Experimental Investigation of Electron Multipactor Discharges at Very High Frequencies

by

Timothy P. Graves

Submitted to the Department of Nuclear Science and Engineering
in partial fulfillment of the requirements for the degree of

Doctor of Philosophy

at the

MASSACHUSETTS INSTITUTE OF TECHNOLOGY

June 2006

Author ....
Department of Nuclear Science and Engineering
May 1, 2006

Certified by ....
Brian LaBombard
Principal Research Scientist, Plasma Science and Fusion Center
Thesis Supervisor

Certified by ....
Steven J. Wukitch
Research Scientist, Plasma Science and Fusion Center
Thesis Supervisor

Certified by ....
Ian H. Hutchinson
Professor of Nuclear Science and Engineering, Department Head
Thesis Reader

Accepted by ....
Professor Jeffery A. Coderre
Chairman, Department Committee on Graduate Students

Experimental Investigation of Electron Multipactor Discharges at Very High Frequencies

by

Timothy P. Graves

Submitted to the Department of Nuclear Science and Engineering
on May 1, 2006, in partial fulfillment of the
requirements for the degree of
Doctor of Philosophy

Abstract

Multipactor discharges are a resonant condition in which electrons impact a surface in phase with an alternating electric field. The discharge is sustained by electron multiplication from secondary emission. As motivation, multipactor discharges can adversely affect many different rf systems in vacuum, and this work provides an improved general understanding of multipactor and gives promising results for improved performance and reliability of these systems.

The Coaxial Multipactor Experiment (CMX) creates and investigates multipactor discharges in both parallel plate and coaxial geometries at very high frequency (VHF). CMX provides the first detailed investigation of multipactor energy distribution functions for both coaxial and parallel plate geometries with the use of retarding potential analyzers (RPA). A 1-D particle tracking simulation supports these experimental distributions and yields the underlying physics behind the distribution shape. Experimental and simulation energy distributions have a low energy population of defocused electrons due to space charge effects and RPA emission, and a high energy population responsible for sustaining the discharge. Results show a higher energy distribution for the coaxial geometry as compared to the parallel plate geometry with the same electrode spacing, implying that coaxial geometries are more susceptible to multipactor. These results are supported by CMX susceptibility data, which are provided for both coaxial and parallel plate electrodes.

Lastly, similar multipactor experiments were performed on Alcator C-Mod rf systems, allowing the discovery of multipactor-induced glow discharge in these systems. Results suggest the onset of this glow discharge causes the observed C-Mod neutral pressure limits. These results are further supported by CMX experiments, and a new, 50 μm sandblasted copper surface treatment has been shown to sufficiently lower $\delta < 1$ for multipactor prevention on CMX and raise the minimum pressure for glow discharge breakdown. This surface treatment shows no significant degradation of high voltage handling, and it is proposed for implementation on the multipactor-susceptible regions of C-Mod rf systems.

Thesis Supervisor: Brian LaBombard
Title: Principal Research Scientist, Plasma Science and Fusion Center

Thesis Supervisor: Stephen J. Wukitch
Title: Research Scientist, Plasma Science and Fusion Center

Thesis Reader: Ian H. Hutchinson
Title: Professor of Nuclear Science and Engineering, Department Head

Acknowledgments

This work would certainly not be possible without the help of many, many people along this path. My thesis supervisors, Steve Wukitch and Brian LaBombard, are at the top of this list. From the beginning, Steve Wukitch encouraged me to develop my interests and discover new areas of research. Rf physics and engineering is, to many, a lost and magical scientific art, so I am very fortunate to have gained the basic tools in this area from a practiced rf Zen master. Also, I am forever grateful to Brian LaBombard, who always had time for me and any others and amazingly still had time for himself. It was Brian's pure curiosity for a new challenge which easily convinced him supervise much of this work.

In addition, I would like to thank Prof. Ian Hutchinson and the department of Nuclear Science and Engineering, because without them, my road and destination would have been very different. Prof. Hutchinson encouraged and permitted funding of this work on multipactor discharge, even when it was driven by pure scientific curiosity. He was always able to ask the right questions and honed this research into what is presented here. The department of which he is currently the head is equally appreciated, as it was the NSE-awarded, MIT Presidential Fellowship that allowed me the freedom to develop a new experiment on multipactor at the PSFC.

The design, construction, and operation of CMX, along with bike repairs, car repairs, custom welding jobs, automotive advice, and all things mechanical or electrical could not have been possible without the help of the PSFC technical and engineering staff. Led by Ed Fitzgerald, I was never turned away and was always given a hard time. Tommy Toland and Ron Rosati were essential in providing vacuum support, advice, and equipment. Mark Iverson, Rick Murray, Charlie Cauley, Andy Pfeiffer, Bob Silva, Sam Pierson, Gary Dekow, Dave Terry, Peter Koert, Bill Beck, Frank Shefton, Paul Lienard, Dave Bellofato, Bob Childs, Bill Parkin, Willy Burke, and Wade Cook were all always willing to help. From the technical and engineering staff, I've learned so much, and because of them, my time at the PSFC was a true blessing and joy.

As a student, many thanks are given to the professors who have dedicated their lives to the equations buried in my brain. To Professors Ian Hutchinson, Jeff Freidberg, Ron Parker, Kim Molvig, and Miklos Porkolab - they're in there, and for that I thank you. I would also like to thank Clare Egan, Valerie Censabella, Corrinne Fogg and the other PSFC and NSE administrative staff for their guidance and aid through the organizational challenges of graduate school.

Where I lack in math, physics, or Latex, my fellow graduate students fill in the gaps. I am forever in debt to the students who have listened and answered my many, and maybe excessive, questions. Jerry Hughes, Howard Yuh, Davis Lee, John Liptac, Vincent Tang, Alex Parisot, Brian Youngblood, Brook Schwartz, and Noah Smick all taught me things that were essential in making this work possible. In addition, I thank my good friend and groomsman, Mike Pope, for lunch, a listening ear, and a thirsty, yet vulgar palette everyday for four years.

Lastly, my most personal gratitude goes out to my family. Both my mother and father have made me who I am today. With their love and unconditional support, I have been able to accomplish so much. To my mother and the many $20 bills earmarked for the bar and not the study hall. To my father who has always and continues to be my role model in all his endeavors. To my sister Pam for all the childhood fights that have now become a deep friendship, now extending to her husband David. But without my unbelievably hard-working guardian angel and his omniscient Employer, none of this would be possible. This work contains many "mishaps" or strange coincidences that yielded key results, and in fact, the entire project started with "accidental" multipactoring. I owe everything to the plan which has been laid out above, and I owe even more for who He has given me to accompany through the rest of my life. Samantha Collins, my best friend and ultimate companion, I thank you for your unconditional love and support. Through thick and through thin, and till death do us part, I will love you forever.

Contents

List of Figures

List of Tables

Chapter 1

Introduction

1.1 Description of a Multipactor Discharge

A multipactor discharge is a phenomenon in which electrons impact one or more material surfaces in resonance with an alternating electric field [1, 2]. Multipactor discharges can occur in radio frequency (rf) or microwave systems in vacuum conditions, as the electrons of this discharge impact the surfaces in phase with the alternating field. The pure electron discharge requires a multiplication in the number of electrons by secondary emission from the impacted surfaces [3, 4]. Fig. 1-1 depicts a simplified picture of a multipactor discharge. In panel A, an electron is born and then accelerated by the oscillating electric field of the form $E_o \sin(\omega t)$, with amplitude, E_o, frequency, ω, and time, t. In this example, the electron hits the opposite electrode with sufficient energy for emission of two secondary electrons. This emission occurs near the time when the field reverses direction at $\omega t = \pi$, and these two secondary electrons, shown in panel B, are then accelerated across the gap in the reverse direction. Again, these electrons traverse the gap in half the cycle time and impact with enough energy to cause further electron multiplication by secondary emission. This process continues with each half cycle as the multipactor develops.

The resonant electron motion described in Fig. 1-1 relies on several factors for the successful development of the multipactor discharge. First, the rf frequency and system geometry coupled with the accelerating electric field must give rise to this

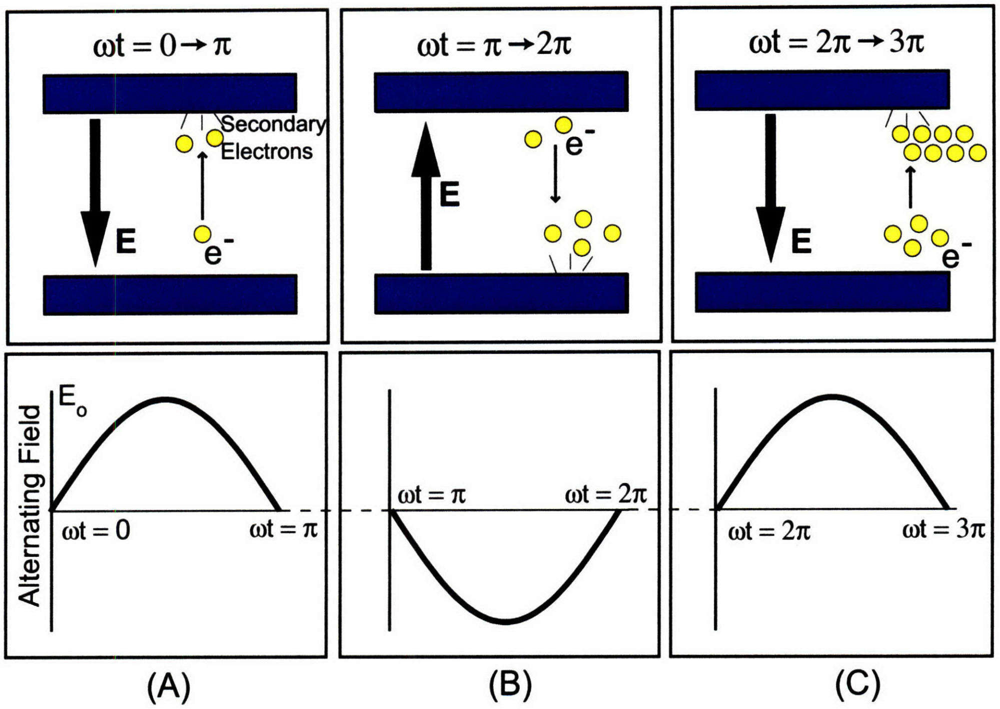

Figure 1-1: Simple explanation of a multipactor discharge with an electric field oscillating between two metal electrodes. Upon each electron impact, secondary electrons are emitted from the surface, multiplying the total number of electrons with each half cycle.

type of resonant electron motion; i.e. the electric field must be just right for a given frequency and geometry in order for electrons to impact the two surfaces in phase with the field. For example, if the rf electric field is too high for a given frequency and electrode spacing, the initial electron will impact too early, the secondary electrons will be emitted against the electric field, and they will not be able to accelerate back across the electrode gap. Conversely, if the electric field is too low, the electron may impact with insufficient energy for secondary electron emission. As a consequence, electrons which sustain the multipactor are focused into a narrow sheet over many cycles, impacting with the required phase range to sustain the resonance.

Secondly, the impacted surfaces must allow for a gain in the number of electrons by secondary emission. As will be described in the next chapter, the secondary electron coefficient must be greater than unity for the incoming electron energy. The electrons of a pure multipactor discharge are supplied completely by secondary emission, so the secondary emission coefficient is critical to the development of the discharge. Lastly, it is necessary for this discharge to occur under vacuum pressures, typically less than 1 mtorr [5], as frequent collisions with background gas can prevent the necessary resonant electron motion.

When the proper geometry, rf frequency, and voltages are combined in vacuum with surfaces possessing the necessary secondary electron emission characteristics, multipactor discharges can occur. These discharges have been observed for low to medium voltages ($<$ 10kV) at frequencies ranging from MHz to 10's of GHz and vacuum pressure [1]. There are several scientific and engineering applications, such as rf satellite payloads [6, 7, 8], particle accelerators [9, 10], and rf fusion experiments [11, 12, 13], which utilize rf power at these frequencies and vacuum pressures, and as a result, they are often affected by these discharges. In addition, these rf applications often involve metal and dielectric materials with sufficiently high secondary electron emission to support multipactor discharges.

Multipactor discharges are considered detrimental to rf systems in most applications. The discharges can detune rf systems, limit the delivery of rf power, damage high power rf sources, and cause a local pressure rise due to the desorption of surface gases. In some cases [5, 14], multipactor can induce a glow discharge below the expected minimum pressure for a multipactor-free, Paschen-type rf glow discharge [15]. As a result, much effort has been placed on preventing multipactor in these systems [9, 16, 17, 18, 19]. While there are some beneficial aspects of multipactor discharge [1], such as vacuum conditioning or electron sources, this work will focus on multipactor as an unwanted phenomenon to be avoided and/or prevented. This work also focuses on multipactor discharges occurring between metal electrodes at frequencies in the very high frequency (VHF) range (30-300 MHz). There is another type of multipactor which occurs on a single dielectric surface, yet it is outside the scope of this work. Kishek's review of multipactor discharges [1] lists many references on this single surface multipactor.

1.2 Historical Background and Motivation

Multipactor discharges were first reported in the 1920's by the Guttons in a series of French publications [20], yet it wasn't until 1934 when Philo T. Farnsworth first referred to this phenomena as *multipactor* [21]. In the following years, Farnsworth received several patents on electron amplifiers and other technologies which highlighted multipactor discharges [22, 23, 24, 25]. In the 1940's, while investigating high frequency gas discharges at low pressure, Gill and von Engel rediscovered multipactor and began the first of many theoretical and experimental studies on the subject of multipactor discharge [26]. Shortly after, dedicated multipactor studies began to specifically investigate and refine the conditions for which multipactor occurs [27, 28]. Since this time, there have been numerous theoretical and computational studies and several experimental investigations of the multipactor effect, and these works are summarized in both review articles of Kishek [1] and Vaughan [2].

To date, experimental multipactor investigations have mainly focused on the voltage, frequency, and geometric criteria for which multipactor can occur, giving susceptibility curves as will be discussed in the next chapter. To the knowledge of the author, there have been no dedicated efforts to experimentally measure the features of the electrons in the multipactor discharge for a range of frequencies at VHF, in the typical geometries supporting rf at these frequencies. *Experimental Investigation of Electron Multipactor Discharges at VHF* is a study which provides experimental data on the steady state multipactor and the electrons within this discharge in parallel plate and coaxial geometries (see Chap. 2). By further understanding these multipactor discharges, rf systems can be better designed to avoid or prevent multipactor. The data from this study can also be used for computational verification of present and future simulations, and it could also lead to the development of new technologies which take advantage of the multipactor discharge.

While this research answers many questions surrounding general multipactor discharges in coaxial and parallel plate geometries, it also provides several very important rf engineering results. *Experimental Investigation of Electron Multipactor Discharges* *at VHF* is in direct support the rf systems used on fusion experiments, specifically Alcator C-Mod, and the multipactor discharges occurring within them. As will be shown in Chap. 6, multipactor discharges can limit these rf systems, consequently limiting the fusion experiment as a whole. This work specifically identifies multipactor discharge as the cause of neutral pressure limitations; therefore, by taking measures to eliminate multipactor in these systems, improved rf operation will lead to more successful fusion experiments.

This thesis begins with the foundational background of rf systems, secondary electron emission, and the theoretical discussion of multipactor discharge in Chap. 2. Next, the experimental setup and multipactor data of the Coaxial Multipactor Experiment [29] is given in Chap. 3. In support of this experimental data, a single particle multipactor simulation was developed and is described in Chap. 4, and Chap. 5 uses this simulation for the analysis of the experimental data. Chap. 6 discusses the role of multipactor on Alcator C-Mod and the supporting experiments to measure and ultimately eliminate these discharges on C-Mod. Finally, Chap. 7 gives the conclusions of this work.

Chapter 2

Fundamentals of Multipactor Discharges

In order to fully understand the physics of multipactor discharges which occur at VHF, several fundamental background subjects must first be introduced. As multipactor is a radio frequency effect, the first section of this chapter will discuss the underlying basic principles of the transmission of electromagnetic fields at the frequencies of interest in parallel plate and coaxial transmission lines. Following the rf fundamentals section, the basic principles behind secondary electron emission will be discussed, as it is this phenomena which gives rise to the multiplication of electrons in a multipactor discharge. After these two foundation principles are introduced, the theoretical background and principles of multipactor discharges are given, including the underlying equations and motivation for this investigation.

2.1 Basic Principles of Radio Frequency Transmission

The main goal of the transmission of power using electromagnetic fields is to effectively deliver rf power to a particular load with minimal power attenuation or loss. Beginning at an rf source, the rf power may have to travel very long distances of many wavelengths before arriving at the load, and transmission lines are successful in achieving this goal with low power loss.

In order to effectively deliver the power to the load and minimize power reflections, the impedancesof the source, load, and all connecting transmission lines, defined by $Z = \frac{V}{I}$, should be "matched" such that the source effectively deposits the rf power into a pure resistive load. [30, 31, 32]. If the impedances are not properly "matched", some fraction of the rf power will not be delivered to the load and will be reflected back toward the source. The degree of the reflection or "mismatch" is often described by the reflection coefficient, Γ, given by the ratio of the reflected voltage, V_- to the forward voltage, V_+. The reflection coefficient can also be defined in terms of the load impedance, Z_L, and the characteristic impedance of the line, Z_o, as shown below.

$$\Gamma = \frac{V_-}{V_+} = \frac{Z_L - Z_o}{Z_L + Z_o} = \frac{Z_{Ln} - 1}{Z_{Ln} + 1}, \tag{2.1}$$

where the normalized load impedance, $Z_{Ln} = \frac{Z_L}{Z_o}$. An ideal, perfectly matched rf system with Z_L=Z_o would deliver all rf power to the load, no power would be reflected, and $\Gamma = 0$. If instead, the rf load is an electrically open circuit, the load impedance $Z_L = \infty$, and $\Gamma = 1$, indicating a complete reflection of rf power. A standing wave results on the transmission line with $V = V_{max}$ at the load . Conversely, if the load is replaced with an electrical short, there is a standing wave pattern with V=0 at the load for Z_L=0 and $\Gamma = -1$. The voltage standing wave pattern, or VSWR, is used to quantify the standing wave and reflected power, and it is defined as the ratio of the maximum line voltage to the minimum line voltage. It can also be defined in terms of Γ as shown in Eqn. 2.2.

$$VSWR = \frac{V_{max}}{V_{min}} = \frac{1 + |\Gamma|}{1 - |\Gamma|} \tag{2.2}$$

Fig. 2-1 illustrates a simple schematic of a transmission line being used in a rf power system. As mentioned, the rf voltage on the transmission line is made up of a forward traveling wave and reverse traveling or reflected wave. These two waves combine to create a standing wave pattern along the transmission line, as shown in

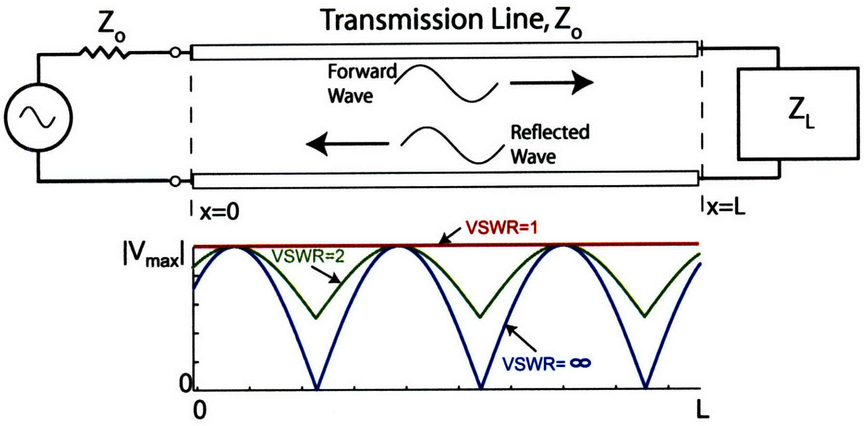

Figure 2-1: An simplified example of a transmission line delivering rf power from a source to a load of impedance, Z_L. Standing wave patterns are shown for several different reflection coefficients.

the lower part of the figure. For the case Z_L=Z_o, all power is delivered to the source, and there is no standing wave pattern. The voltages on the transmission line are all equal to V_{max}. For the two cases described previously with $|\Gamma| = 1$, VSWR=∞, meaning V_{min}=0, as shown in Fig. 2-1.

Often, rf systems are operated at 50 Ω, and the source and transmission lines are matched with this impedance. If a load with a 50 Ω impedance is chosen, all power is delivered to this load with $\Gamma = 0$. Yet, in most cases, rf loads cannot have their impedance specified to match the source and connecting transmission line. Actual impedances are made up of both a resistive impedance, R, and a reactive impedance, X. The reactive impedance is a result of capacitance or inductance of a rf component. Capacitive reactance is given by $X_c = \frac{1}{i\omega C}$ for capacitance, C, and inductive reactance is $X_L = i\omega L$, where L is the inductance in this case. The resulting complex impedance is expressed as $Z = R + X$. For example, a load of 100Ω in a 50Ω system gives reflection coefficient of $\Gamma = 0.333$, corresponding to 11% reflected power. In this case, the VSWR=2, and the standing wave pattern would be of the form shown in Fig. 2-1. The lowest voltage on the line would be half of the maximum voltage.

Loads can be a variety of rf devices, including antennas coupled to plasmas, antennas coupled to air, or other devices [33]. In addition, transmission lines may have sections where impedance mismatches may occur and cause power reflections. When dealing with high power rf, sources can be severely damaged by this reflected power, so impedance matching networks are implemented to minimize the reflected power to the source. The reflected power is minimized as a result of an appropriate impedance change provided by the impedance matching network, and as a result the load appears as a pure and matched resistance to the source [31]. The matching network "matches" the source side of the transmission line, and provides sufficiently low reflected power for rf operation. Yet, as a result of the impedance matching network, the unmatched side is a resonant cavity which can store energy as a standing wave pattern between the load and the matching network.

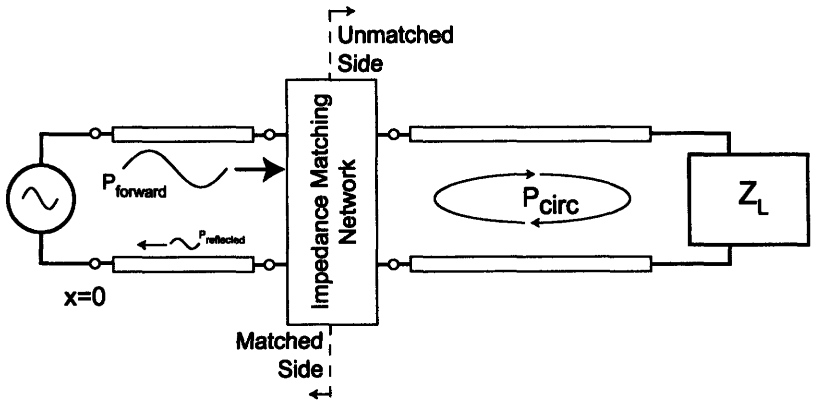

Figure 2-2: A typical rf power system with impedance matching network to minimize reflected power to the source.

As before, the standing wave pattern in the unmatched section depends on the reflection coefficient and the amount of power absorbed by the load. The amount of stored energy in the resonant loop is given by the quality factor, Q, of the circuit. The Q factor is defined as

$$Q = 2\pi\frac{\text{Stored energy}}{\text{Power dissipated in one rf cycle}} = \frac{X}{R} = 2\pi\frac{P_{circ}}{P_{forward}}. \tag{2.3}$$

For a system with very low power dissipation, such as a capacitor, the Q factor is typically of order 1000, while for rf antenna systems, the Q factor is much lower between 10 and 100 [34]. Also, the voltage in the unmatched or resonant section of the transmission line grows with a time constant $\tau_{rf} = \frac{Q}{\omega}$, where ω is the angular rf frequency, yielding a longer voltage rise time for a higher Q factor. Often in rf engineering, the stored energy of an rf system is expressed in terms of circulating power. The circulating power, P_{circ}, is expressed as

$$P_{circ} = \frac{1}{2}\frac{(V_+^2 + V_-^2)}{Z}. \tag{2.4}$$

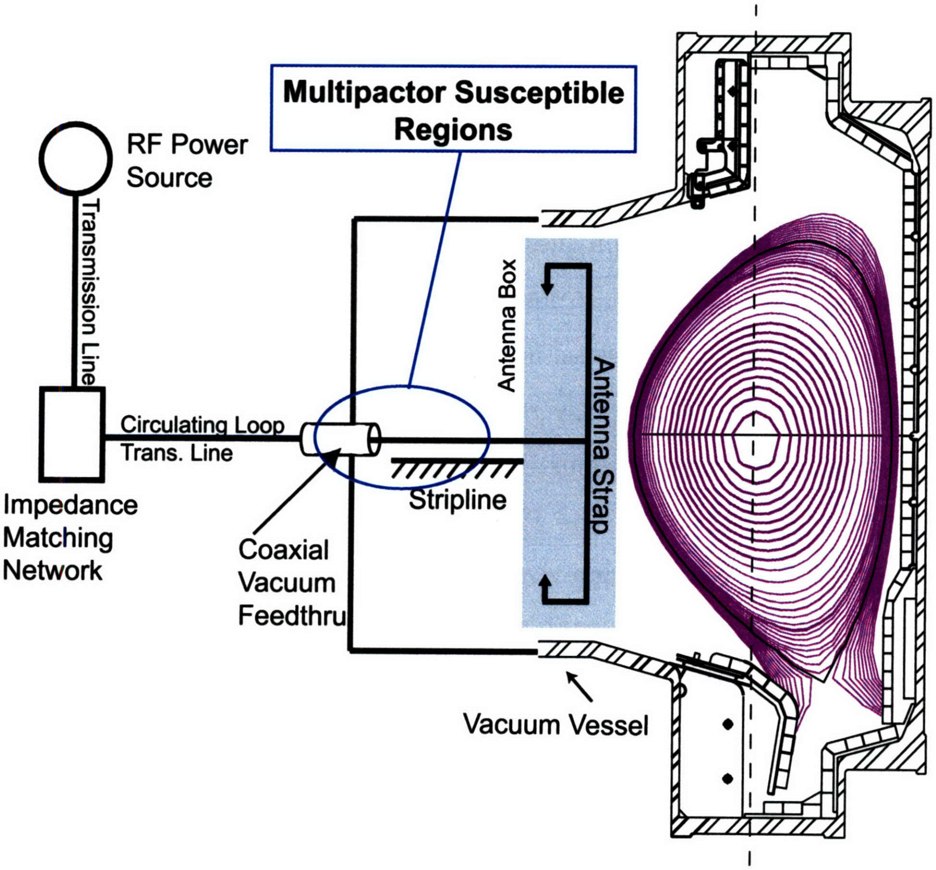

Figure 2-3: Alcator C-Mod and other fusion experiments use high power rf for plasma heating. These systems can be affected by multipactor discharges.

When the multipactor discharge occurs in a tuned rf system, the electrons change the resonant impedance of the network, resonator, or cavity, such that the impedance matching network can no longer prevent reflected power to the source. When the multipactor occurs, it detunes the network, which can be seen as a rise in reflected power. Also, the Q of the circuit drops with multipactor current, as the multipactor limits the amount of power that can be delivered to the load. It is this effect which motivates the need to further understand multipactor discharges, primarily for prevention purposes on rf systems like those present on fusion experiments[12]. Fig. 2-3 illustrates the Alcator C-Mod rf system, which has several possible locations where multipactor is possible. This figure is also discussed in Chap. 6.

2.2 Transmission Lines

Two common transmission lines for wave propagation are parallel plate and coaxial transmission lines, and these are discussed in the following two sections. As the focus of this work is multipactor discharges in these transmission line geometries, understanding the electric fields within these lines is critical to understanding multipactor phenomena. Typically, for VHF, rf power is propagated in transmission lines as transverse electromagnetic (TEM) waves, in which both the electric field, **E**, and magnetic field, **B**, are perpendicular or transverse to the direction of propagation. In addition, the electric and magnetic fields must be perpendicular to each other, as determined from Maxwell's equations [30]. The TEM fields are given for both parallel plate and coaxial geometries in the following sections.

2.2.1 Parallel plate transmission line

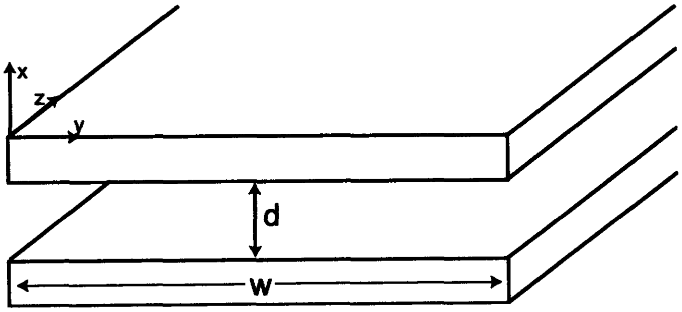

Figure 2-4: An example of a parallel plate transmission line, with plate separation, d, and width, w. In this case, the wave is propagating in the z direction.

A simple and commonly used transmission line is the parallel plate transmission line, illustrated in Fig. 2-4. In this example, the parallel plates have spacing, d, and width, w, and the wave propagation direction is in the z direction. For a wave propagating in the z direction with amplitude, E_o, angular frequency, ω, and wave number, k, the electric and magnetic fields are given by

$$\mathbf{E} = \hat{\mathbf{x}} E_o \sin(k_z z - \omega t), \tag{2.5a}$$

$$\mathbf{B} = \hat{\mathbf{y}} \frac{E_o}{c} \sin(k_z z - \omega t), \tag{2.5b}$$

where c is the speed of light in vacuum. The parallel plate electric field, which accelerates the electrons in a multipactor, sinusoidally varies in time with frequency, f. From Eqn. 2.5a, at a fixed time, the voltage varies linearly in the x direction and is given by

$$V_{pp} = -E_o x \cdot sin(k_z z - \omega t). \tag{2.6}$$

The voltage and electric field amplitudes are related by $V_o = E_o \cdot d$. Using Ampere's law and Eqn. 2.5b, the sinusoidal current is given by

$$I_{pp} = \frac{E_o}{\eta_o} w \cdot sin(k_z z - \omega t), \tag{2.7}$$

where the vacuum intrinsic impedance, $\eta_o = \sqrt{\frac{\mu_o}{\epsilon_o}}$. Using Ohm's law, the characteristic impedance of the parallel plate transmission line is

$$Z_o = \frac{V_{pp}}{I_{pp}} = \eta_o \frac{d}{w}. \tag{2.8}$$

2.2.2 Coaxial transmission line

In contrast to the parallel plate line, the coaxial transmission line contains the **E** and **B** fields completely and can also maintain vacuum pressure within the closed outer conductor. For this reason, coaxial lines can often be found in rf vacuum system. An example of a coaxial transmission line with wave propagation in the z direction

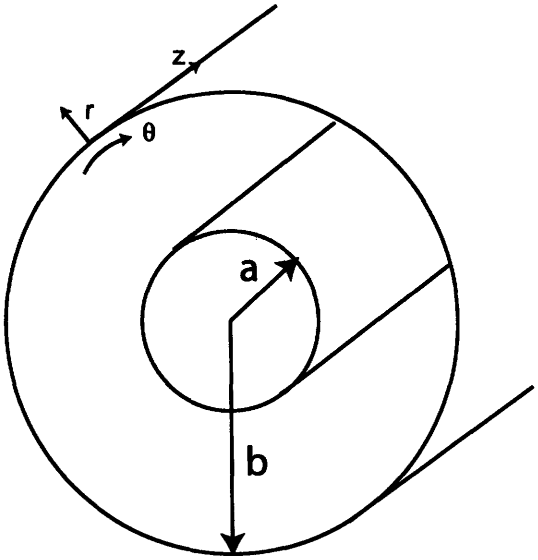

Figure 2-5: Schematic view of a coaxial transmission line with inner conductor of radius, r=a, and outer conductor of radius, r=b.

is illustrated in Fig. 2-5. The coaxial transmission line is made up of an inner conductor of radius, a, and an outer conductor of radius, b. Starting with Gauss's law in cylindrical coordinates, the electric field is given by

$$\mathbf{E}_{coaxial} = \hat{\mathbf{r}}\frac{E_o}{r}\sin(k_z z - \omega t). \tag{2.9}$$

In the cylindrical geometry, the electric field is inversely related to the radius between the coaxial electrodes. This is a fundamental difference from the linear electric field of the parallel plate geometry. As in the parallel plate case, the magnetic field of the coaxial geometry is perpendicular to the electric field.

$$\mathbf{B}_{coaxial} = \hat{\theta}\frac{1}{c}\frac{E_o}{r}\sin(k_z z - \omega t). \tag{2.10}$$

The voltage between the two conductors is also a function of radius, shown in Eqn. 2.11. In the coaxial geometry, the electric field and voltage amplitudes are related by $V_o = E_o \cdot \ln(\frac{b}{a})$.

$$V_{coaxial} = -E_o \ln\frac{r}{b}\sin(k_z z - \omega t) = \frac{V_o}{\ln\frac{b}{a}}\ln\frac{r}{b}\sin(k_z z - \omega t) \tag{2.11}$$

As in the previous case, the current is determined from Ampere's law and Eqn. 2.10

$$I_{coaxial} = 2\pi \frac{E_o}{\eta_o} \sin(k_z z - \omega t), \tag{2.12}$$

and the characteristic impedance of the coaxial transmission line is

$$Z_o(coaxial) = \frac{\eta_o}{2\pi} \ln \frac{b}{a} \tag{2.13}$$

In both parallel plate and coaxial geometries, the characteristic impedances are chosen to match the impedance of the source, which area all 50 Ω in the following discussed experiments.

2.3 Secondary Electron Emission

When an electron impacts a surface, it is possible for this electron to cause the emission of additional electrons from the impacted surface, called secondary emitted electrons [3]. This phenomenom is dependent on the impacting electron energy, angle, and the surface material properties. The effect of secondary electron emission is discussed in many different texts [3, 4, 35, 36], and it is still a topic of interest for new materials and surface treatments [16, 37, 38]. As an electron impacts a surface, inelastic and elastic collisions are also possible, but these effects will neglected for this discussion regarding multipactor. In this discussion, the incoming, high energy electron is referred to as the primary electron, and the emitted electron is referred to as the secondary electron.

2.3.1 Energy distribution of secondary emitted electrons

Secondary emitted electrons are emitted from material surfaces with a distribution of energy which has been investigated both experimentally [3, 4], and theoretically [39]. This distribution is a non-maxwellian, low energy distribution with electron energies below 50 eV, and is independent on the primary electron energy. The distribution of energies has a peak typically from 1 to 5 eV for metal surfaces [4]. Chung and Everhart developed an analytical expression for this distribution function, given in Eqn. 2.14 [39].

$$f(E) = \frac{E}{(E+\phi)^4} \tag{2.14}$$

where in this case, E is the emitted electron energy. Eqn. 2.14 agrees well with experimental data, and it is dependent on the material work function, ϕ. Fig. 2-6 illustrates the distribution of secondary emitted electron energies using the Chung-Everhart equation with $\phi = 4.46$ eV.

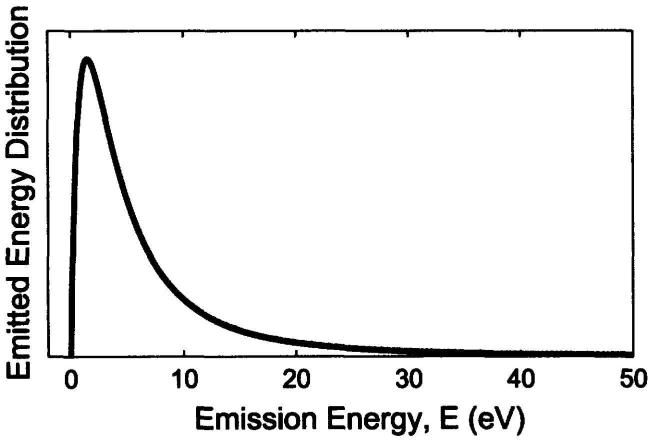

Figure 2-6: Distribution function of the emitted secondary electron energy, where $\phi = 4.46$ eV, corresponding to copper.

2.3.2 Angular distribution of secondary emitted electrons

In addition to the energy distribution of the secondary electrons shown in the preceding section, secondary electrons are also emitted with a spread in angle relative to normal surface vector. In this case, an electron emitted completely normal to the surface has a 0° emission angle. It has been shown experimentally that the secondary electrons are emitted with an approximate cosine distribution [3, 40], shown in Fig. 2-7.

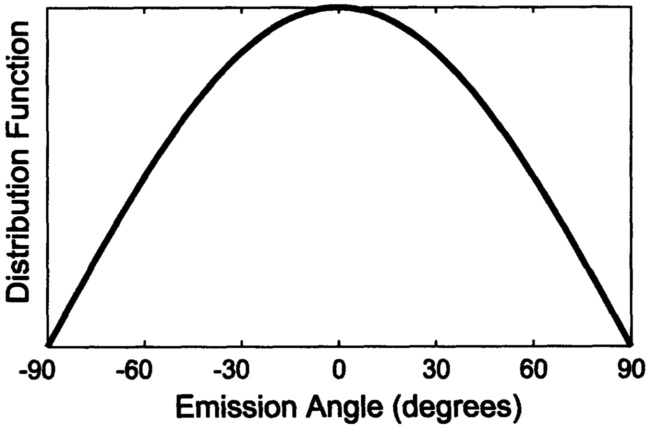

Figure 2-7: The emission angle distribution function for secondary electrons is given by a cosine distribution.

2.3.3 Secondary electron yield and the secondary electron coefficient

The most important aspect of secondary electron emission in regards to multipactor discharge is the secondary electron yield, represented as δ, and also known as the secondary electron coefficient. This secondary electron coefficient represents an average number of secondary electrons emitted as a function of the primary electron impact energy. Because multipactor discharges require a multiplication of electrons with each cycle, as described in Chap. 1, δ is critical in the development and sustainment of the multipactor.

Fig. 2-8 illustrates the secondary electron coefficient dependence on primary electron energy. As seen in the figure, $\delta = 1$ at two energies, E_1 and E_2. These are often referred to as the first and second crossover points. At these points, the number of secondary electrons emitted is equal to the number of incoming primary electrons. At $E_1 < E_{PE} < E_2$, the number of secondary electrons is greater than the number of primary electrons with energy E_{PE}. It is this energy range which is the focus for multipactor discharges, as these discharges rely on the multiplication or gain of electrons by secondary emission. The maximum secondary electron coefficient, δ_{max}, occurs at an energy, E_{max}.

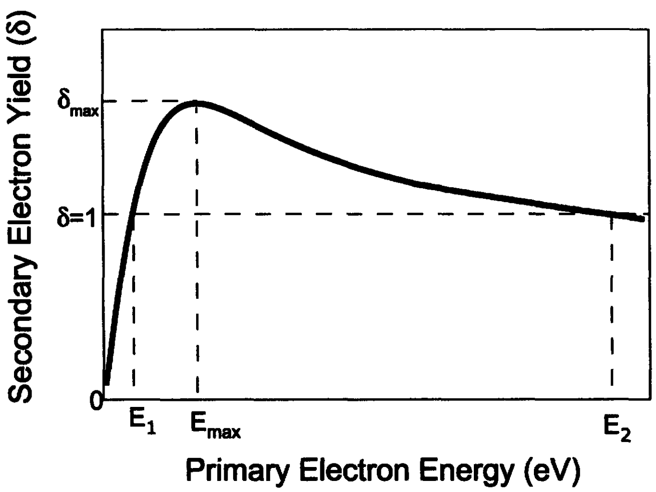

Figure 2-8: The secondary electron yield (coefficient), δ, as a function of primary electron energy.

The general shape of δ shown in Fig. 2-8 holds for many metals and insulators. Because the shape is in general the same, experimental data for δ is typically given in terms of the crossover energies, E_1 and E_2, and the curve maximum, δ_{max} and E_{max} [3, 4, 35, 36]. Table 2.1 gives experimental data on the secondary emission coefficient for different electrode materials from various references.

It is discussed by both Bruining and Gibbons that the secondary yield can increase with oblique incident angles of the primary electrons [3, 36]. This effect is also seen by Kirby and King [42]. In [42], the secondary electron yield can increase up to 60% for oblique angles of 75°. This increase in δ is typically only seen for very smooth surfaces, as rough surfaces emit secondary electrons with no preference to the incident angle.

Bruining also discusses the effect of adsorbed gases on the secondary yield of a surface. The presence of adsorbed gases effectively lowers the work function, ϕ, of the material, which can in turn raise δ [3]. McKay has shown a 60% increase in δ with a factor of two decrease in ϕ, caused by an adsorbed sodium layer on tungsten [44].

It has also been shown in the literature that rough surfaces can successfully lower δ below unity in order to prevent multipactor [16, 36, 45]. Surface roughening suppresses secondary electron emission by increasing the probability that a secondary emitted

Material/Surface	δ_{max}	E_{max} (eV)	E_1 (eV)	E_2 (eV)	Ref.
Cu (pure/GDC)	1.28-1.4	600	200	> 1500	[35, 36, 16]
Cu (as received)	2.4-2.5	280-300	< 100	3000	[16, 37]
Cu (Baked at 300°C)	1.8	300	100	2000	[16]
Cu_2O	1.19-1.25	440	n/a	n/a	[36]
Stainless Steel (304)	1.2-1.4	300-400	70-200	1000	[41, 5, 42]
Ti (pure)	0.9	280	–	–	[35, 36]
Ti (as received)	2.0	200	< 100	1500	[16]
TiN (air exposure 15 min)	1.18	n/a	107	n/a	[43]
TiN (air exposure 30 min)	1.20	n/a	80	n/a	[43]
TiN (air exposure 4 days)	1.58	n/a	53	n/a	[43]
Al (pure)	0.97-1.0	300	300	300	[35, 36]
Al (99.5%, as received)	3.5	350	< 100	> 2000	[16]
Al_2O_3	1.5-3.2	350-1300	40	n/a	[36]
C (graphite)	1.0-1.02	300	200-300	300 -350	[35, 36]
C (aquadag)	0.75	350	–	–	[35, 36]
C (soot)	0.45	200-500	–	–	[35, 36]
Fe (pure)	1.3	200-400	120	1400	[35, 36]
Mo (pure)	1.25	300-375	140-150	1100-1200	[35, 36]
W (pure)	1.35-1.4	650	250	> 1500	[35]
Ni (pure)	1.3	550	150	> 1500	[35]
Au (pure)	1.79	1000	150	> 4000	[36]

Table 2.1: Secondary electron emission properties for different materials. GDC refers to glow discharge cleaned [16].

electron will be immediately reabsorbed by a neighboring peak on the roughened surface. As previously mentioned, the secondary electrons are emitted with a cosine angular distribution, and if the roughness is high enough, many of the electrons will scatter within the local surface peaks until they are reabsorbed in the surface. This effect will be discussed further in Chap. 6.

Several different analytical models have been developed over the years to determine curves like that given in Fig. 2-8. The most comprehensive survey and study of these analytical models is Vaughan's approach [46], and this model is used in many of the recently developed multipactor simulations [1].

2.4 Multipactor Discharge Basics

As mentioned, multipactor discharges can occur in vacuum when an electron impacts a surface in resonance with the rf electric field and causes a gain in the number of electrons by secondary emission. As will be shown, this resonance condition depends on the electron transit time between two electrodes, which is dependent on the accelerating voltage, the rf frequency, and the system geometry. In addition, the electrons have to impact with $E_1 < E_{PE} < E_2$ such that $\delta > 1$, and the number of electrons increases with each half cycle.

2.4.1 Theory of multipactor discharges

The multipactor resonance condition for an electron in a parallel plate geometry can be determined analytically starting with the Lorentz force and the equation of motion,

$$\frac{d\mathbf{v}}{dt} = \frac{q}{m}\left(\mathbf{E} + \mathbf{v} \times \mathbf{B}\right) \tag{2.15}$$

If the electron velocity is sufficiently less than c, then the magnetic field can be neglected, as it has a magnitude smaller than **E** by a factor of c (Eqn. 2.5). Assuming 1-D motion in the x direction, and an oscillating electric field of the form

$$E_x = E_o \sin(\omega t), \tag{2.16}$$

the equation of motion in the x direction becomes

$$\frac{dv}{dt} = \frac{eE_o}{m}\sin(\omega t), \tag{2.17}$$

where e is the electron charge, m is the electron mass, and ω is the angular frequency. If the electron is born from an electrode at a time, t = $\frac{\alpha}{\omega}$, relative to the rf phase, α, with initial velocity v_o, the time dependent, 1-D velocity and position of the electron are given by

$$v = v_o + \frac{eE_o}{m\omega}\left(\cos(\alpha) - \cos(\omega t)\right) \tag{2.18a}$$

$$x = x_o + \frac{v_o}{\omega}(\omega t - \alpha) + \frac{eE_o}{m\omega^2}\left[\sin(\alpha) - \sin(\omega t) + \cos(\alpha)(\omega t - \alpha)\right]. \qquad (2.18b)$$

In the simplest example, the multipactor resonant condition specifies the electron must traverse the electrode spacing, d, and impact the opposing surface near the time the electric field changes direction. The electric field changes direction at $\omega t = N\pi + \alpha$, where N is a positive odd integer. Invoking this condition of $\omega t = N\pi + \alpha$ in Eqn. 2.18b, the multipactor condition for the voltage in a parallel plate geometry is given by

$$V_o = E_o \cdot d = \frac{m}{e}\frac{\omega d(\omega d - v_o N\pi)}{N\pi\cos\alpha + 2\sin\alpha}. \qquad (2.19)$$

For simplicity, if the electron is born at the x=0 electrode with $v_o = 0$, and $\alpha = 0$, Eqn. 2.18b becomes

$$V_o = \frac{4\pi m}{e}(f \cdot d)^2, \qquad (2.20)$$

using N = 1 and $f = \frac{\omega}{2\pi}$. For a parallel plate geometry similar to that given by Fig. 2-4, with electrodes placed at x = 0 and d, Fig. 2-9 depicts example trajectories of several electrons starting at t=0 with a emission energy chosen from a secondary emission distribution function, accelerating in a 70 MHz, 250 V field. These electrons move resonantly between the plates, impacting near the field reversal time. Many of these electrons impact with sufficient energy for secondary emission, as seen by the continued trajectories after an electrode is impacted.

One important result of this simple theoretical analysis is a scaling law for the multipactor voltage. For a parallel plate geometry, the multipactor voltage scales with frequency and gap distance squared, or $V \propto (f \cdot d)^2$. For frequencies in the VHF range and gap spacings on the order of centimeters, the multipactor voltage is of order 10^2 volts.

In many cases, Eqn. 2.20 can be used as a back of the envelope estimate for the

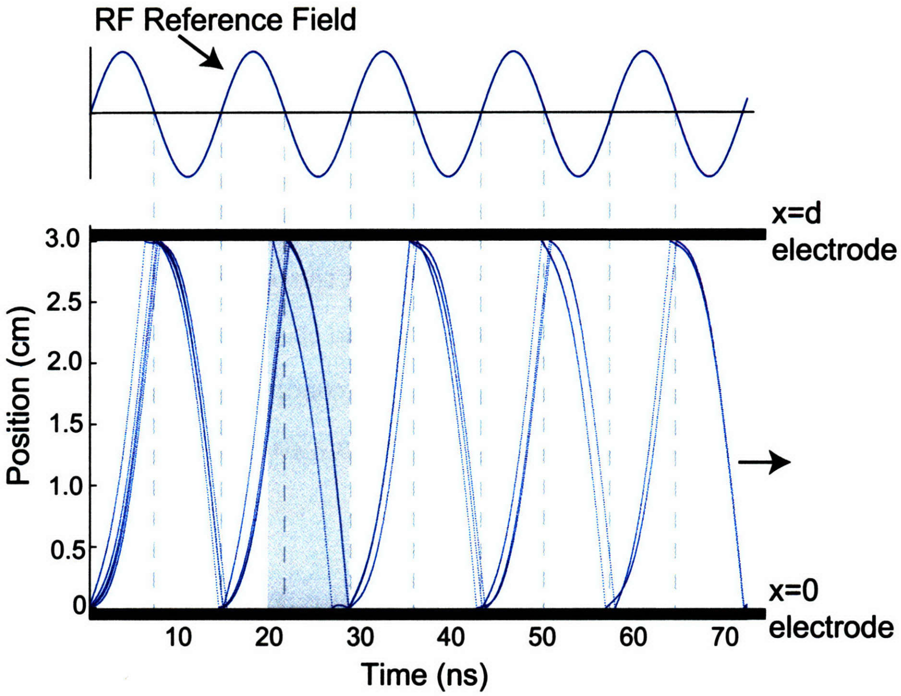

Figure 2-9: An example of electron trajectories impacting between two parallel plate electrodes, spaced at 3 cm. In this case, the rf voltage is 250 V and the frequency is 70 MHz.

resonant multipactor voltage. Yet for Eqn. 2.20, the electron is born at $\alpha = 0$ and with no initial velocity. In reality, the secondary electrons are emitted with a range of rf phases and an energy distribution given by Fig. 2-6. Because of the phase and emission energy variation, there is a range of voltages over which multipactor can occur. This multipactor range of the minimum and maximum resonant voltages is often plotted with the product of frequency and distance, giving what is often called a "susceptibility curve". Susceptibility curves are often determined computationally or experimentally for different materials and geometries[1, 2, 28, 47, 48]. These curves illustrate the voltages, frequencies, and gap sizes to be avoided for multipactor sensitive systems.

The upper and lower multipactor susceptibility bounds for a parallel plate geometry can be determined theoretically for zero or monoenergetic electron emission energy [1]. The lower bound is determined by maximizing the denominator of Eqn. 2.19 and obtaining the theoretically maximum phase, $\alpha_{max} = \arctan \frac{2}{N\pi}$. The upper bound for zero energy emission is determined from Eqn. 2.20. This upper bound increases with nonzero emission energy due to the possibility of emission at negative phase. A negative phase is possible for an electron that has sufficient emission energy in order to not be accelerated back to the emitting electrode. In reality, because of the random nature of the emission energy, these theoretical models can only give approximate ranges of the multipactor susceptibility, as illustrated in Fig. 2-10. This figure illustrates experimentally determined onset voltages for multipactor in parallel plate and coaxial geometries, and for different electrode surface compositions. Fig. 2-10 will be discussed further in Chap. 5.

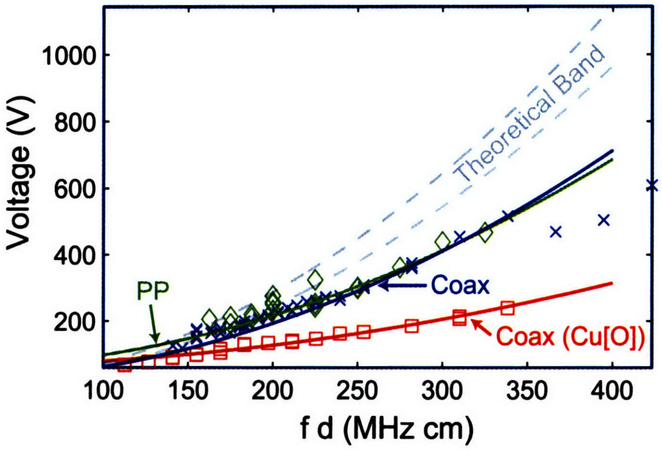

Figure 2-10: Experimentally determined, minimum voltage for multipactor in parallel plate and coaxial geometries. Kishek's monoenergetic model for susceptibility [1] is insufficient for determining these bands. This figure will be discussed at length in Chap. 6.

Experimental susceptibility curves often provide the minimum multipactor voltage for a particular frequency and distance [5, 47], as in Fig. 2-10. In addition, and not shown in Fig. 2-10, the upper bound of the multipactor can also be shown. Because the multipactor discharge is a resonant condition, it is possible to "push through" the multipactor resonant band to higher voltage, as long as the system can handle the rf loading and reflected power as a result of the multipactor. Multipactor push-through is often seen as a large jump in cavity voltage as the multipactor extinguishes and removes the detuning element in the rf circuit. For frequencies and materials studied in this work, the multipactor extinguishes due to the defocusing of the electron sheet in the non-resonant field. In order to experimentally determine the upper limit of the multipactor susceptibility band, the voltage is typically started above the multipactor resonance and lowered until the discharge is detected [47].

In addition and of equal importance, the multipactor discharge develops as a result of the amplification of electrons by secondary emission at each electrode impact. The electron gain from secondary emission must be greater than the rate at which electrons in the system are lost. The impact energy of the incoming primary electron must be in the energy range for $\delta > 1$; i.e. $E_1 < E_{PE} < E_2$ in order to contribute to the gain of the multipactor. Electrons which impact with energy outside this range are lost to the electrodes by absorption. It is possible for an electron to impact with $E_1 < E_{PE} < E_2$ too early or too late in reference to the change in the rf field due to the variation in emission energy. Due to the subsequent advance or delay of the secondary emission, this new electron may in turn not be able to achieve "multipactor-sustaining" status with $E_1 < E_{PE} < E_2$ in the next cycle and is lost by absorption. For example, in the shaded region of Fig. 2-9 near 20 ns, there is an electron which impacts at a time earlier than the others. In the next cycle, this electron again impacts too early, and consequently is born against the rf electric field and is absorbed by the lower electrode. As a result, there is a phase focusing evolution, in which only electrons that hit with both sufficient energy for high electron gain and proper phasing continue to the next cycle. As a result of this phase focusing effect, the electrons move between the conductors as a thin electron sheet that can fill up to 33% of the electrode gap. This effect can be seen in the simulation results of Chap. 4, and is also discussed by Vaughan [2].

2.4.2 Multipactor saturation

If resonant conditions are satisfied, and the impact energy is in the correct range for a large electron gain, the number of electrons cannot grow infinitely, and there must be some mechanism for saturation. Kishek has shown one saturation mechanism is rf loading caused by the multipactor discharge. As the multipactor grows, it detunes the rf circuit as described in Sec. 2.1, and saturates by preventing additional rf voltage. Kishek describes this saturation and transient effects for resonators with various quality factors, and he determines a typical multipactor saturation time of 100 - 200 rf cycles [49, 50]. Riyopoulos discusses another saturation mechanism due to space-charge-induced debunching of the multipactor electron sheet [51]. This saturation occurs as a result of the mutual repulsion of the phase-focused electron sheet. The space-charge field defocuses the electrons by accelerating them ahead and behind the focused sheet, causing them to fall outside allowed phase range and impact with insufficient energy for secondary emission. This space-charge effect also changes the resulting energy distribution of the multipactoring electron, as will be shown in Chap. 5.

2.5 Multipactor Avoidance

As mentioned, multipactor is often an undesirable phenomenon, and avoidance can be critical in the operation of certain systems. Multipactor can be avoided in several ways. The first and most effective is to make the geometry unfavorable for multipactor at all frequencies of interest [9]. By designing vacuum rf systems in such a way, multipactor is unable to develop and limit the rf system. Unfortunately, the geometry cannot always be changed in this way. System geometries may have engineering constraints or may be fixed by the necessary boundary conditions as in a waveguide, and other methods must be employed to prevent multipactor.

Another method often used is to reduce the secondary electron coefficient of the multipactoring surface, such that an amplification in the number of electrons is not possible. As mentioned, surface roughening and other surface treatments have been shown to reduce $\delta < 1$ for the necessary energies and prevent multipactor from occurring. This method is often the most simple and favorable solution for systems in which the geometry is already specified.

Lastly, it is possible to suppress electron motion across the gap by DC electric fields [17, 52, 53]. By placing a large (~ 1 kV) DC bias between the rf electrodes, electrons cannot accelerate across the gap, and multipactor can be effectively eliminated.

The drawback of this approach is that many systems have physical or engineering constraints that will not allow such a DC bias.

2.6 Coaxial Multipactor Discharges and Motivation Continued

Multipactor discharges in a coaxial geometry

In the previous section, the parallel plate geometry was used to outline the basic principles of a multipactor discharge because of the linear electric field and analytically determined equations of motion. Yet, as mentioned in Chap. 1, multipactor can occur in a wide variety of geometries, and this work focuses on the coaxial geometry because of the wide use of coaxial transmission lines for rf power at VHF. Because the electric field in the coaxial transmission line is spatially non-uniform, as described in Sec. 2.2.2, no closed-form, analytic solution exists for the equations of motion, and they must be solved computationally. While the same general principles of phase-focusing and saturation hold for coaxial multipactor, the details of the discharge in this more complicated geometry have not been investigated to the extent of the parallel plate case. Also, because of the cylindrical geometry, the angular coordinate, theta, is included in the equation of motion and further complicates the electron motion. Eqn. 2.21 gives the 2-D equation of motion for an electron in a coaxial geometry like that shown in Fig. 2-5. This equation will be visited again in detail in Chap. 4 in order to simulate the particle trajectories in this coaxial geometry.

$$m(\ddot{r} - r\dot{\theta}^2) = F_r = -\frac{eV_o}{ln\frac{b}{a}} \frac{\sin(\omega t + \alpha)}{r} \tag{2.21}$$

Because of the non-linear equations and complicated theoretical approach, much less work has been done on coaxial multipactoring as compared to the parallel plate case. One might assume that this more complicated scenario would make coaxial multipactoring less likely, but this work will show that in fact the opposite is true. Furthermore, to the knowledge of the author, experimental data on coaxial multipactor is limited to that of Richard Woo, which aims to outline the multipactor susceptibility of coaxial electrodes [47, 54]. Computational work has been done for coaxial multipactoring by Somersalo and Yla-Oijala to determine the susceptibility and scaling laws for coaxial geometries [48, 52]. As a result, there is a scientific need for experimental data for discharges in these coaxial geometries, and this work provides this additional information while supporting the above listed references.

Motivation Continued

In both parallel and coaxial geometries, very little experimental work has been done to characterize these discharges. Beyond the parallel plate distribution functions presented by Höhn at 50 MHz and 5.5 cm electrode spacing, no data measuring coaxial or parallel plate distribution functions for a range of frequencies or variety of electrode materials exists in the literature. The focus of the Coaxial Multipactor Experiment [29] and this work is to provide detailed experimental data on coaxial multipactor discharges and the associated energy distribution functions at VHF in coaxial transmission lines. In addition, this work is also directed at measuring and understanding parallel plate multipactor discharges, for comparison to the existing data of Höhn and for comparison to the coaxial multipactor discharges of this study. As mentioned in Chap. 1, this work is in direct support of the rf systems in fusion experiments, and by understanding the differences in parallel plate and coaxial geometries which are both possible on Alcator C-Mod, the extent of the impact of multipactor on fusion experiments is determined. It will be shown in Chap. 6 that multipactor discharges in both mentioned geometries are possible on Alcator C-Mod, and these discharges limit rf operation. Understanding these discharges leads to better multipactor prevention techniques, which then leads to better rf performance on fusion devices.

Chapter 3

The Coaxial Multipactor Experiment (CMX)

The Coaxial Multipactor Experiment (CMX)[29] is a tabletop, testbed facility designed to investigate multipactor discharges in both parallel plate and coaxial geometries at various frequencies in the VHF range. Addressing the scientific need for experimental multipactor data, CMX provides the first detailed investigation of multipactor discharges and the associated electron distribution functions for various frequencies, geometries, and parallel plate electrode materials. While CMX specifically supports Alcator C-Mod and rf systems on fusion experiments, this research applies to any VHF rf system which has multipactor sensitive areas in vacuum. Because CMX is a small tabletop experiment, different multipactor scenarios are easily tested for larger experimental applications and interests. This chapter gives a detailed description of the experiment, its operation, and the main experimental results.

3.1 Rf Experimental Setup

CMX produces a multipactor discharge in a 25.4 cm, stainless steel (SS), six-way cross called the Multipactor Vacuum Chamber (MVC) capable of a base pressure of 5×10^{-8} torr. Fig. 3-1 depicts both the coaxial and the parallel plate multipactor configurations. In each case, the vacuum region is given by the shaded area. The MVC uses a manual gas bleed valve to introduce a variety of gases at different pressures. The transmission line vacuum windows are Myat 401-050 gas barriers with Viton o-rings and Teflon barrier.

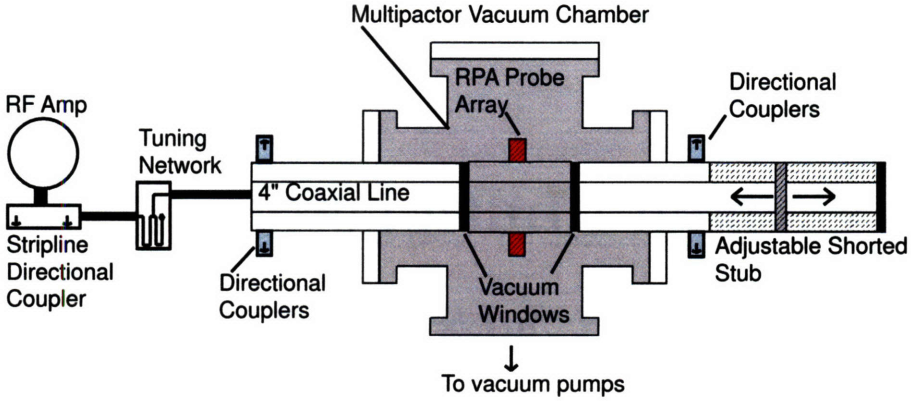

(a) Coaxial Multipactor Setup

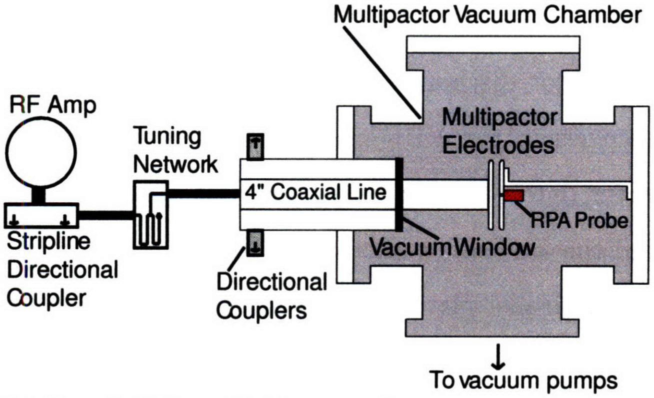

(b) Parallel Plate Multipactor Setup

Figure 3-1: CMX Experimental setup for both (a) coaxial and (b) parallel plate multipactor discharges.

CMX investigates multipactor discharges in the frequency range of 40-150 MHz with rf power up to 1 kW in the high Q resonator (typical Q$\sim$1500, coaxial; Q$\sim$500, parallel plate). Because of the high Q of the cavity, voltages of order 1 kV can be achieved in the unmatched section with a relatively low input power. A tuning network, consisting of a stub tuner and phase shifter pair, provides the appropriate impedance matching in order to minimize the reflected power to the source. Rf power measurements include several pairs of directional couplers: one on the matched side, and a pair on each side of the vacuum chamber, except in the parallel plate case, the last coupler pair is absent.

In the coaxial case, two vacuum windows allow the 50Ω, 10 cm outer diameter, copper transmission line to pass continuously through a 15 cm long vacuum section. This short length allows for less than 5% voltage variation in the vacuum section for the VHF frequencies of interest. By varying the length of an adjustable shorted stub at the end of the resonator, the maximum voltage of the standing wave pattern can be placed in the MVC. The multipactor discharge occurs in this coaxial region of the MVC. Both inner and outer conductors are cleaned for ultra high vacuum with no additional surface preparations; therefore, the coaxial conductors are placed into vacuum with a copper oxide layer. A detailed discussion of CMX vacuum preparation procedures is given in Sec. 3.3.

In the parallel plate case, the center conductor of the gas barrier is extended into the center of the MVC. One multipactor electrode is attached to the center conductor, and the other electrode is grounded to the MVC by an aluminum ground strap. A 2 cm teflon spacer prevents multipactoring in the short coaxial region of the vacuum window. The electrodes are 10 cm in diameter, spaced 1 cm to 3 cm apart.

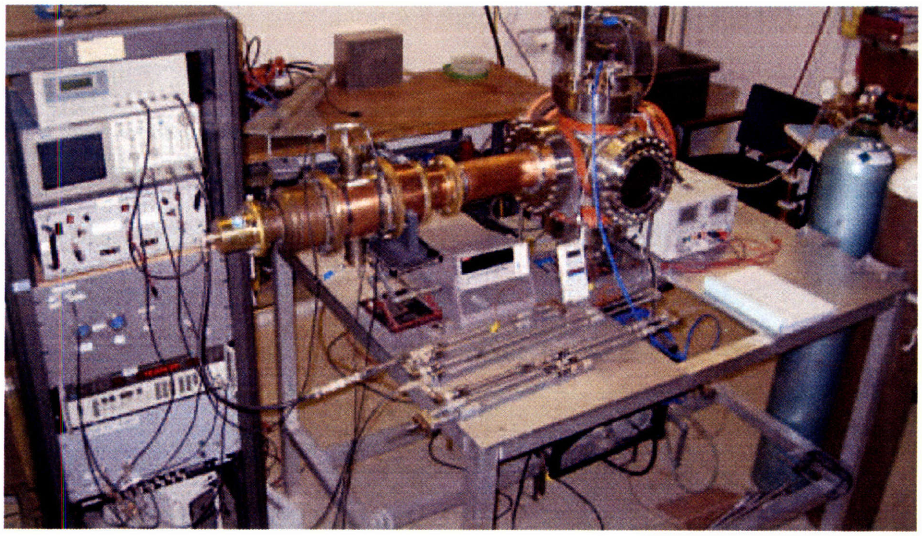

Figure 3-2: The Coaxial Multipactor Experiment in the parallel plate geometry.

CMX measures parallel plate multipactor discharges with stainless steel, glow

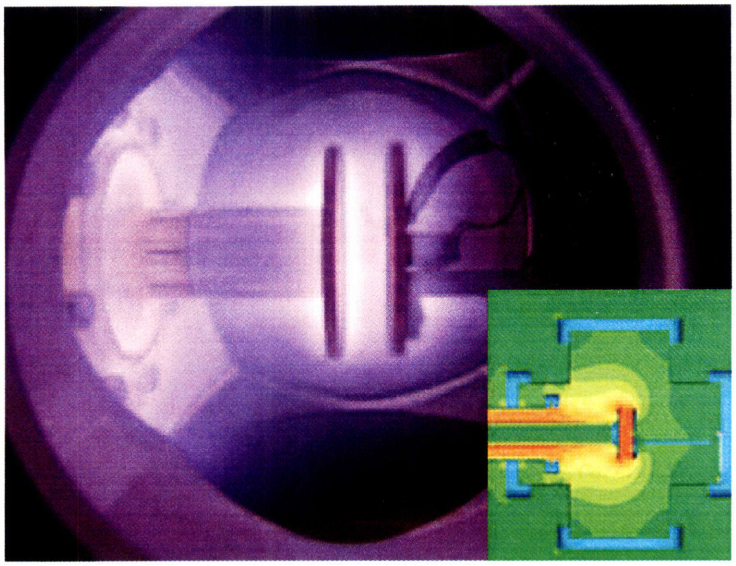

Figure 3-3: Argon rf glow discharge on copper, parallel plate electrodes. CST Microwave Studio was used to model the vacuum fields of the MVC, as illustrated in the lower right hand corner.

discharge cleaned (GDC) copper, copper with oxides, and titanium with oxides electrodes, with the added ability to test any additional electrode material thought to be of interest. These particular electrode metals were chosen because of their common use in rf systems and their varied secondary electron coefficients. In order to successfully produce the multipactor, these electrode materials have secondary emission coefficients $\delta \geq 1$ at the multipactor electron energy, as discussed in Chap. 2 [16, 35, 41]. The electrodes are typically vacuum conditioned by both multipactor and rf glow discharge. Efforts were made to remove the oxide surfaces of both the copper and titanium electrodes by means of argon rf GDC etching. The degree of the oxide removal was inferred by a change in the multipactor onset voltage, which is a result of the different secondary electron coefficients of the respective metal oxides. No direct measurement was made to determine the level of oxide removal by argon etch.

3.1.1 Rf power measurement

The CMX rf power is measured in three locations by directional couplers. On the matched side, before the tuning network, a -30dB stripline directional coupler measures forward and reflected power. On the unmatched side, after the tuning network, adjustable coaxial directional couplers measure the rf power with -50dB attenuation. The exact attenuation for each coupler at the proper frequency is calibrated by a network analyzer. All lines and couplers have a characteristic 50Ω impedance, and all connecting lines are calibrated to correct for cable attenuation.

Each coupler outputs a sinusoidal voltage signal which is proportional to the attenuated rf power. This signal is converted to a DC voltage by an rf diode, which is calibrated with a rf power meter. Each signal is digitized by a National Instruments 6071e digitizer and recorded by the Matlab Data Acquisition Toolbox package.

For each shot, rf data is taken for 3 seconds at a sample rate of 1 kHz and then averaged. Each rf signal is processed after each shot. Fig. 3-4 describes how the multipactor voltage is determined. Power and voltage conversions are done using Eqn. 3.1 and 3.2 for a 50Ω line.

$$P = \frac{1}{2}\frac{V^2}{50} \tag{3.1}$$

$$dBm = 10 \cdot \log\left(\frac{P}{1mW}\right) \tag{3.2}$$

The voltage in the location of the multipactor is not measured directly in either configuration, but is instead determined by the following methods. In the coaxial case, the MVC voltage is determined from the standing wave pattern in the unmatched section. Because the rf voltage is zero at the shorted stub, the voltage can be determined using the circulating power, P_{circ}, and the electrical length, L, from the short stub to the center of the MVC, described by Eqn. 3.3.

$$V_{MVC} = \sqrt{2 \cdot 50 \cdot P_{circ}} \cdot \sin(2\pi f \cdot \frac{L}{c}) \tag{3.3}$$

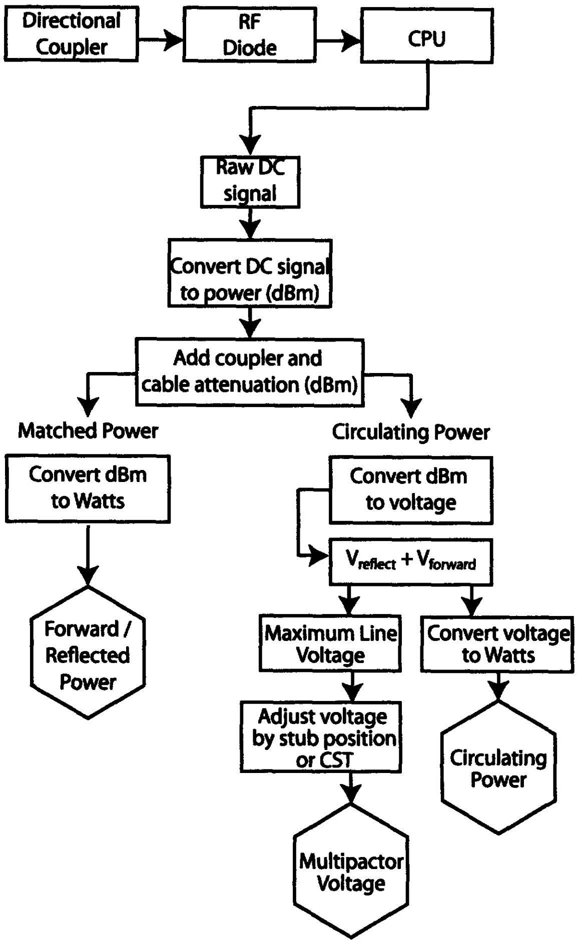

Figure 3-4: For each shot, forward/reflected power, circulating power, and multipactor voltage are calculated using this method. In order to determine the multipactor voltage, the stub position is used in coaxial experiments, and the CST simulation data is used in parallel plate experiments.

In the parallel plate case, the MVC voltage between the electrodes is determined by simulation using CST Microwave Studio [55] and a solid model of the rf system and vacuum chamber. Fig. 3-3 and Fig. 3-5 depict the magnitude of the vacuum electric fields in the MVC for the CST simulation. For 80 Mhz and a 3 cm gap, simulation data yields a MVC electric field, E, between the electrodes of 498 V/m for an excitation power, P_{excite}, of 1 W rf power. This electric field depends on the rf frequency, and the frequency-dependent simulation results are given by Table 3.1. The voltage between the plates is assumed to be approximately equal throughout the gap, although, in reality, this is not the case, as illustrated in Fig. 3-5. These non-linear electric field effects increase with frequency as the wavelength becomes shorter and closer to the MVC feature sizes, but the field remains sufficiently constant for the constant field approximation to hold for the VHF frequencies of interest. The parallel plate MVC voltage is determined by scaling the CST data with the circulating power and electrode spacing, d, by the following relationship,

$$V_{MVC} = E \cdot d\sqrt{\frac{P_{circ}}{P_{excite}}}. \tag{3.4}$$

Frequency (MHz)	E field (V/m)
50	436
60	439
70	470
80	498
90	523

Table 3.1: CST simulation data for the vacuum electric field between the parallel plate electrodes.

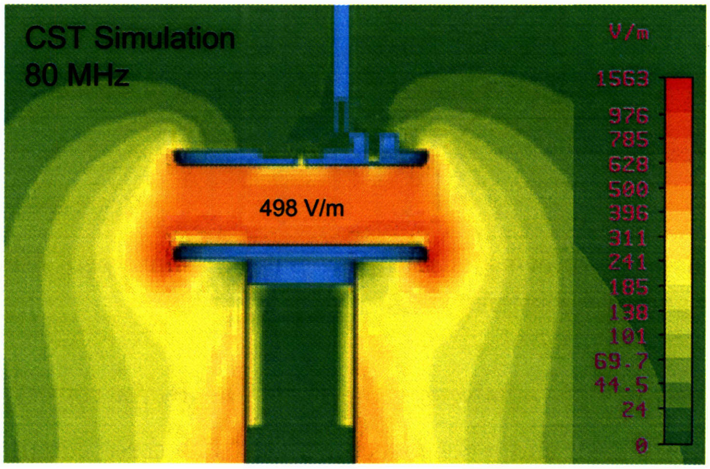

Figure 3-5: CST simulation results for the parallel plate region at 80 MHz and 3 cm electrode spacing. The non-linear electric field can be enhanced by a factor of 3 near the edges of the electrodes.

All voltage values in this work are given as peak rf voltages, as opposed to an RMS voltage. Lastly, electrical lengths of each rf component, including the adjustable length of the shorted stub, were determined with a network analyzer.

3.1.2 Multipactor current measurement

The multipactor current and electron energy distribution functions are critical components in all multipactor discharges. In CMX, the multipactor current and energy distribution functions are measured with retarding potential analyzers (RPAs). The same gridded analyzers are used in both coaxial and parallel plate configurations. RPAs collect electron current as a function of a bias voltage, forming an I-V characteristic [56]. This characteristic is then used to determine the distribution function as will be shown shortly in Sec. 3.2.

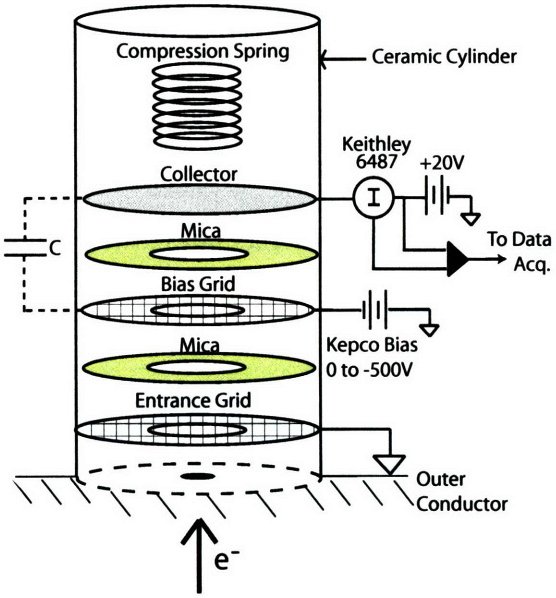

Figure 3-6: Schematic drawing of retarding potential analyzers used to determine electron current and distributions.

Fig. 3-6 illustrates the analyzer geometry. The RPAs consist of a grounded entrance grid, a bias grid, and a SS collector plate. The three components are separated and electrically isolated by 0.25 mm thick mica washers. The grids are made by spot-welding a 44% optical transmission, electroformed SS mesh to a 0.33 mm thick stainless steel washer. The grid mesh has an aperture size of 3 mm, which is much smaller than the electron Debye length of several centimeters inside the probe. The RPA can collect current densities as high as 30 A/m^2 before space charge limits the current within the RPA. The highest CMX multipactor current densities for a given bias voltage are of order 1 A/m^2 and far below that for space charge limitations. The RPA components are stacked inside a ceramic cylinder which is then mounted over an entrance aperture on the conductor of interest. A simple spring applies the necessary force to keep all RPA components aligned and the entrance grid in good electrical contact with the conductor.

In the coaxial geometry, twelve RPAs are arranged azimuthally around the outer conductor, while in the parallel plate geometry, a single RPA is placed in the center of the grounded electrode. In all cases, the multipactor current enters through a 3.2 mm entrance aperture. The through-hole depth of the aperture is 3.3 and 1.7 mm for the coaxial and parallel plate cases, respectively.

The bias grid is swept (0 to -500 V max) by a Kepco BOP 500M in order to collect the current as a function of bias voltage. In order to fully suppress any secondary emission from the collector, a minimum +20 V is maintained between the collector and bias grid by holding the collector fixed at +20 V while the bias grid voltage is swept negatively with a 1 Hz triangle waveform. The bias waveform is depicted in Fig. 3-7. The time trace of the collected current in the absence of multipactor is shown in the second panel of Fig. 3-7, which illustrates both the typical noise levels and displacement currents to be discussed shortly.

To determine the necessary voltage to fully suppress all secondary electrons from the collector, multipactor current was measured with suppression voltages from 0 to 30 V. At suppression voltages below 15 V, less current is measured due electron loss from the collector from secondary emission. At suppression voltages above 15 V, there is no change in the collected electron current, indicating sufficient suppression of secondary electrons from the collector.

A Keithley 6487 picoammeter measures the multipactor electron current from the collector. The picoammeter is held at the +20 V collector voltage relative to ground, and the ±2 V analog output is then input to a simple balanced differential amplifier with unity gain to subtract the bias voltage, as shown in Fig. 3-6.

Noise level voltages are maintained below 50 mV, and the signal voltage ranges from 0 to 2 volts from the Keithley 6487, providing a typical signal to noise ratio of

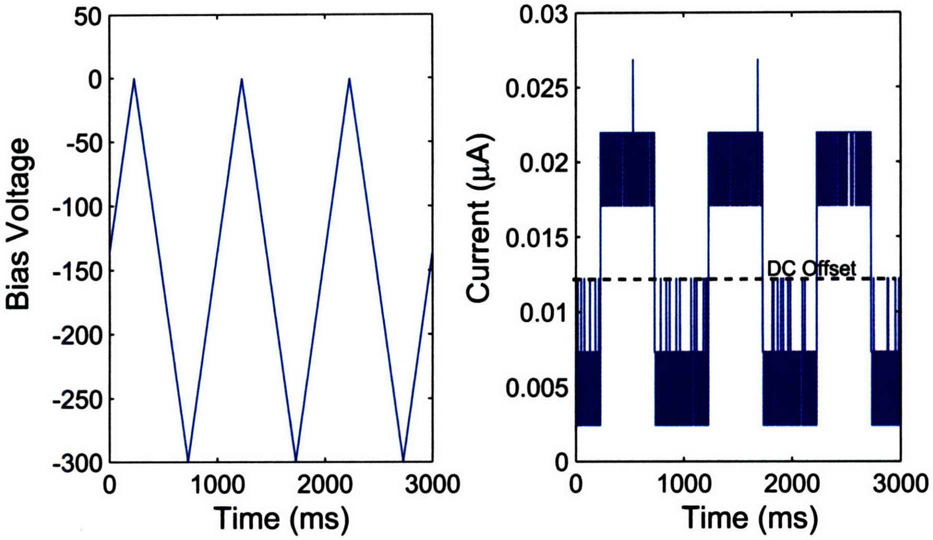

Figure 3-7: CMX voltage and current signals in the absence of multipactor. There was no observed changes in the measurements with the presence of rf voltage.

20. In the second panel of Fig. 3-7, the noise level of 10 μA corresponds to 10 mV, typical for all incoming signals. In order to keep noise levels to a minimum, electrical connections in vacuum are made by shielded coaxial wire with SMA connections to the vacuum electrical feedthrough. There was no change in the baseline signals (without multipactor) due to the presence of rf voltage. Also, all external electrical connections are made with shielded coaxial cable, and the differential amplifier power is filtered with 0.1 μF capacitors.

Careful attention was placed on stray capacitance and displacement current errors. Approximately 15 pF capacitance between the collector and bias grid accounts for the observed displacement current as the bias grid voltage is swept. Fig. 3-7 illustrates the displacement current seen as a square wave, which is proportional to dV/dt and the capacitance. The total capacitance between the collector and all surrounding components, including the bias grid and cable shields, can approach 100 pF or more; therefore, by holding the collector at fixed voltage and only sweeping the bias grid, the displacement current is minimized and is later averaged out using a smoothing spline function. Also, the bias grid is biased at a low frequency of 1 Hz to minimize dV/dt and the associated the displacement current. Because of the method to be described in Sec. 3.2, the 12 mV constant DC offset of the differential amplifier seen in the figure does not affect the inferred distribution function. Multipactor current and bias grid voltage data are recorded and digitized at 1 kHz for 3 seconds, or 3 full voltage sweeps.

3.2 Determination of Distribution Functions

Mathematically, the collected electron current per unit area is given by

$$j(V) = \int_{v}^{\infty} f(v')v'dv', \tag{3.5}$$

where $f(v)$ is the one dimensional velocity distribution function, and v is the electron velocity directed along the axis of the RPA. Using $V = \frac{mv^2}{2e}$ for the bias voltage and a change of variables in Eqn. 3.5,

$$j(V) = \int_{v}^{\infty} f(v')\frac{dv'^2}{2} = \int_{-V}^{\infty} \left[f(v') \cdot \frac{e}{m}\right] dV' = \int_{-V}^{\infty} F(V')dV' \tag{3.6}$$

The energy distribution function is then given by

$$\frac{\partial j(V)}{\partial V} = F(V), \tag{3.7}$$

where $F(V) = f(V) \cdot \frac{e}{m}$ [56]. Fig. 3-8 shows each step in the calculation of the distribution function for each shot.

After the multipactor current signal is amplified and extracted from the collector voltage, the data is digitized, and the I-V characteristic is smoothed by the Matlab Curve Fitting Toolbox smoothing spline function with smoothing parameter equal to 0.999 [57]. This smoothed characteristic is then differentiated numerically to give the electron distribution function. Examples of both the raw and smoothed CMX I-V characteristics and the corresponding electron distribution are shown in Fig. 3-9. The distribution function is shown in units of μA per volt with x-axis units of eV, matching that of the bias voltage.

The total collected current is determined by numerically integrating the distribution function. This method yields a collected current which agrees with the unbiased Keithley current measurement at steady state. To calculate the true multipactor current density, j, the collected current, I, is divided by the transmission coefficients of the two RPA grids, 0.44, and the collector area, 0.08 cm^2, shown by Eqn. 3.8.

$$j = \frac{I}{0.44^2 \cdot 0.08cm^2} \tag{3.8}$$

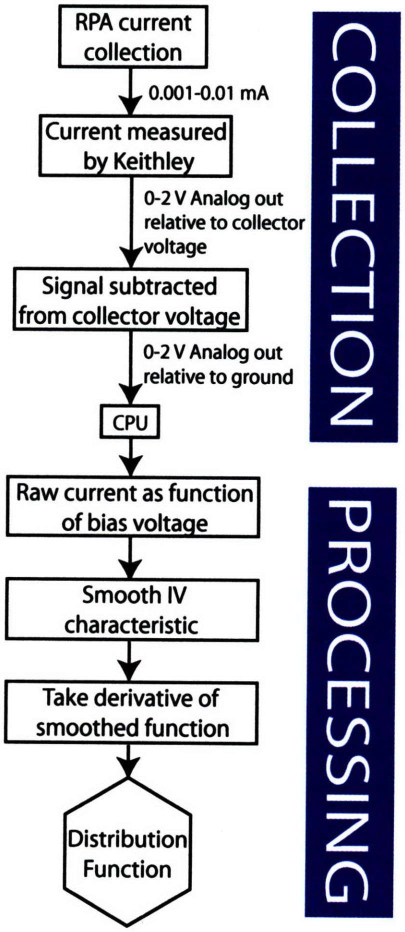

Figure 3-8: For each shot, the multipactor current is recorded and analyzed by this method. The electron energy distribution function is determined by taking the derivative of the IV characteristic.

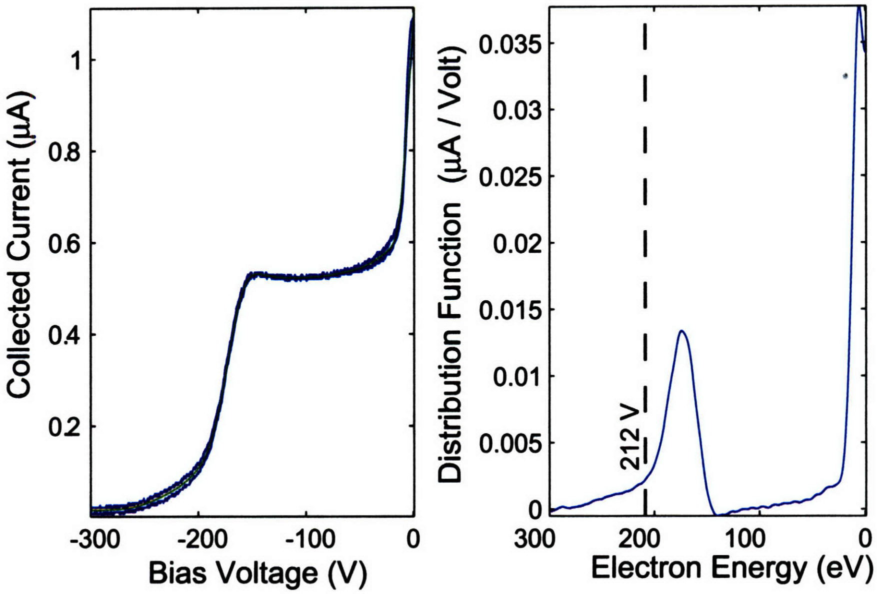

Figure 3-9: I-V characteristic and energy distribution function for coaxial geometry, 60 MHz, 3.2 W multipactor, $V_{MVC} = 212V$.

3.2.1 Distribution function error estimation

In order to estimate the uncertainty in the electron energy distribution caused by electronic noise, the standard deviation, σ, of the raw signal from the smoothing spline fit is first determined. Then using a normally distributed random number generator, random noise with a standard deviation of σ is added the the smoothed I-V characteristic to generate synthetic "raw data". This new "noisy" characteristic is then fit again by the same spline function, and the distribution function is determined by the same process described previously. This process is repeated many times and each time a slightly different distribution is generated within the fit error. In this way, an estimate of the upper and lower error bounds on the electron energy distribution function is obtained.

Fig. 3-10 illustrates the typical error bounds for CMX energy distributions. The distribution function error is approximately 10^{-3} μA per volt, which is roughly of order 5-10% of the measured current density for electron energies near the multipactor voltage. Errors in the inferred $F(V)$ also impact the total collected current

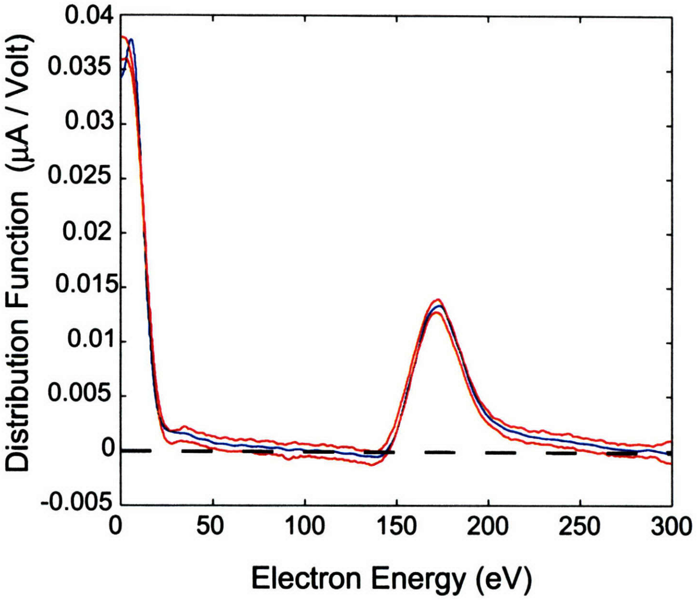

Figure 3-10: Energy distribution function for 60 MHz, V = 212V, coaxial geometry. Using the initial fit RSME of 0.0105, the error bands are determined by taking maxima and minima of 1000 fits using the process described in Sec. 3.2.1

measurement through the numerical integration of the distribution function. Upon numerically integrating all 1000 error distributions, the percent error of the average collected current measurement is 5.3%.

In some cases of large electron current, the distribution appears to dip below zero on the y axis, but no more than is allowed by the error, as seen in Fig. 3-10. Aside from fit error, a negative distribution function could also arise from insufficient secondary electron suppression from the collector, but as shown, this is a very small effect within the error bounds.

3.3 Experimental Operation

3.3.1 Vacuum and surface preparation

As previously mentioned, CMX provides a base vacuum pressure of 5×10^{-8} torr. In order to maintain this base pressure, the vacuum chamber is typically cleaned and baked for several days at 120°C at the start of each experiment cycle. Both coaxial and parallel plate electrodes are prepared for vacuum by abrasively cleaning to a moderately polished finish. They are then vacuum cleaned with alcohol before entering the chamber. Electrodes made of metals that form oxide layers, such as copper and titanium, enter the chamber with the oxide layer. In the case of copper, this oxide formed is Cu_2O, as this is the oxide which forms at ambient temperatures [37]. These oxide layers can be removed from the parallel plate electrodes by means of a rf generated, argon glow discharge at neutral pressures up to 100 mtorr and frequencies from 50-100 MHz. Glow discharge cleaning in the coaxial geometry was found to be impractical. Due to the low vacuum conductance [58] in the coaxial region, a plasma in the coaxial region interacts with the Teflon windows, which introduces a large amount of impurities that coat the electrode surfaces instead of being pumped out of the system. As a result, all coaxial electrodes have an oxide surface layer, and these electrodes are cleaned of any surface impurities by multipactor conditioning and long outgassing times on the time scale of weeks.

3.3.2 Experimental procedure

In order to initiate the multipactor discharge, the rf circuit is first tuned to the desired frequency with a network analyzer. The rf power is then manually increased in a stepwise manner, recording data at each power step as shown in the first panel of Fig. 3-11. At multipactor onset, the reflection coefficient increases proportional to the multipactor current, as shown in the second and third panels of Fig. 3-11. As the MVC voltage increases, the multipactor current increases until the multipactor pushes through the upper voltage limit, indicated as a drop in electron current and a jump in MVC voltage. Fig. 3-11 also depicts the electron energy distribution functions for each power step. These distributions increase in magnitude and energy with increasing rf voltage until push-through is achieved. A more quantitative description of the distribution functions with increasing MVC voltage is given in Fig. 3-12 and Sec. 3.4.1.

The multipactor heat flux is determined from the distribution function by Eqn. 3.9.

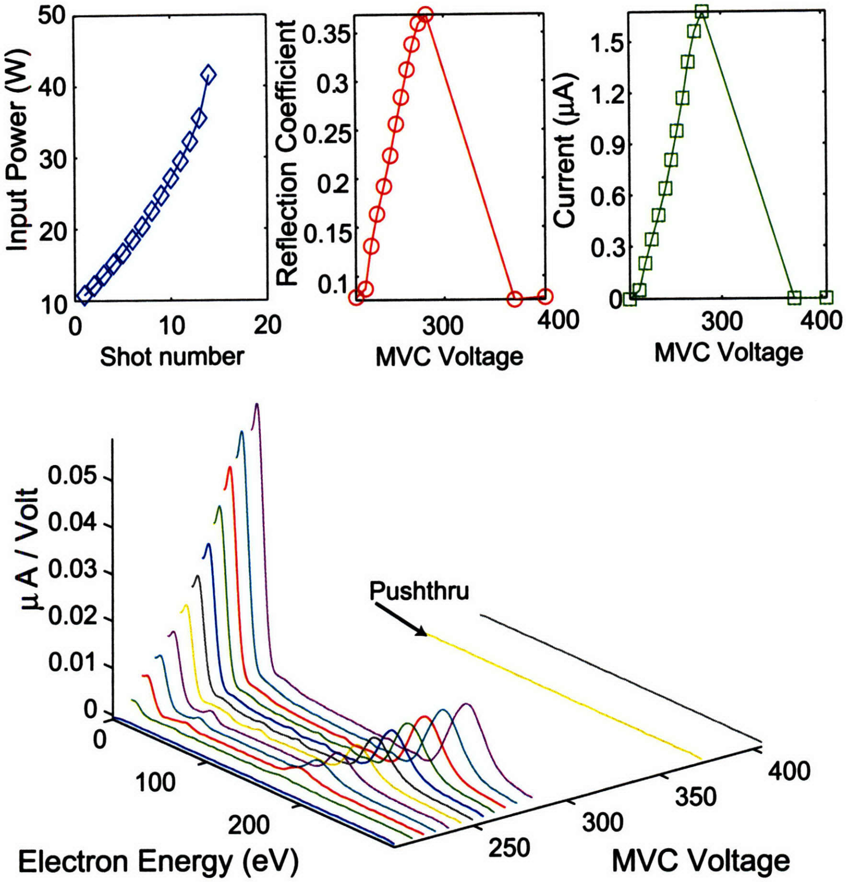

Figure 3-11: Rf and collected multipactor electron current data for 70 MHz, coaxial geometry, copper electrodes. The electron energy distributions at each MVC voltage are shown in the lower panel.

$$q'' = \frac{1}{|e|} \int E \cdot F(E) dE, \tag{3.9}$$

where q'' is the heat flux ($\frac{W}{m^2}$), and E is the electron energy. By multiplying q'' by the electrode surface area (471 cm^2, coaxial; 79 cm^2, parallel plates), the approximate power dissipated in the discharge is determined. This power is typically $10 - 15\%$ of the input power, 8 to 10 W maximum. It is an approximate determination because the lower energy portion of the distribution is altered by secondary emission within the RPA. This effect will be discussed further in Chap. 5.

3.4 Experimental Results

This section presents the experimental data sets for both coaxial and parallel plate multipactor discharges at various frequencies and geometries. Distribution functions, collected current measurements with MVC voltage, reflection coefficients, and multipactor susceptibilities are given for each of these geometries. The electrode spacing for the coaxial case was 2.82 cm, while the parallel plate electrodes were spaced at both 2.5 and 3 cm.

3.4.1 Coaxial multipactor distribution functions

Data were collected for coaxial multipactor discharges from 40 MHz to 150 MHz under several different conditions. All coaxial data are taken from discharges within the system described in Fig. 3-1, a 50 Ω, 10 cm outer diameter, coaxial transmission line, with base pressure below 10^{-7} torr. Results from azimuthal measurements in the coaxial case show no azimuthal spatial variation of the multipactor, so the following results are measurements from a single RPA. The same RPA was used in all coaxial multipactor measurements.

The coaxial data set is comprised of three main groups: Vacuum-prepared, clean electrode discharges, post-oxidation/surface impurity electrode discharges, and discharges at various base pressures (Chap. 6). The first group is used as the example of a typical coaxial multipactor, while the second group describes the effect of oxidation and surface impurities on the distribution functions.

Coaxial multipactor with vacuum-prepared electrodes

Fig. 3-12 illustrates the electron energy distributions for 70 MHz in a coaxial geometry with increasing rf voltage in the MVC. In each distribution, there is a low energy population below 50 eV and a second, higher energy peak which tails off near the MVC voltage, as seen in Fig. 3-12. As the rf voltage is incrementally increased, the high energy population of the distribution increases with the rf voltage until push-through is achieved, and the discharge then extinguishes. The peak of the high energy

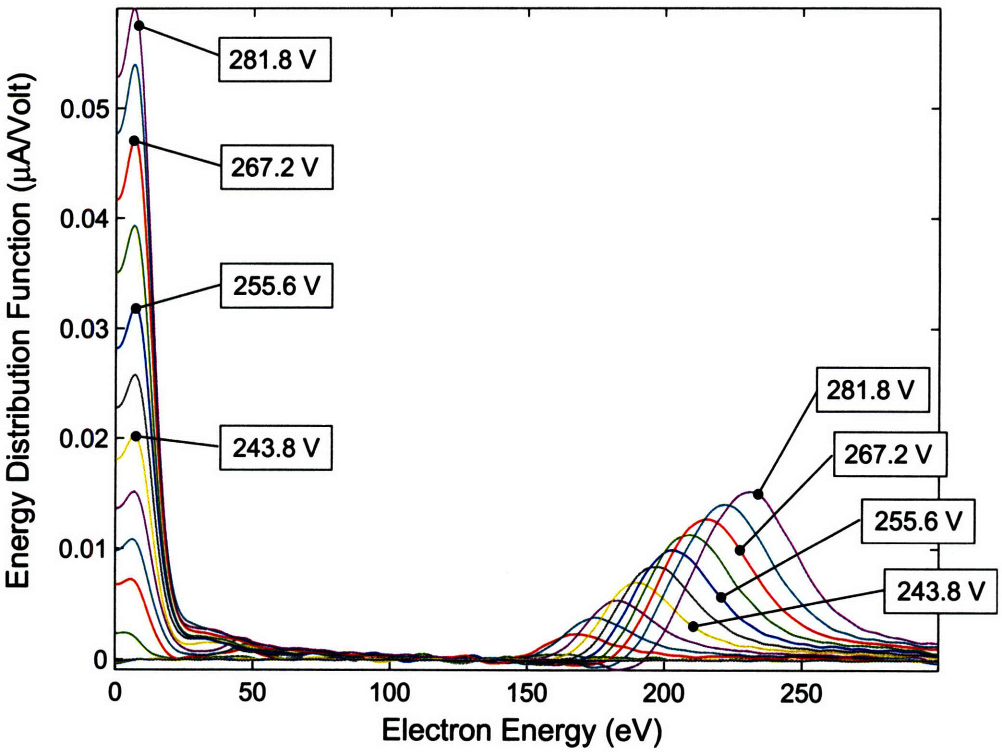

Figure 3-12: Multipactor energy distribution functions for 10 cm, 50 Ω, coaxial transmission line at 70 MHz. The electron energy increases with the rf voltages as shown by the 4 distributions with their associated rf voltage. The electron distribution drops at the V_{MVC}, but a high energy tail continues past this rf voltage.

population is located at an energy equal to 75 to 80% of the MVC voltage (see also Fig. 3-14). Also, the tail of the distribution extends past the MVC voltage, reaching zero approximately 50 volts past the rf voltage.

For properly cleaned and vacuum-prepared electrodes, multipactor discharges were measured from 55 to 150 MHz. Fig. 3-13 shows all distributions for this frequency range. Multipactor was not possible below 55 MHz for the clean electrode case. As the frequency increases, the energy of the electron distribution function increases nearly linearly. At 130 MHz, the distribution moves out of the voltage range of the RPA, and high energy electrons can no longer be measured with the 500 V bias supply. In addition, the reflection coefficient generally increases to as high as 0.5 with increasing electron current for all frequencies.

As will be shown in the following chapters, the most important aspect of the

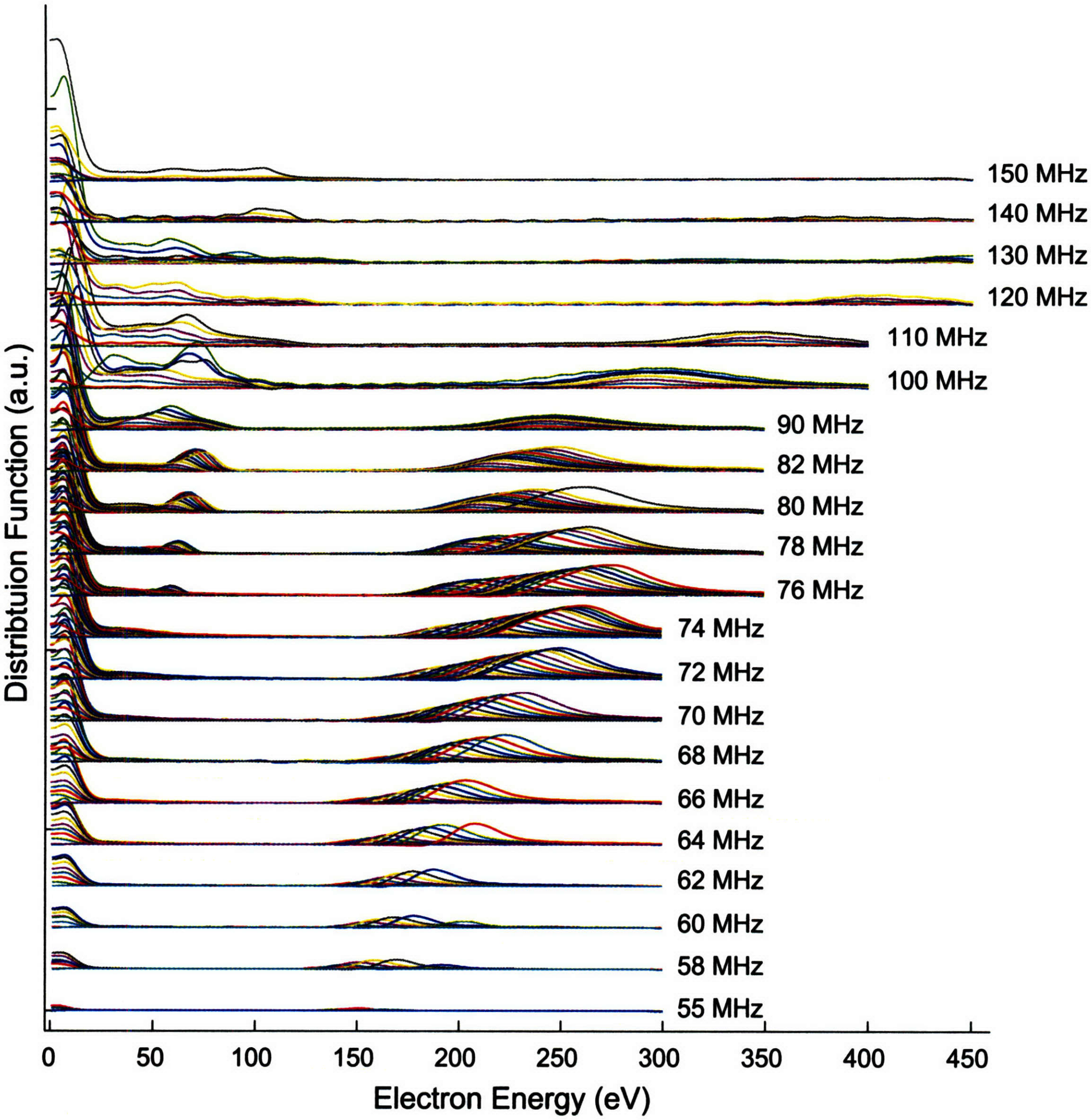

Figure 3-13: All energy distributions for coaxial multipactor from 55 MHz to 150 MHz.

distribution function is the high energy population, as it is this population which is responsible for sustaining the multipactor. Fig. 3-14 illustrates the peak energy of this population as a function both frequency and rf voltage. The first panel shows the energetic location (E_{peak}) of the high energy population, while the second panel gives E_{peak} relative to the MVC voltage for each shot and frequency. As mentioned, E_{peak} increases nearly linearly with frequency within the RPA range, but relative to the MVC voltage, the high energy population remains nearly constant at 80% until the

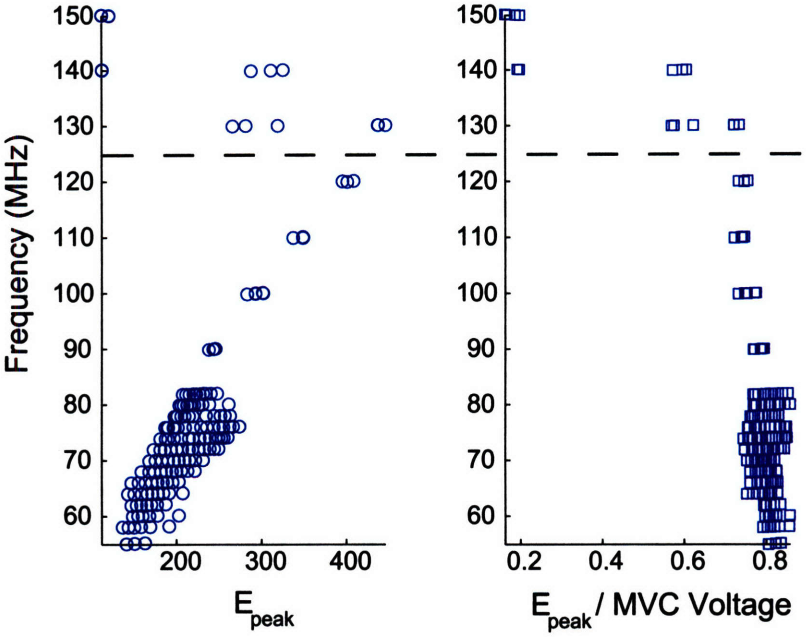

Figure 3-14: In the first panel, E_{peak}, the peak of the high energy population, is shown with frequency. The second panel shows E_{peak} normalized by the MVC voltage, which holds at 75-80% of the MVC voltage below 130 MHz. Above 120 MHz, the high energy distribution moves outside the RPA range.

distribution energy moves outside the RPA range at 120 MHz. For a given frequency, there is also a slight increase in the relative location with increasing MVC voltage, but it generally remains near 80%.

Also, the magnitude of collected electron current generally increases with frequency, shown in Fig. 3-15. This figure illustrates the collected current with rf voltage for all measured frequencies. The figure also indicates multipactor push-through, indicated by a sudden drop in collected current accompanied by a large jump in rf voltage. At 76 MHz and above, push-through was not possible given the relatively small available power of 50 W and the high reflection coefficient, but it is presumable that push-through would occur given sufficient forward power and reflected coefficient tolerance. This difficulty in push-through is thought to be a result of a high degree of electron resonance and the high number of electrons impacting with energy near δ_{max} [37].

In addition, there is an experimental observation of an increase in number of electrons at 50-75 eV for 76 MHz and above, is shown in more detail in Fig. 3-16. It was initially thought this population might be associated with the difficulty in push-through, but it will be shown in Chap. 5 that these electrons arise from new electron trajectories possible at the higher frequencies. As the cavity voltage increases, these trajectories are no longer possible, and these distributions are not present.

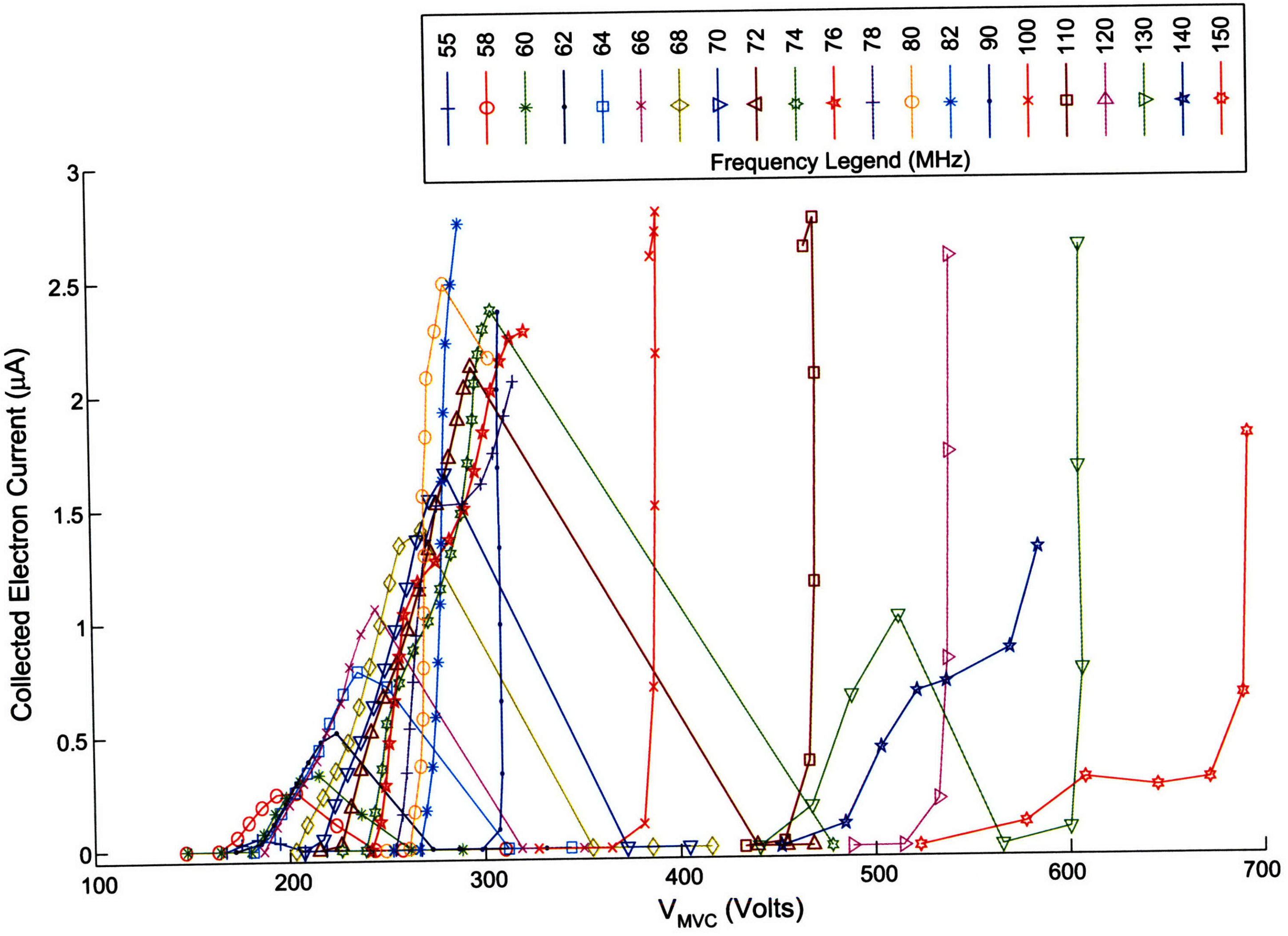

Figure 3-15: Collected electron current as a function of MVC voltage for frequencies 55 MHz to 150 MHz. Push-through can be seen as the current drops to zero while also jumping in voltage. Push-through was not possible above 76 MHz with the 50 W rf power source.

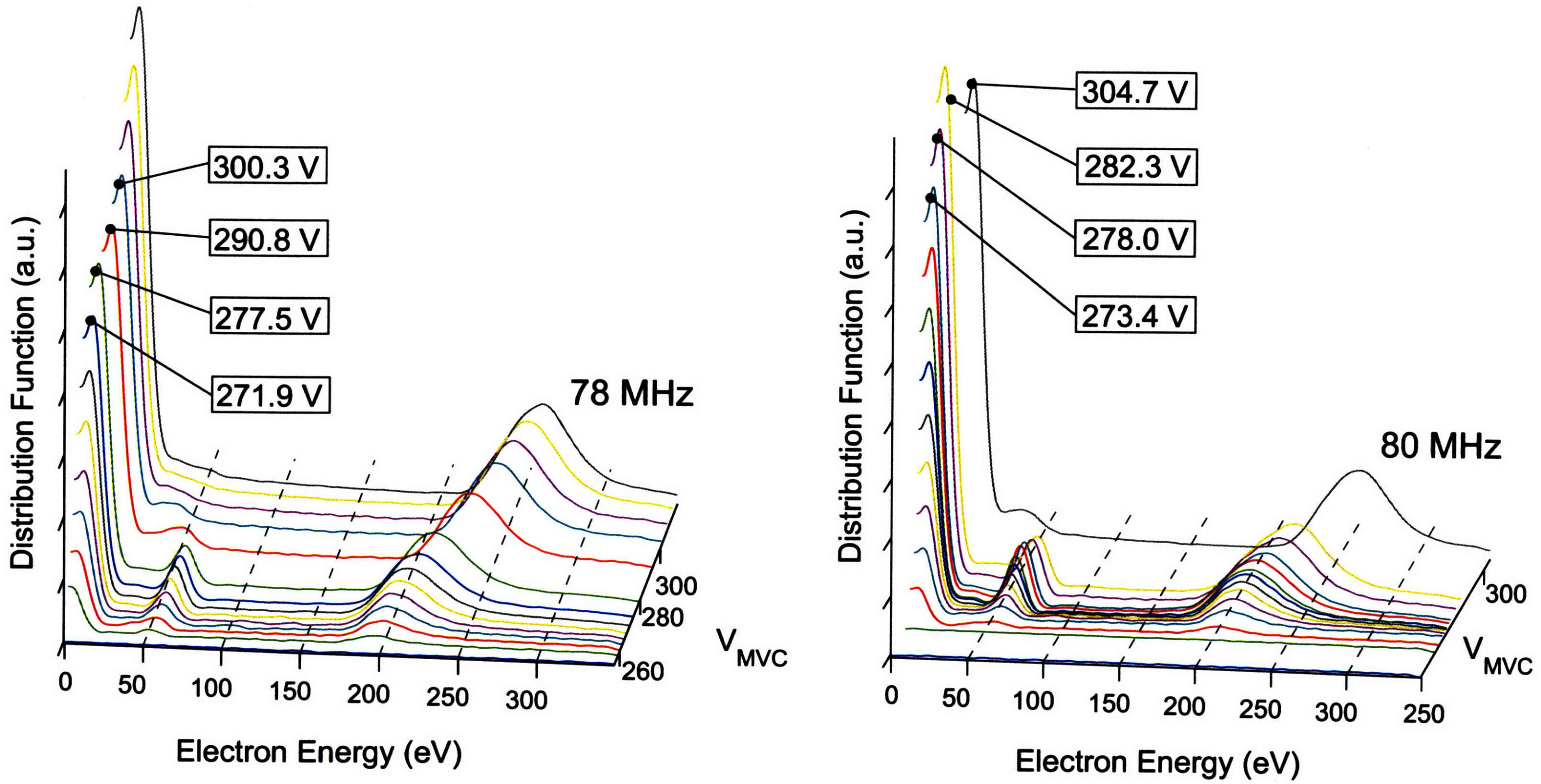

Figure 3-16: Electron distribution functions for 78 and 80 MHz. In each frequency case, the low energy (50-75 eV) peak is seen at lower voltage, and the location of the high energy peak remains fairly constant, as seen in Fig. 3-12. Eventually the high energy peak moves to higher energy with the rf voltage, and the low energy population disappears.

Coaxial multipactor with surface oxide and impurities

During conditioning experiments at 80 MHz, a power fault caused the turbopump to shut off and the gate valve to remain open. The pressure slowly rose by an unknown rate to a few millitorr in the chamber over the next few hours while the multipactor discharge continued. Eventually, as the pressure increased, the multipactor transitioned to a glow discharge inside the coaxial vacuum region. It is presumed that the multipactor and the glow discharge both interacted with the elevated level of neutral gases to cause a heavy oxidation of the coaxial electrodes [37]. Also, it is thought that the glow discharge interacted with the Teflon vacuum windows, introducing additional impurities to the electrode surfaces. No quantitative estimate of the level of oxidation or impurity generation was possible for this study.

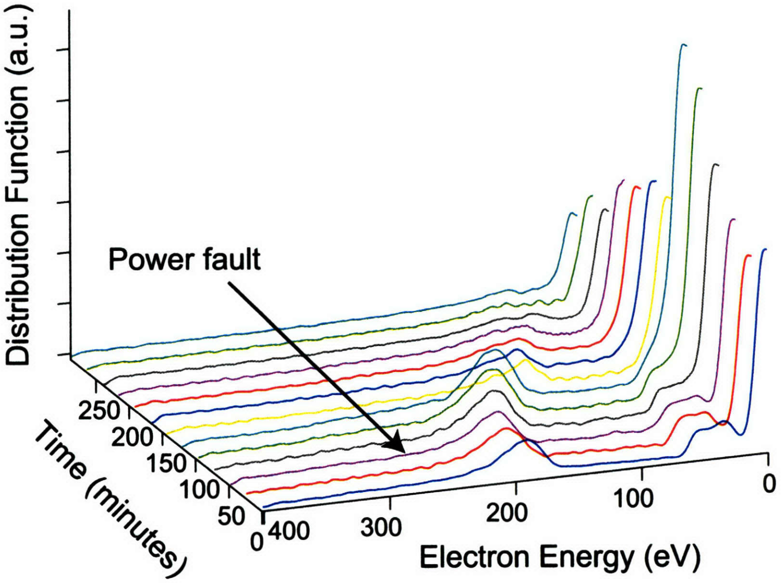

Figure 3-17: Energy distribution functions during a multipactor conditioning experiment. After approximately 50 minutes, a power fault occurred which turned off the turbopump while leaving the gate valve open. Subsequently, the coaxial electrodes were coated with an oxide coating and other surface impurities.

The important results of this pressure rise was the significant change to the characteristics of the multipactor discharge. Due to the fault, the coaxial electrodes yielded a much lower onset voltage as compared to the clean electrode case. This will be further described in Sec. 3.4.3. Fig. 3-17 depicts the evolution of the distribution function with time as the pressure slowly rose in the chamber. The distribution function decreased in energy as the pressure increased until the high energy population eventually vanished due to the onset of a glow discharge. Fig. 3-18 gives the distribution functions at 70 MHz after the oxidation/impurity event, illustrating the large change resulting from this event. This result suggests the importance of surface preparation for multipactor susceptible surfaces, as oxide and impurity coated surfaces greatly increase the susceptibility for multipactor. This will be discussed further in Chap. 6.

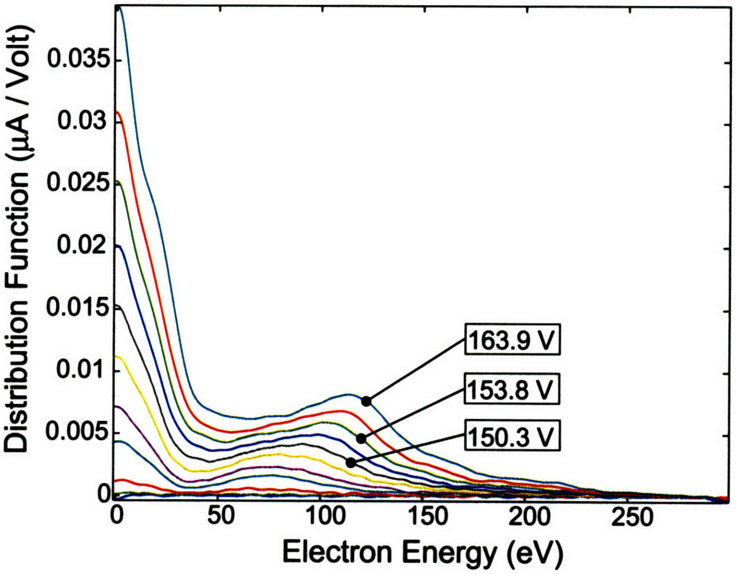

Figure 3-18: Distribution functions for 70 MHz after power glitch. The distribution function is much lower in energy due to oxidation and impurities on the conductor surface.

3.4.2 Parallel plate multipactor distribution functions

In order to make contact with the existing parallel plate multipactor data in the literature, several parallel plate experiments were performed on CMX to broaden the data set and determine consistency with the results of Höhn [5]. Multipactor discharges were investigated for copper, glow discharge cleaned (GDC) copper, stainless steel, and titanium with oxide electrodes, described in Sec. 3.1.

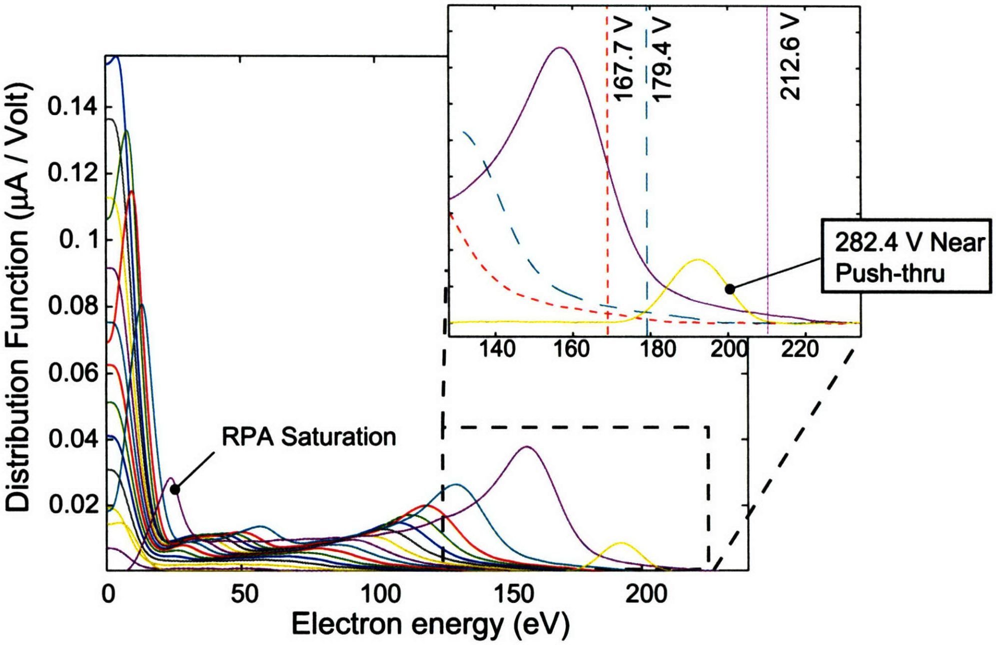

Figure 3-19: Parallel plate multipactor distribution functions for 60 MHz, copper with oxide electrodes, 2.5 cm gap. Each distribution before push-through tails off to zero at the MVC voltage, as seen in the zoomed section.

Parallel plate gaps of 1, 2.5, and 3 cm were investigated for copper. At 1 cm, no multipactor was possible from 50 MHz to 90 MHz, so the gap was increased to a minimum of 2.5 cm for the multipactor experiments. The gap was later adjusted to 3 cm to support multipactor discharges after glow discharge cleaning for frequencies between 50 MHz and 150 MHz. All other materials were tested with a 3 cm gap.

Fig. 3-19 depicts the multipactor distribution functions for each MVC voltage at 60 MHz. With the exception of cases near push-through, each distribution function tails off to zero near the MVC voltage. The last case with MVC voltage = 282.4 V is near push-through, indicated by a decrease in electron current.

For the parallel plate multipactor, the collected electron current scales with frequency similarly to the coaxial case shown in Fig. 3-15, but the current is generally higher for a given rf voltage and frequency. The magnitude of the collected current also depends on the electrode material, as illustrated in Fig. 3-20. The figure gives the collected current for pairs of copper and SS electrodes, and one pair of titanium

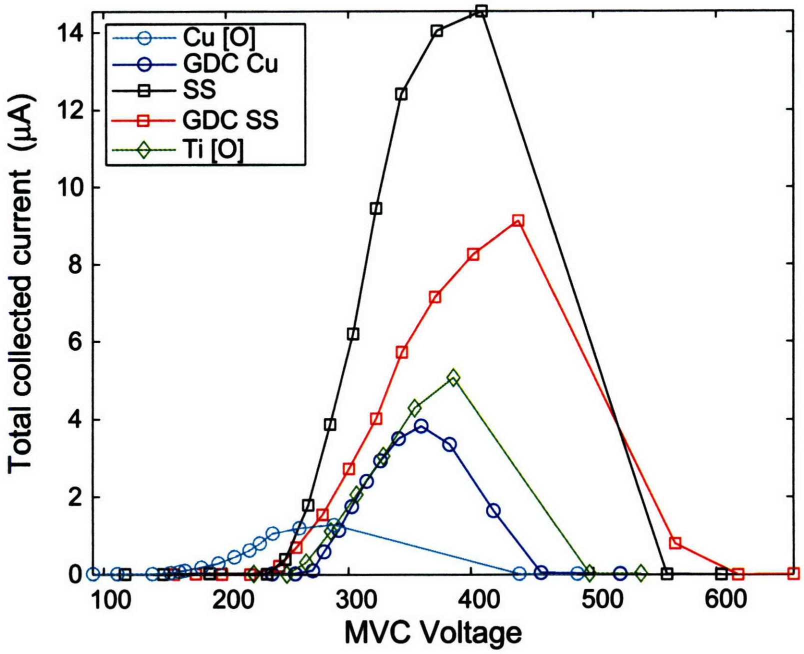

Figure 3-20: Collected current as a function of MVC voltage for 70 MHz and several different electrode materials.

electrodes.

For both copper and SS, the first electrode pairs (Cu, SS) have been placed in vacuum with minimal (less than 3 hours) of outgassing time and no multipactor or glow discharge cleaning. The second electrode pairs (GDC Cu/SS) have been processed with the Argon glow discharge to remove any surface impurities or oxide layers in the copper case.

The effect of the processing can be seen in Fig. 3-20. In the Cu case, surface impurities and an oxide layer are present on the electrode surfaces. Cu with Cu_2O oxide, represented as Cu[O], multipactor begins at a much lower voltage than in the GDC case (GDC Cu), where impurities and the majority of the oxide layer have been removed. In the SS case, processing the electrodes only reduces the multipactor current and does not change the multipactor susceptibility voltage. Because SS does not have an oxide layer, the processing only removes surface impurities. This suggests that the magnitude of δ is decreased, in contrast to an energy shift in δ with the removal of an oxide layer.

Comparing all three materials, SS electrodes give rise to the largest multipactor current, followed by titanium, and then GDC copper. Also, the voltage range in which the multipactor can exist before push-through has the same relationship between the different materials. SS has the largest range, next to titanium, and then copper. The multipactor range and current magnitude relationships between the different materials are due to the differences in the secondary electron coefficient, as discussed in Chap. 2. Higher multipactor electron current is expected for materials with higher secondary electron emission [5, 16, 35, 41].

For parallel plate multipactoring, the reflection coefficient for a given rf voltage and frequency is the same as the reflection coefficient for coaxial multipactoring, ranging from 0 to 0.5, despite the larger collected current in the parallel plate case. The approximate power absorbed by the parallel plate multipactor is typically 1-4 W, much less than the coaxial multipactor due to the surface area ratio of $A_{coaxial}/A_{pp} = 6$.

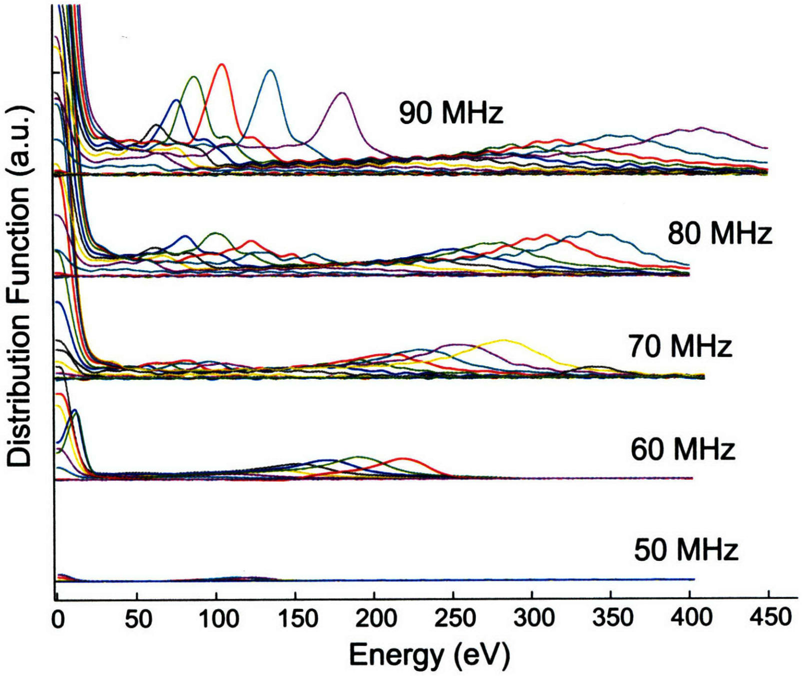

Figure 3-21: Distribution functions for glow discharge cleaned, SS electrodes, 3 cm gap, for various frequencies.

Fig. 3-21 depicts distributions at several frequencies for glow discharge cleaned, SS electrodes. The figure illustrates the relative size of the distributions at the different frequencies. At 50 MHz, the high energy peak can hardly be seen in comparison. Also, notice at 80 and 90 MHz, a low energy population near 100 eV of comparable size to the high energy population can be seen. Similar distributions are seen for both copper and titanium electrodes.

Similarly to the coaxial case, the energetic location of the high energy population within the RPA range is shown in Fig. 3-22. In general, for frequencies of 50 to 90 MHz, the high energy population is near 70% of the MVC voltage, as compared to 80% for the coaxial case.

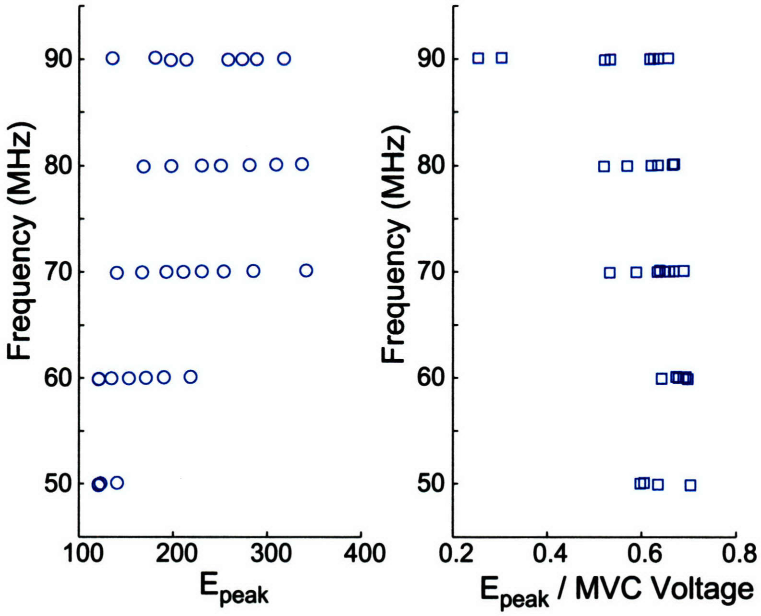

Figure 3-22: The energy value of the high energy distribution peak, E_{peak} with frequency. Also shown in the second panel is E_{peak} normalized by the MVC voltage.

3.4.3 Multipactor susceptibility curves

As mentioned in Chap. 2, multipactor susceptibility curves provide the voltage onset of the multipactor discharge at a given frequency and distance. Such curves exist for most common geometries, such as parallel plate and coaxial geometries [1, 47]. The curves often scale as $V_{suscept} \propto (f \cdot d)^2$ [1, 48], and these scaling laws for CMX multipactor discharges in both coaxial and parallel plate geometries will be discussed in Chap. 5. Also, while the upper limit of the multipactor was not specifically investigated in this study, the multipactor voltage band between onset and push-through was typically seen to be 200-400 volts wide for frequencies between 50-100 MHz and centimeter sized gaps.

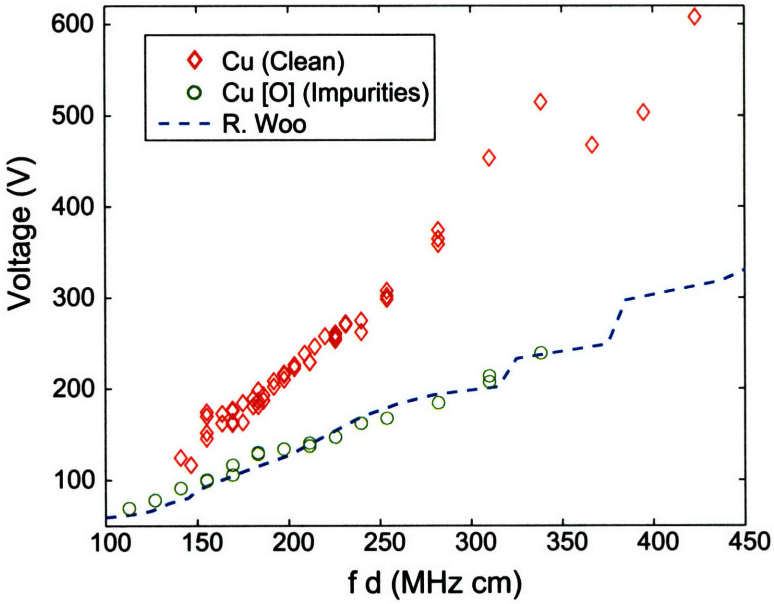

Figure 3-23: CMX coaxial multipactor susceptibility for 50Ω copper transmission line with electrode spacing of 2.82 cm. The dashed line represents Woo's coaxial data of the same geometry and Cu[O](Copper with oxide) electrodes for comparison to the CMX post-oxidation data. [47]

Fig. 3-23 depicts the multipactor susceptibility for all coaxial multipactor data sets. Initially, the vacuum system had been baked to 120°C, multipactor conditioned, and then held under vacuum conditions. These data combine to give the susceptibility relation for vacuum-prepared, 50Ω, 10cm copper coaxial transmission line. Fig. 3-

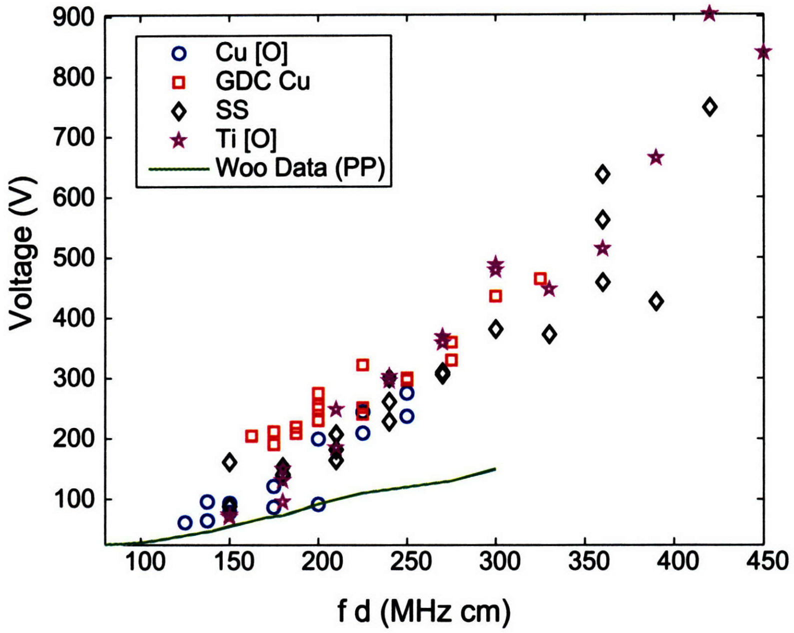

Figure 3-24: CMX parallel plate multipactor susceptibility for Cu[O], GDC Cu, SS, and Ti[O] electrodes, as compared to the experimental parallel plate data of Woo [47].

23 also illustrates the voltage lowering effect of surface oxides and impurities on the electrodes, represented by Cu[O] meaning copper with oxides. The Cu[O] data clearly show this decrease in the multipactor onset voltage. This data agrees very well with R. Woo's experimental data [47, 54] within reasonable error, shown as the dashed line in Fig. 3-23. In his experiment, no effort was made to remove any of the oxide layers or to allow time for outgassing of surfaces.

The same susceptibility curves are determined for the parallel plate geometry of CMX. Fig. 3-24 illustrates the parallel plate susceptibility for multiple electrode materials as compared to the experimental parallel plate data of Woo [47]. The GDC Cu data, represented by the red squares, compared to the Cu[O] electrodes, seen as blue circles, illustrate the effect of Cu_2O removal by plasma etch. The etched copper surface has a higher susceptibility voltage, and no multipactor was possible below 75 MHz, in contrast to the Cu[O] case which begins multipactoring at 50 MHz (2.5 cm gap). The differences in the susceptibility curves for the different electrode geometries will be discussed in Chap. 5.

Other parallel plate electrode materials tested on CMX were GDC titanium, titanium nitride, and copper sandblasted with 50 μm aluminum oxide. For the etched titanium electrodes, the multipactor was eliminated if the rf discharge was maintained for many hours, and the multipactor test was done immediately after turning off the plasma etch. This indicates successful removal of the high δ oxide layer by plasma etch. The etching process exposes the pure titanium with $\delta < 1$ for all energies, suppressing the multipactor until the oxide layer reforms as the surface reoxidizes with slow vacuum leakage.

Both titanium nitride coated electrodes and sandblasted copper electrodes were also tested in order to determine their ability to reduce the secondary emission coefficient for multipactor avoidance, specifically for use on Alcator C-Mod. Both these materials and tests will be discussed in Chap. 6 in more detail. Titanium nitride was unsuccessful in eliminating multipactor for frequencies of 50-100 MHz and an electrode gap of 3 cm, and the reasons behind this will be discussed in Chap. 6 and in [43]. On the other hand, no multipactor could be detected for sandblasted copper electrodes at the same frequencies and gap size after sufficient in-situ vacuum preparation. This result is also discussed further in Chap. 6.

Chapter 4

Monte Carlo Multipactor Simulation

In order to better understand the underlying physics of the multipactor distribution functions described in the previous chapter, a 1-D Monte Carlo, particle-tracking simulation was developed. The goal of the code is to compute electron multipactor distributions by simulating the same geometric and rf conditions of CMX and allowing secondary emitted electrons to move according to the electromagnetic forces within the transmission line. The code is adapted to simulate both parallel plate and coaxial transmission line geometries of any given size.

The basic premise behind the code is to launch an electron into the electric field, appropriate for the chosen geometry, and move the electron until it impacts an electrode. The simulation incorporates Monte Carlo (MC) techniques for initial conditions of each secondary emitted electron. Each electron is emitted at an electrode surface with an energy chosen statistically, but randomly from the proper secondary emission model, described by Eqn. 2.14.

The simulation launches a specified number of electrons at a specified phase, α, or phase distribution relative to the rf electric field. It also assumes a step function for δ, such that δ=0 for $E<E_1$, and δ=1 for $E>E_1$, where E_1 is the minimum energy for which δ=1. This approximation to actual secondary yield is appropriate for this simulation, and it will be shown in Sec. 4.3 that the approximation does not affect the resulting distribution functions. Yet, as a consequence of this assumption, the simulation does not provide any information on the growth rate or susceptibility of the multipactor.

4.1 Monte Carlo Sampling

The secondary emission energy distribution function describes the probability of a particular electron emission energy and is subsequently also called a probability distribution function (PDF). This PDF can also be represented as a cumulative distribution function, CDF, which provides the cumulative probability for a particular range, which in this case is the energy range. The first step in mathematically determining the CDF is to normalize the PDF so that the integral is unity, shown by Eqn. 4.1a, where A is the normalization constant, and $f(x)$ is the PDF bounded by x_{min} and x_{max}. Once the normalization constant is determined, the CDF is found by integrating the normalized PDF, as in Eqn. 4.1b [59].

$$1 = \frac{1}{A}\int_{x_{min}}^{x_{max}} f(x) \cdot dx \tag{4.1a}$$

$$CDF = \frac{1}{A}\int_{x_{min}}^{x} f(x) \cdot dx \tag{4.1b}$$

For the secondary electron emission PDF described by Eqn. 2.14, the associated CDF is given by Eqn. 4.2a. This CDF yields the cumulative probability of an electron being born with energies between E$_{min}$ and a particular energy E. If E is equal to E$_{max}$, then all energies are included in the probability, and the CDF should equal unity.

$$CDF = \frac{1}{A}\left[\frac{\phi}{3(E+\phi)^3} - \frac{1}{2(E+\phi)^2} + \frac{1}{6\phi^2}\right] \tag{4.2a}$$

$$A = -\frac{1}{2(E_c+\phi)^2} + \frac{\phi}{3(E_c+\phi)^3} + \frac{1}{6\phi^2} \tag{4.2b}$$

For these models, the minimum emission energy of zero and maximum energy of E$_c$ = 50eV are used. As in Chap. 2, ϕ is the material work function. Fig. 4-1 depicts the PDF and CDF for the emitted secondary electron energy. As an example, the figure shows an 80% probability that the emitted electron will have an energy between 0 and 10 eV.

In order to best reflect the physical environment, the emitted electron energy must be chosen randomly from the CDF of Fig. 4-1. The CDF is sampled by choosing a random number between 0 and 1 and finding the corresponding energy on the x-axis. When this is repeated many times, the numerically determined, emission energy distribution will have the same form as f(E) shown in Fig. 4-1 with error related inversely to the square root of the number of samples [60].

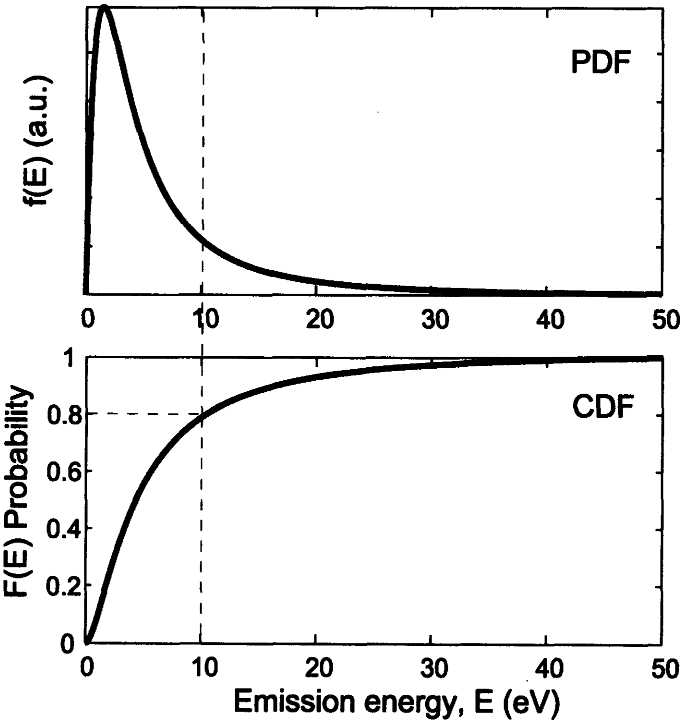

Figure 4-1: Emitted energy distribution function or PDF for secondary electron emission [39] and the corresponding cumulative distribution function, CDF.

Two variables, the electron emission energy and the emission angle, are sampled by the MC process described above. As mentioned in Chap. 2, the angular distribution is a cosine distribution, and is randomly sampled by the equation $\theta = \sin^{-1}(2\Upsilon - 1)$, where Υ is a random number between 0 and 1. Lastly, the electrode variables, ϕ, E_F, E_1, are chosen for the appropriate electrode material from tabulated data in the literature [4, 35, 36].

4.2 CMX Simulation Description

The basic operation of the code is described by Fig. 4-2. Both parallel plate and coaxial multipactor simulations operate with this same general procedure. In each case, the simulation is initialized with the rf frequency, peak rf voltage, number of particles, electrode properties (ϕ, E_1), and electrode geometry (coaxial or parallel plate; electrode spacing). The electron is then started at a particular electrode with a MC energy and angle, $t_{rf} = 0$, and a relative phase to the rf field. The electron is then moved by the appropriate electric fields of specified rf voltage and frequency for the given geometry until either electrode is reached. When an electrode is hit, the impact energy, time, relative phase, and initial conditions (velocity and angle) are recorded. If the impact energy is sufficient for secondary emission, i.e. $E > E_1$, a new electron is emitted from the impacted electrode at the corresponding impact time. This process is continued until the electron impacts with insufficient energy for secondary emission. At that point, a new electron is launched, and the procedure is repeated.

After running the simulation for a given number of electrons, the output includes electron distributions for the impact energy, time, phase, impacted electrode, and the initial angle and energy. As mentioned, the starting phase is provided as an initial condition. Typically, each electron is started with a relative phase of zero. To determine the effect of the starting phase on the simulation output, several iterations can be performed using the output phase distribution as the starting phase of the new simulation. This is then repeated until there is no change in the output distributions.

For a given rf voltage and geometry, a single electron can "bounce" between the two conductors many times if resonant conditions are met. The total number of electrode impacts, or hits, divided by the number of particles, ζ, can give a qualitative indication of whether resonant conditions are satisfied by giving a "degree of resonance". For instance, if $\zeta < 2$, electron resonance is low, and electrons impact with

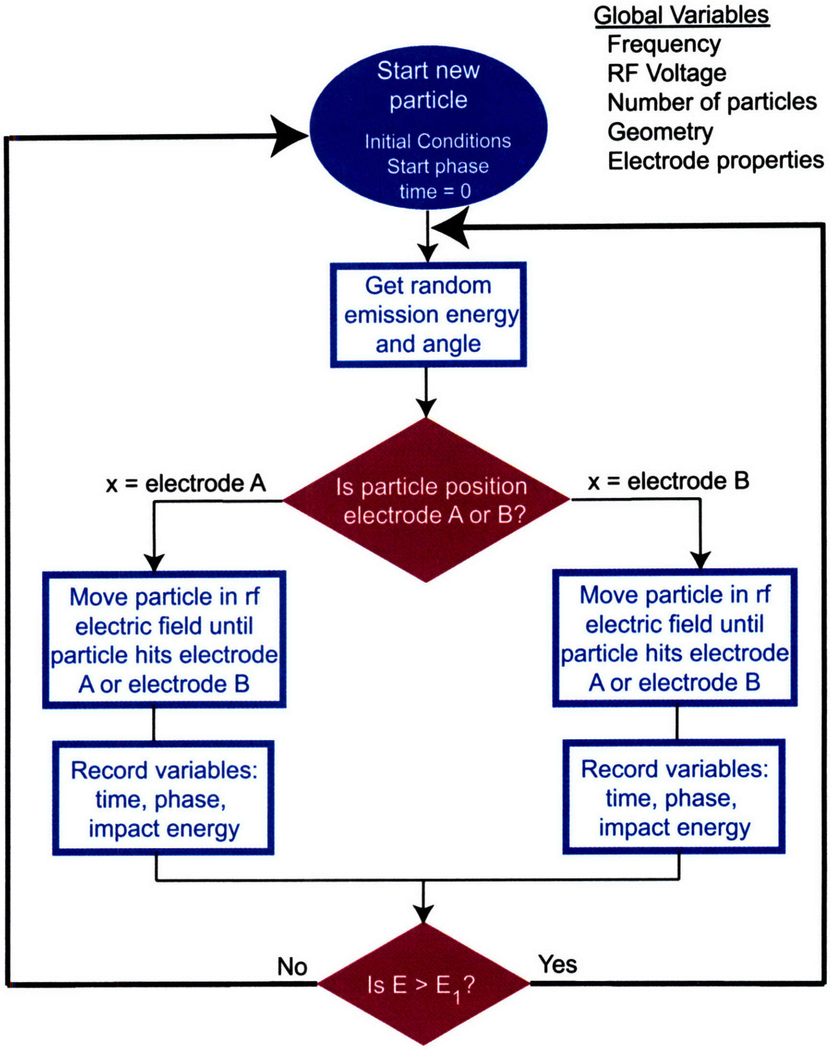

Figure 4-2: General flow chart for the CMX Monte Carlo multipactor simulation. Both coaxial and parallel plate multipactor simulations operate in the same manner. The simulation output includes electron distributions for impacted electrode, impact energy, time, phase, initial angle, and initial energy.

$E<E_1$ more often than not. In reality, no multipactor will exist given the same parameters. When experimentally-determined, multipactoring parameters are used in the simulation, ζ can be on the order of 100 or larger, indicating a strong multipacting electron resonance.

The difference between parallel plate and coaxial multipactor simulations arises within the electric fields which accelerate each electron. For the parallel plate case, the electric field is linear. The equations of motion are determined analytically and given by Eqns. 4.3 for an rf voltage of the form $\frac{V_o}{d}\sin\omega t$. For these equations, the electron is born at $t = \frac{\alpha}{\omega}$ relative to the rf voltage. The electron motion and position are advanced in time increments of 5000 steps per rf cycle until the electron impacts either electrode.

$$v = v_o + \frac{eV_o}{m\omega d}\left(\cos(\alpha) - \cos(\omega t)\right) \tag{4.3a}$$

$$x = x_o + \frac{v_o}{\omega}(\omega t - \alpha) + \frac{eV_o}{m\omega^2 d}\left[\sin(\alpha) - \sin(\omega t) + \cos(\alpha)(\omega t - \alpha)\right] \tag{4.3b}$$

$$v_o = \sqrt{\frac{2|e|}{m}E_{MC}} \cdot \cos(\theta_{MC}), \tag{4.3c}$$

where m is the electron mass, e is the electron charge, ω is the rf angular frequency, α is the relative phase, x_o and v_o are initial position and velocity respectively, V is the rf voltage, E_{MC} is the randomly chosen emission energy, and θ_{MC} is the randomly chosen emission angle.

In the coaxial multipactor simulation, the electric field is proportional to $\frac{1}{r}$, therefore the equations of motion must be solved numerically. In addition, because of the nature of the coaxial geometry, the electron's angular momentum must be included due to possible electron trajectories around the inner conductor. While the Lorentz force is purely radial, the acceleration in cylindrical coordinates also includes an angular term, shown in Eqn. 4.4.

$$a_r = \ddot{r} - r\dot{\theta}^2, \tag{4.4}$$

where in this case, θ is the angular displacement. The equation of motion then becomes

$$m(\ddot{r} - r\dot{\theta}^2) = F_r = -\frac{eV_o}{ln\frac{b}{a}}\frac{\sin(\omega t + \alpha)}{r}, \tag{4.5}$$

where a and b are the inner and outer conductor diameters, respectively. Using the definition and conservation of angular momentum, L, the equation of motion becomes

$$\frac{d^2r}{dt^2} = -\frac{eV_o}{m \cdot ln\frac{b}{a}} \frac{\sin(\omega t + \alpha)}{r} + \frac{L^2}{m^2 r^3} \tag{4.6}$$

It is Eqn. 4.6 that is solved in the coaxial multipactor simulation using a Runge-Kutta solver with 1000 time steps per rf cycle. The angular momentum is determined from the initial position and the energy/angle MC variables, θ_{MC} and E_{MC}, described by Eqn. 4.7.

$$L = mr \cdot \sin(\theta_{MC}) \cdot \sqrt{\frac{2|e|}{m} E_{MC}} \tag{4.7}$$

4.3 Simulation Results

Simulations can be run for all ranges for frequencies, rf voltages, electrode spacing, and electrode materials. This flexibility will be used in the Analysis chapter to compare the experimental results to the appropriate simulation results and understand the electron distributions under various conditions. This section illustrates typical simulation results for both parallel plate and coaxial multipactor. Fig. 4-3 gives an example of multipactor energy distribution functions with increasing rf voltage. As in the experimental case, the electron impact energy distribution increases in energy with the rf voltage, and maximum current occurs when the voltage yields the highest resonance for a given frequency and geometry. When the voltage is too low for the multipactor resonance, most electrons are immediately lost on the first impact due to insufficient energy for secondary emission, i.e. $\zeta < 2$. As the rf voltage increases into the range for multipactor, Fig. 4-3 initially shows an increase in both ζ and the number of electrons due to the higher degree of electron resonance. The highest degree of resonance occurs in this figure near 220 V. Yet as the voltage increases beyond 220 V, multipactor becomes less favorable, and both ζ and the number of electrons decrease.

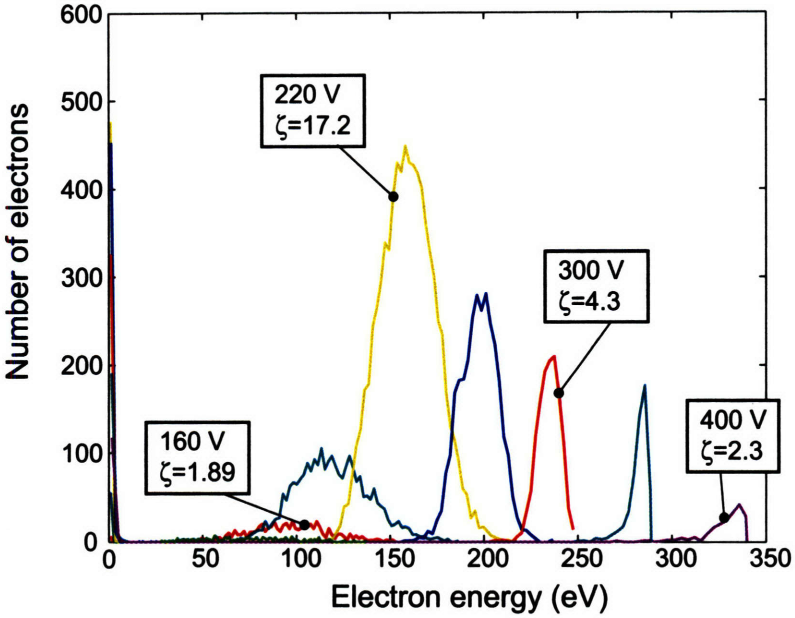

Figure 4-3: General simulation results for various rf voltages for 60 MHz and parallel plates spaced 3 cm apart. As the voltage increases, the multipactor resonance condition is satisfied, and electrons begin to "bounce" between the electrodes ζ times. As the voltage increases above the multipactor resonance, multipactor cannot be supported to the same degree, and ζ decreases.

As mentioned, representing the secondary electron coefficient as a step function equal to unity for $E \geq E_1$ has no effect on the distribution function as long as the majority of resonant electrons have energies above E_1. This can be seen by running simulation cases for the same rf frequency, voltage, and geometry, and only changing E_1. Fig. 4-4 shows no change in the distribution function when changing E_1 from 50 eV to 150 eV, illustrating the independence of the energy distribution function from the secondary yield. The impacting energy distribution is only dependent on the multipactor resonant conditions and the initial conditions (initial energy and time). As mentioned by Vaughan, the secondary yield mainly affects the growth rate of the multipactor, which is outside the focus of this work [2].

While the energy distribution function remains constant, changing E_1 does change the degree of the multipactor resonance, seen in the change in ζ. For lower E_1, more electrons can continue on to the next cycle, while the opposite is true as E_1 approaches

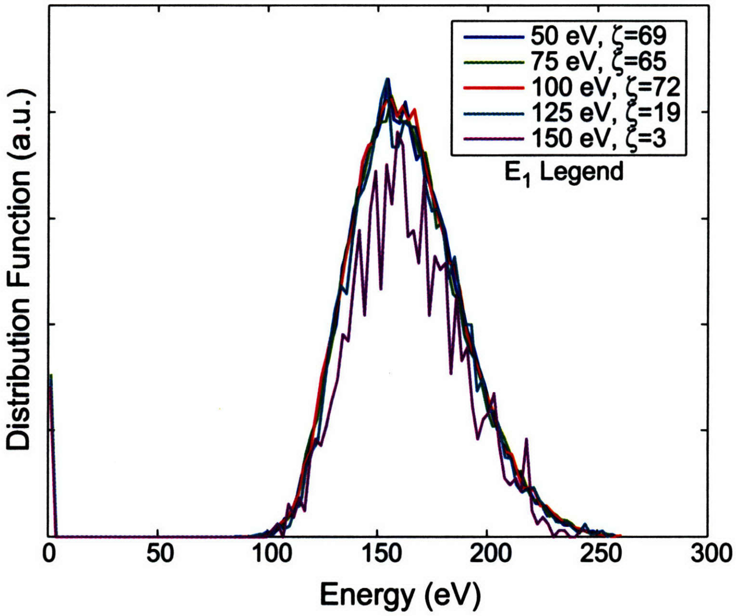

Figure 4-4: Parallel plate impact energy distribution functions for 70 MHz, 250 V, and 3 cm spacing. The shape of the impacting electron energy distribution has no dependence on the secondary electron coefficient.

the energy of the resonant group of electrons near 200 eV.

4.3.1 Parallel plate multipactor results

In the following discussion of typical parallel plate simulation results, conditions of 60 MHz, 160 V, and 2.5 cm electrode spacing will be considered. The two parallel electrodes will be referred to as plate 1 and plate 2, located at x=0 and x=d, respectively where d is the electrode spacing. Initially electrons start at plate 1. For the discussed case, 10,000 particles were started with 80,672 impacts divided approximately evenly between each electrode. E_1 = 125 eV was chosen for a copper with oxide (Cu_2O) surface [36]. There are no changes in the distribution results upon phase iteration, so these results represent a single iteration with all electrons starting at $\alpha = 0$.

Fig. 4-5 shows the emission energy, angle, and velocity distribution functions for all electrons impacting plate 2. It is important to note the absolute value of all initial condition distribution functions are the same for all cases, parallel plate or

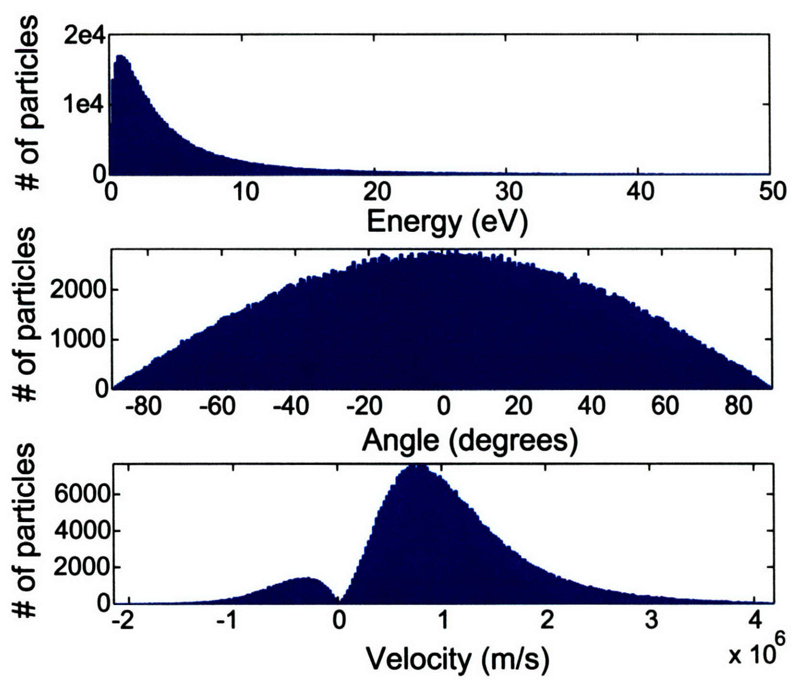

Figure 4-5: Emission energy, angle, and velocity distribution functions for parallel plate geometry, 60 MHz, 160V.

coaxial. The energy distribution reflects the expected distribution given by Eqn. 2.14, and the angular distribution reflects the expected cosine distribution. The velocity distribution has two separate distributions seen in Fig. 4-5. Each distribution is identical, except for a difference in sign and magnitude. This distribution consists of electrons born at plate 1 and plate 2. Particles born from plate 2 have a negative velocity as they are moving in the negative x direction. The opposite is true for electrons originating from plate 1. Seen in the figure, more electrons originating from plate 1 impact plate 2. The difference in magnitude between the two electrons groups will be discussed shortly with Fig. 4-7. These two electron groups are reversed when analyzing the opposite electrode.

Fig. 4-6 illustrates the impact energy, phase, and time distributions for plate 1 at 60 MHz and 160 V, with a electrode gap equal to 2.5 cm. Because of the symmetry of the parallel plate distribution, impact energy distributions are the same for either plate. In the first panel of Fig. 4-6, there is a low energy population near 0 eV, and a higher energy population centered near 120 eV. The electron energy of this higher energy population drops to zero at the rf voltage, equal to 160 V in this case. In the second panel, the distribution of relative phase has a maximum near $\alpha = 2.8$, indicating most electrons impact right before the rf changes sign at $\alpha = \pi$. In the third panel, the distribution of impact time illustrates that the electrons continue to hit with sufficient energy for over 30 rf cycles. The distribution decreases symmetrically and exponentially with each rf cycle as electrons impacting with $E<E_1$ are lost. In reality, the multipactor requires sufficient electron multiplication to overcome this exponential electron loss, but this simple picture is adequate for generating the appropriate distribution functions.

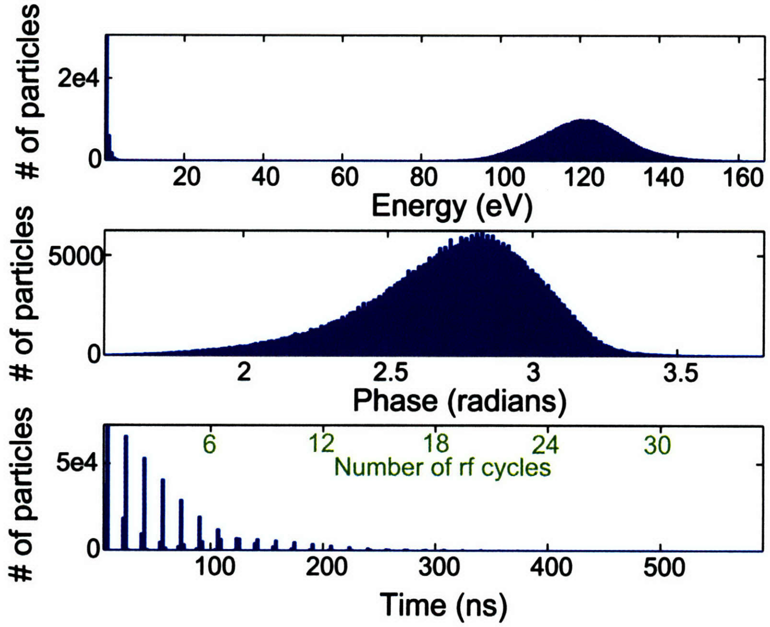

Figure 4-6: Impact energy, phase, and time distributions for parallel plate multipactor at 60 MHz, 160 V, and an electrode spacing of 2.5 cm.

For each electrode, the impacting distribution functions can be separated by the starting electrode into two groups as described in Fig. 4-7. The first panel of Fig. 4-7 gives the energy distribution functions of electrons originating from both electrodes which impact plate 2. The transit time between electrode impacts can also be determined for the different groups of electrons, as illustrated in the second panel of Fig. 4-7. In this figure, the harmonic fraction distribution, n, is shown for all electrons impacting plate 2. The harmonic fraction is defined as

$$n = \frac{t_{impact} - t_{launch}}{T}, \tag{4.8}$$

where T is the rf period.

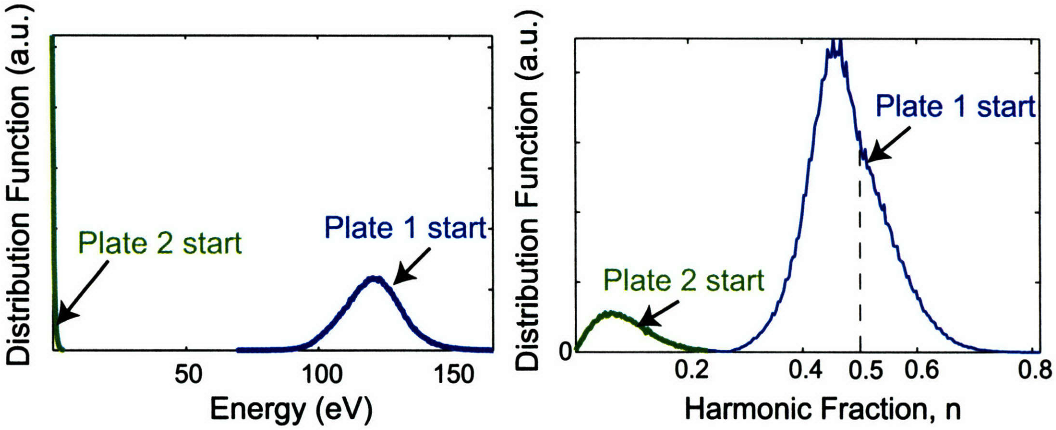

Figure 4-7: Electron distributions impacting plate 1 separated by the starting electrode. The low energy population originates from plate 2 against the rf field and impacts the same electrode after a short period of time. It is the electrons from plate 1 that are responsible for sustaining the multipactor.

Electrons which impact plate 2 originating from the same electrode hit after a very short time with energy less than 3 eV. These electrons are born against the rf field, and represent defocused electrons. The high energy population, centered near 120 eV, is made up entirely of electrons originating from the opposite electrode and impacting near the field reversal, half cycle time of n = 0.5. No higher harmonic trajectories are seen in this case.

Other key results of the simulation are the impact times and phases of the particular electrons which have sufficient energy to cause secondary emission; i.e. $E>E_1$. In order to meet the resonant conditions, the high energy electrons are required to impact near the electric field reversal time, which is indeed the case. Fig. 4-8 depicts a scatter plot of both phase and absolute time plotted against electron energy. Shown next to the scatter plot is a density contour plot illustrating the relative density of the electron energies at a particular phase or time.

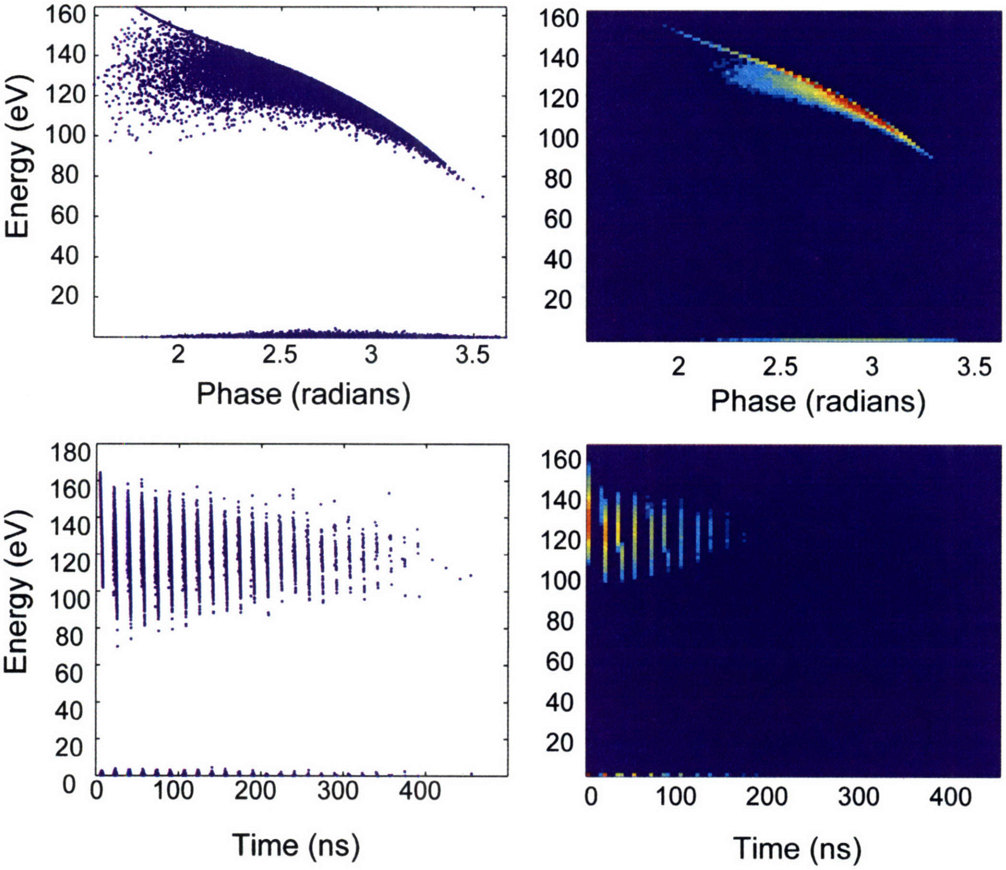

Figure 4-8: Scatter and contour plots of the electron impact energy at each phase and time. Multipactor conditions are the same as Fig. 4-6.

4.3.2 Coaxial multipactor results

This section will describe typical coaxial multipactor simulation results by using the particular case of 70 MHz, 250V, b = 10 cm, a = 4.35 cm, 50 Ω. E_1 was equal to 125 eV. The simulation was run for 150,000 particles, all starting with initial phase = 0. Further phase iterations did not yield any change in the results.

For both conductors, there is a set of electrons which begin and end their trajectory at the same conductor. Electrons starting at either electrode can be accelerated to hit the same or opposite electrode, depending on the initial conditions and electric field. It is possible for outer-starting electrons, having the proper initial energy in the θ direction, to "miss" the center conductor near the time of the field reversal. The electron can then accelerate outward to another section of the outer conductor. By

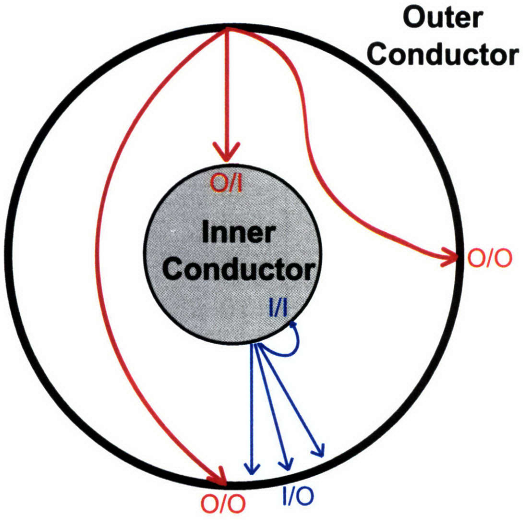

Figure 4-9: Electrons born at the inner conductor can accelerate across and impact the outer conductor (I/O) or turn around to hit the center conductor again (I/I). Electrons born at the outer conductor can have more complicated trajectories with orbital-like motion around the center conductor due to their angular momentum (O/O).

including and conserving the initial angular momentum of the electrons, trajectories like those shown in Fig. 4-9 are accounted for in the simulation. There are four possible trajectories labeled as *Start Electrode/Impact Electrode*: I/I, I/O, O/O, O/I; where I = inner and O = outer.

Fig. 4-10 and 4-11 illustrate the initial condition distributions for electrons reaching each particular electrode, normalized by the number of particles. The green distributions represent all electrons which impact the outer conductor, and the blue distributions represent electrons impacting the inner conductor. As in the parallel plate case, the velocity distribution of Fig. 4-10 gives information on the originating electrode. The electrons with positive initial energy are born at the inner conductor and vice versa for the outer conductor.

It is interesting to note the electrons which originate and impact the same electrode. Seen in the velocity distributions, 14% of electrons which start at the outer conductor return to hit the outer conductor (O/O), while only 3% of electrons which begin at the inner conductor come back to hit the inner conductor (I/I). The relative size of these distributions is due to the higher occurrence of O/O trajectories.

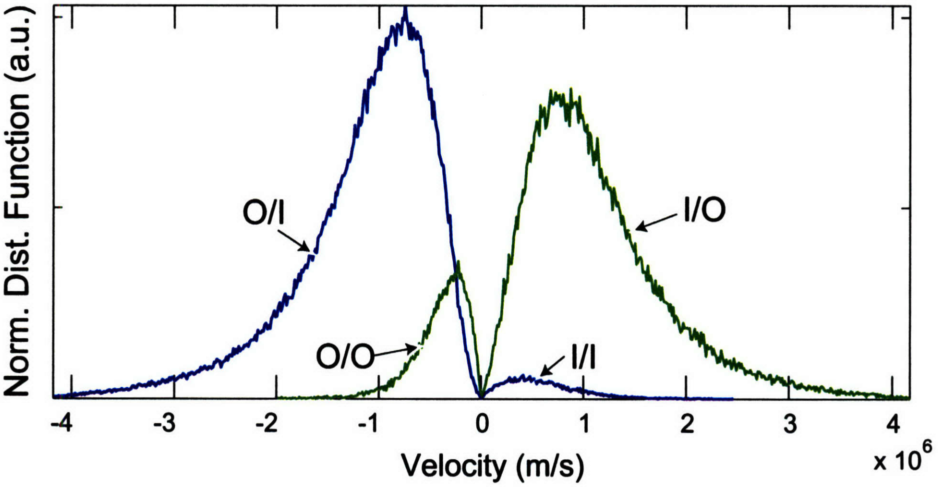

Figure 4-10: Emission velocities for electrons impacting both inner and outer conductors. Electrons with positive initial velocity are born at the inner conductor, while electrons with negative initial velocity are born at the outer conductor. For example, the distribution labeled O/O represents electrons starting and hitting the outer conductor.

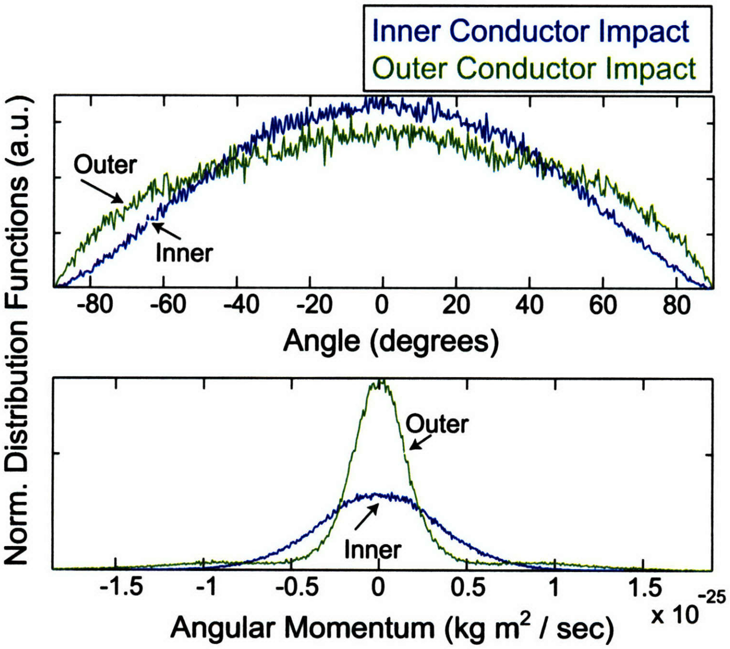

Figure 4-11: Emission angle and angular momentum distributions for all electrons, separated by the particular electrode impacted.

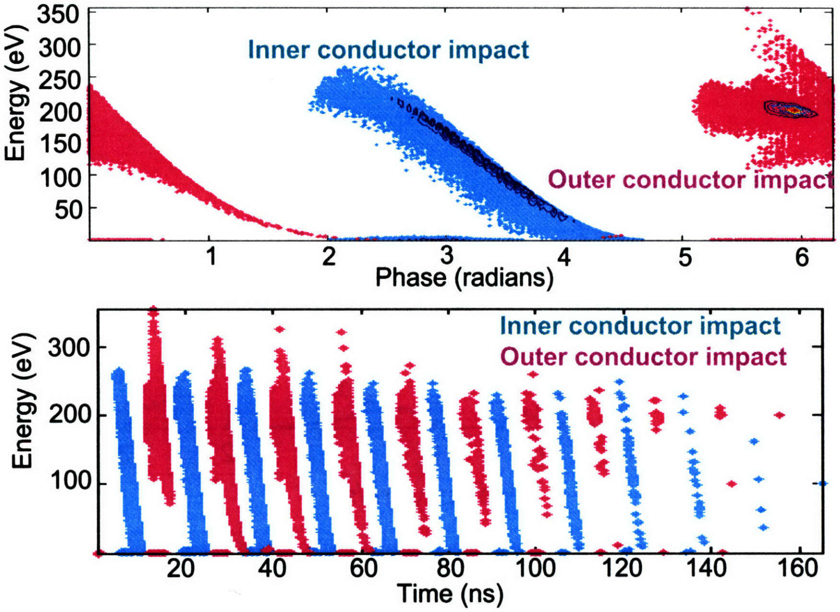

Figure 4-12: Scatter plots of the phase and time of impact for each electron energy. A contour plot is overplotted in the phase plot to illustrate the relative number of particles.

The emission angle and angular momentum distributions are shown in Fig. 4-11. The differences in these distributions for inner versus outer starting electrons are due to the trajectories described in 4-9. The angle distributions illustrate more electrons with a high emission angle impact the outer conductor due to the "center missing" trajectories (O/O). From the distributions of angular momentum, the bulk of the population impacts the outer conductor with near zero angular momentum, while the inner conductor is impacted with a less peaked angular momentum distribution. It will be shown shortly that the more peaked L distribution near L=0 for the outer conductor is due to the narrow, high energy ($E>E_1$) beam of electrons which are accelerated outward from the center conductor (I/O).

As in the parallel plate case, the electrons "bounce" between the electrodes and impact near the field reversal times at phases of 0 and π, shown in Fig. 4-12. The first panel has a contour plot overplotted to show the relative density of particles at a particular energy and phase. The highest concentration of particles impact the outer conductor at a relative phase near 6 with an energy of 200eV.

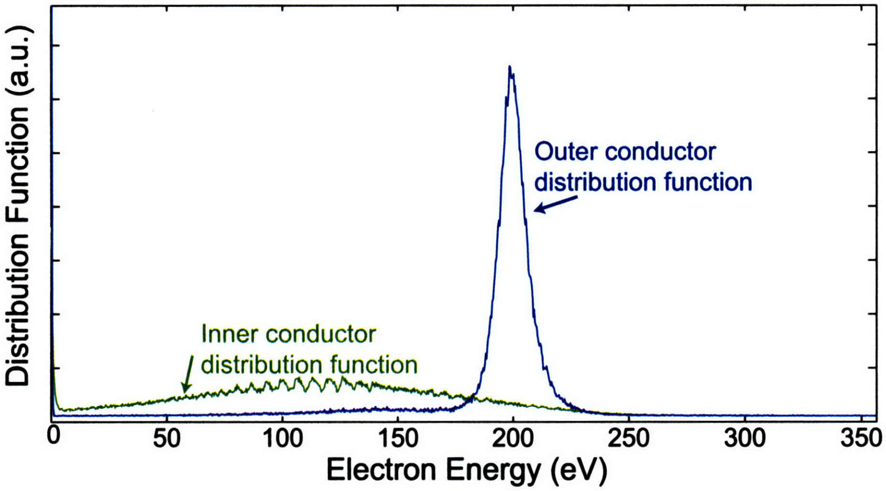

Figure 4-13: Impact energy distribution functions for both the inner (green) and outer (blue) conductors.

Fig. 4-13 shows the electron impact energy distribution functions for each electrode. The outer conductor distribution has a large population of electrons centered at 200eV representing the multipactoring electrons and another population at 0 eV representing defocused electrons. The high energy distribution falls to zero near 350 eV, but this is difficult to see from the figure due to the number of particles and the relative height of the 200 ev peak to the tail. The tail can be seen more clearly on the log axis in Fig. 4-14. In contrast to the outer conductor distribution, the inner conductor distribution is much more broad and tails to zero at 250 V. The saw tooth structure near 100 eV is due to the finite time steps of the coaxial simulation.

Fig. 4-14 separates the distribution functions by the originating electrode. For instance, the first panel shows all electrons impacting the inner conductor, but the electrons are separated by the conductor of origin (I/I, O/I). Nearly all electrons which impact the inner conductor originate from the outer conductor (O/I). Only a small, defocused, low energy fraction start at the inner conductor and hit the inner conductor (I/I). Also seen in Fig. 4-14, there is a significant fraction of the electrons impacting the center conductor with E<125 eV, and all these electrons terminate upon this low energy impact.

The distribution functions for outer conductor impacts are shown in the second

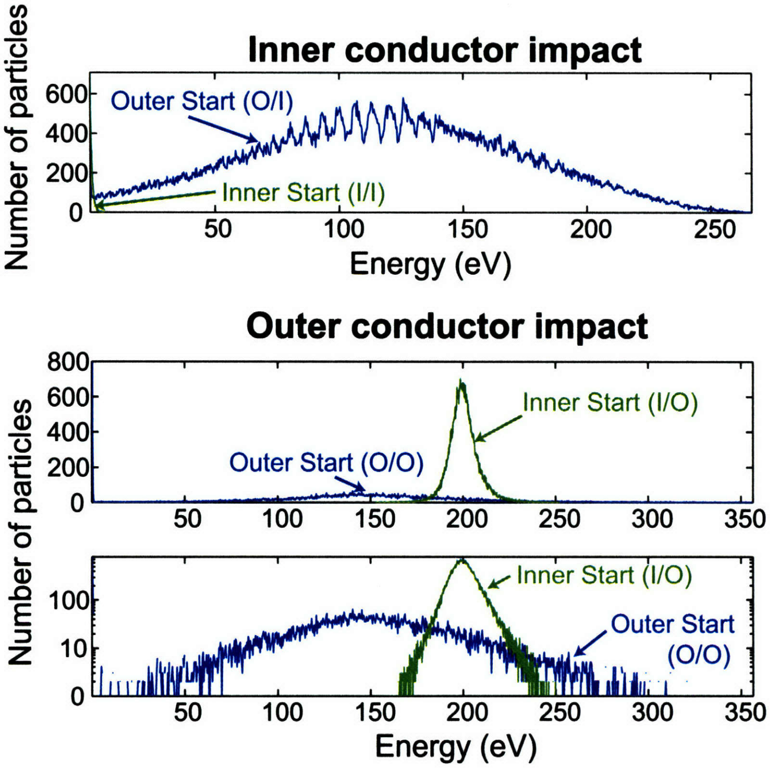

Figure 4-14: Electron energy distribution functions for both inner and outer conductors. The distributions are separated by the starting electrode. The outer-impacting distributions are also displayed on a logarithmic y-axis in order to see the high energy tail to over 300 eV.

and third panel, represented as both a linear and semi-log plot. All electrons born from the inner conductor impact the outer conductor as a fairly narrow beam centered at 200 eV and going to zero at 250 V. There is also a significant fraction of electrons which begin and impact the outer conductor (O/O). The O/O distribution is much broader and also includes a large number (4,653) of defocused electrons at 0 eV. The large peak at 0 eV has been cut off in order to focus on the higher energy distribution. It should be noted that this outer-originating distribution has a large number of multipactor-capable electrons above 125 eV and is also responsible for the high energy tail which extends to over 300 eV. This result suggests the outer conductor is capable of sustaining a multipactor discharge without secondary emission from the inner conductor.

The number of electrons decreases exponentially with the number of rf cycles as

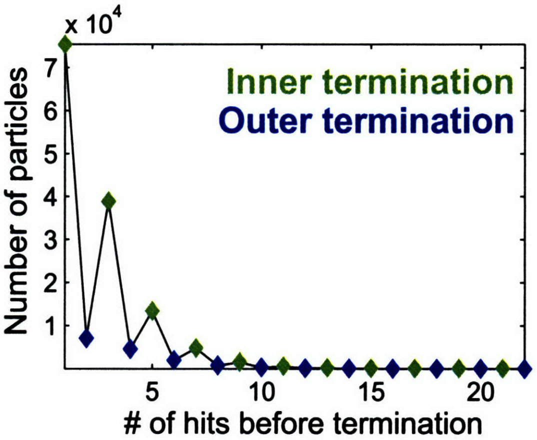

Figure 4-15: The number of particles decays unsymmetrically for the coaxial case. More particles terminate upon hitting the inner conductor because of the lower energy distribution.

in the parallel plate case, except the decay is not symmetric in the coaxial case. More electrons terminate upon impacting the center conductor because of the large fraction of the O/I energy distribution with $E<E_1$. In addition, the I/O electrons with $E>125$ eV also contribute to the non-symmetric decay shown in Fig. 4-15 and the high density region in Fig. 4-12. Because these electrons have $E>E_1$, all continue to the next cycle, and therefore fewer particles terminate on the outer conductor.

Fig. 4-16 illustrates scatter plots of impact energy with angular momentum for each electrode. Both plots are symmetric about zero because of the symmetric angular distribution initial condition. Looking first at the electrons impacting the center conductor, electrons originating from the outer conductor impact with a wide range of angular momentum with energies up to 250 eV. The few electrons originating at the center conductor and impacting the center conductor impact with very low energy, and the angular momentum spread is 43% less than the previous case (O/I). This difference in angular momentum is due to the difference in radius between the outer (1.97 cm) and the inner (0.86 cm) conductors, and the L dependence on this radius (see Eqn. 4.7).

More interesting are the electrons which impact the outer conductor, shown in the second panel of Fig. 4-16. All electrons which originate from the inner conductor impact the outer conductor with energy above 150 eV and maximum energy near 250

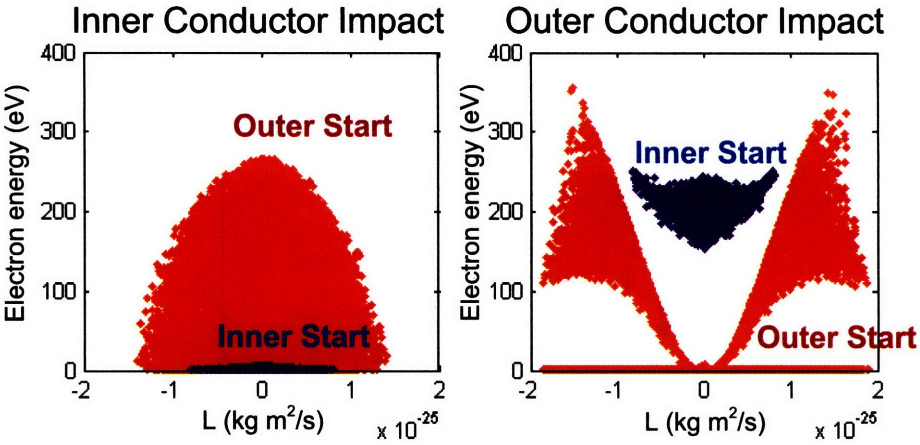

Figure 4-16: Scatter plot of impact energy and angular momentum for electrons impacting each conductor. Electrons originating at the outer conductor are shown in red, while electrons starting at the inner conductor are shown in blue.

eV. The angular momentum range is ± 0.8 x10^{-25} kg m^2/s. Alternately, the outer-originating electrons impact with a much different pattern. The angular momentum range is 43% larger than inner-originating electrons due to the conductor dimensions, yet there are no electrons with zero angular momentum for energies over 5 eV. Instead, the electrons have a narrow energy band for a given angular momentum, determined by the aspect ratio of the coaxial line. The physical interpretation of the shape shown in red on the second panel of Fig. 4-16 is a consequence of the rf phase and electron angular momentum. These are the electrons which have trajectories that "miss" the center conductor as described by Fig. 4-9. If an electron is born with no θ velocity, it will either impact the center conductor with the distribution shown in red in the first panel of Fig. 4-16 or impact the outer conductor with near zero energy as a defocused electron. Which case depends on the relative phase when the electron is born. The initial phase, v_θ, and angle determine the orbital-like motion around the center conductor. It is also important to again notice that the outer-originating electrons with angular momentum near ± 1.4x10^{-25} are responsible for the high energy tail of electrons impacting the outer conductor.

For the case described here, there are no electrons which have harmonic fractions over 1, which indicates no multiple harmonic trajectories. For the inner conductor

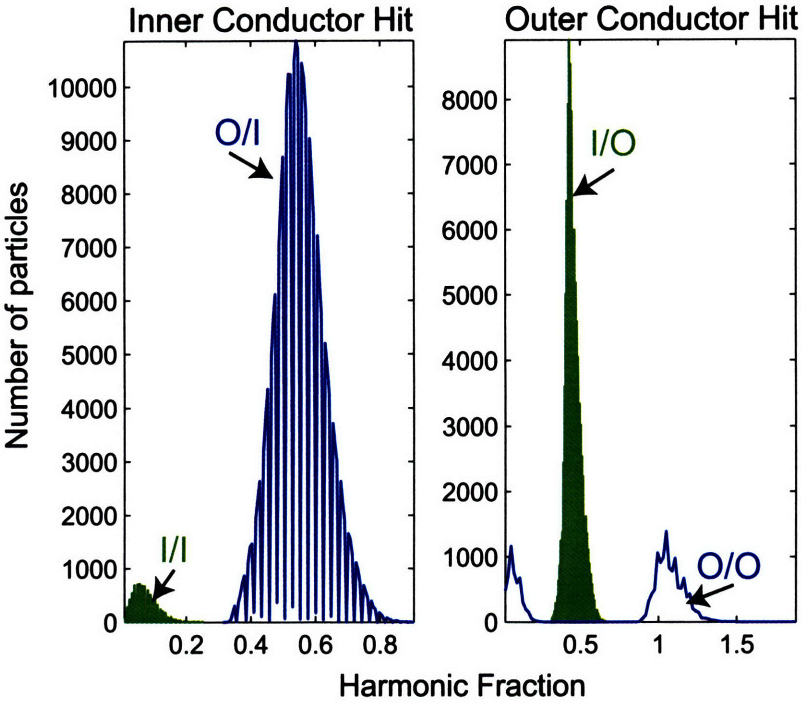

Figure 4-17: Distribution functions of the harmonic fraction, n. Both outer and inner conductor impacts are shown, and the distributions are separated by the starting conductor. The saw-tooth structure in the distributions are due to the finite time steps in the simulation.

impacts, the resonant electrons labeled O/I impact the inner electrode right after the rf field reversal with the maximum located at $n = 0.56$. The defocused, low energy electrons labeled I/I are shown impacting very early, as these electrons are being launched against the rf field and immediately impact the same conductor with low energy.

The electrons impacting the outer conductor from the inner conductor, I/O, all impact in a very narrow time band right at the field reversal, $n = 0.5$. The O/O electrons are divided into two groups: a low energy, defocused group which impact very soon after being launched, and a high energy group which impact the outer conductor after 2 field reversals or a single rf cycle. These are the electrons mentioned previously that miss the inner conductor and are accelerated to the opposite side of the outer conductor.

Chapter 5

Analysis

The focus of this chapter is to provide an understanding of the experimental electron energy distributions by using computational results from the Monte Carlo simulations developed in the previous chapter. The goal is provide the physical mechanisms and underlying physics responsible for the shape of the distribution function. It will be shown in both coaxial and parallel plate cases, the high energy population responsible for the multipactor is a result of the resonance condition of the multipactor, and this can be explained by the simple single particle simulation. Yet, for the more subtle features of the distribution functions, such as the low energy populations and the width of the high energy population, an explanation is provided by including space charge effects and interaction with the rf voltage. Also, the effect of impurities and oxides on electrode surfaces will be discussed.

Upon determining the physics behind the different distribution functions, a comparison of coaxial and parallel plate simulation data show that coaxial geometries are more susceptible to multipactor, and this is also seen experimentally. Lastly, scaling laws and "rule of thumb" engineering equations for the multipactor susceptibility will be given.

5.1 Coaxial Multipactor Analysis

5.1.1 Comparison between simulation and experimental results

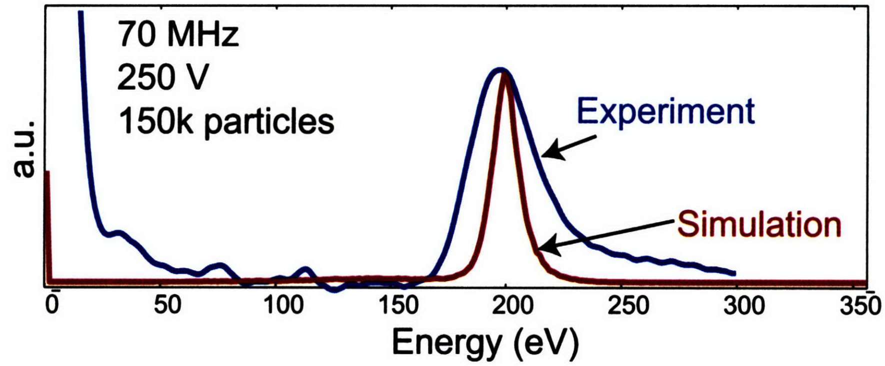

Figure 5-1: Comparison of coaxial multipactor distribution functions of electrons impacting the outer conductor with f = 70 MHz and V_{rf} = 250 V.

For any given CMX experimental parameters, the same parameters can be implemented in the MC simulation previously discussed. By comparing the distributions of the experiment to those of the simulation, the physics behind the features of the electron distributions can be determined. Initially, the experimental distributions will be compared to simulation data with no space charge effects, energy and phase spreading, or other collective effects. This simulation will be referred to as the single particle approach because of the non-inclusion of collective effects. For this initial comparison, the experimental distribution for coaxial multipactor at 70 MHz, 250 V, and electrode spacing of 2.82 cm will be compared to the simulation discussed in Chap. 4 using the same parameters as the CMX experiment. The aperture depth of 1.7 mm is neglected in the coaxial simulation.

Fig. 5-1 depicts both experimental and simulation distribution functions for electrons impacting the outer conductor. The most significant similarity of the distribution functions is the energetic location of the high energy population. In both cases, the peak is near 200 eV and 80% of V_{rf}. As discussed in Chap. 4 and Fig. 4-14, nearly all of this population consists of electrons originating from the inner conductor and impacting the outer conductor (I/O). The location of this population is purely a result of the phase and velocity distributions developed from the corresponding geometries and electric fields. In other words, this population consists of the electrons which meet the multipactor resonance condition for the given geometry, frequency, and voltage. Another similarity is the presence of an energetic tail extending to near 350 eV. This tail is difficult to see in Fig. 5-1 because of the relative height as compared to the high energy population, yet the red curve representing the simulation data ends when no more electrons are measured at 350 V. As discussed in the preceding chapter, this tail is a result of the angular momentum of electrons born at the outer conductor, which allows certain electrons to miss the center conductor and hit the opposite side of the outer conductor (O/O).

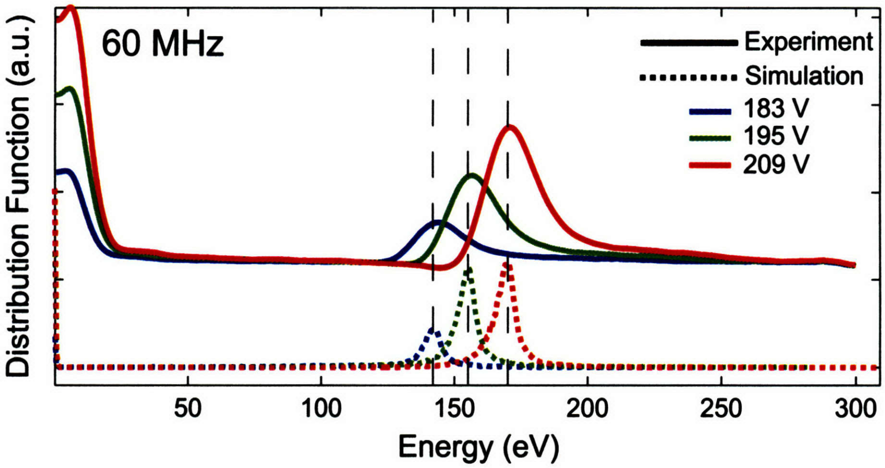

Figure 5-2: Comparison of experimental and simulated coaxial multipactor at 60 MHz, 50 Ω, 10 cm outer electrode diameter, and 3 different voltages; 183V, 195V, and 209V.

The same similarities can be seen at the other frequencies as shown in Fig. 5-2 and 5-3. For 60 MHz, three experimental cases are simulated with the same conditions and rf voltage. The simulation distributions are all normalized by the same constant so that the distributions retain their relative size information. Fig. 5-2 illustrates the multipactor current becomes larger with increasing rf voltage. This is due to the higher degree of electron resonance; i.e. more electrons having sufficient energy for secondary electron emission at these higher rf voltages. The simplified simulation using a step function δ, with E_1=125 eV, is sufficient to explain this current rise with rf voltage.

For 80 MHz, the experimental distributions have the same general shape as the distributions for 60 and 70 MHz, with the multipactor population at slightly higher energy. At 80 MHz, and an rf voltage near 270 V, a new population of electrons is seen experimentally near 50-75 eV, as shown in Fig. 3-16. Fig. 5-3 compares the experimental and simulation cases for the rf voltages of 270 V and 305 V. These two voltages were chosen because the 50-75 eV population, present at 270 V, disappears at V_{rf} = 305 V. This same feature is also seen in the simulation data of Fig. 5-3.

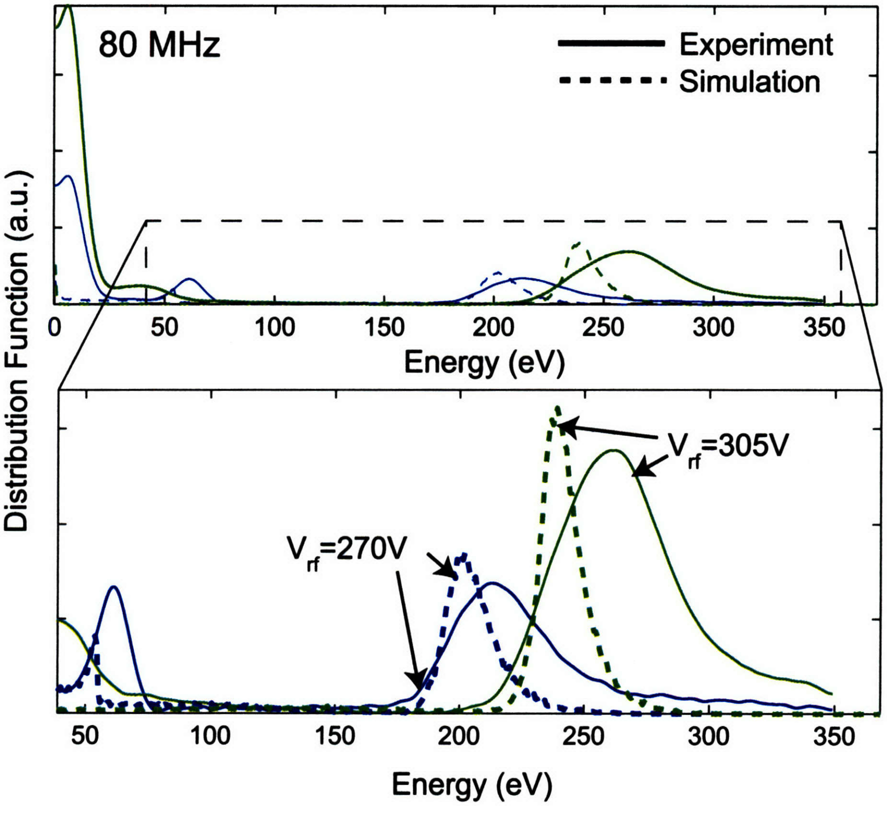

Figure 5-3: Comparison of experimental and simulation coaxial multipactor at 80 MHz, 50 Ω, d_{outer} = 5cm, and rf voltages, V_{rf} = 270 V and 305 V.

Comparing the simulation and experimental data for 80 MHz, the peaks of the high energy populations from the simulation are at slightly lower energy than the experimental peak. While the peaks are slightly different, the low energy sides of distributions agree very well. Interestingly, this can also be seen in the 50-75 eV population. The data match very closely on the low energy side of the population. From these data, it appears there is some unknown effect likely causing an upward spread in energy of the electron distributions. Also, as in the 60 MHz case, the relative increase of the current with rf voltage can also been seen in the simulation at 80 MHz.

Returning to the discussion of the 50 eV population, simulation results show these electrons are born from the outer conductor with low angular momentum, and, for the proper initial conditions, they reverse in direction before they can impact the inner conductor. Having insufficient initial energy or inappropriate starting phase to reach the opposite conductor, these electrons return to the outer conductor with impact energies near 55 eV. This can be seen in Fig. 5-4.

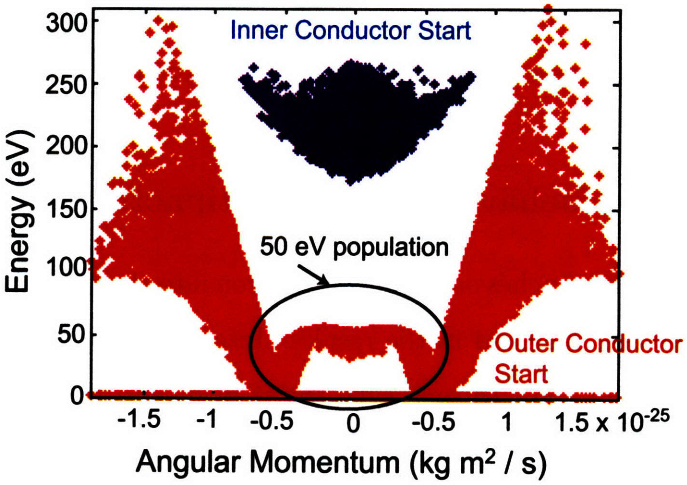

Figure 5-4: Scatter plot for electron energy and angular momentum for outer conductor impacts. The 50 eV population can be seen at low angular momentum, originating from the outer conductor.

The single particle simulation provides energy distribution functions of the electrons which are purely dependent on the specific geometry, frequency, and voltage for a given distribution of initial conditions; i.e. emission velocity and angle. Observing the distribution similarities between this simulation and experiment, it can be concluded that the energy distribution of the high energy electrons responsible for sustaining the multipactor is a result of the resonance condition for the specific multipactor conditions. In other words, the frequency, geometry, and rf voltage are just right to provide resonant electron distributions of the shape shown above. With that said, the remainder of this chapter will deal with explaining the differences in the experimental and simulation results. The main differences in the results are the difference in width (relative height) of the high energy population, the difference in the relative height of the high energy tail, and the absence of a large low energy population in the simulation.

In determining the cause for these differences, several mechanisms such as electron-electron and electron-neutral collisions can be ruled out completely. With electron densities near 10^{11} m^{-3} and neutral gas densities below 10^{18} m^{-3}, the electron mean free paths are much larger than the system size for clean electrodes [58]; therefore collisions could not influence the distribution functions. The following section will suggest several possible mechanisms, not included in the single particle simulation, which could explain the described differences in the distribution functions.

5.1.2 Collective behavior of the multipactor discharge

Because the simulation launches only a single electron into the vacuum rf electric field, no collective effects are included in the results. Interaction between multipactoring electrons, interaction of the electrons with the rf field, and interactions within the RPA are not included in the simulation, and it is these effects that will be shown to cause the differences between the experimental and simulation distributions.

Electron space charge effects

Because the electrons accelerate across the gap as a phase-focused, narrow group as described in Chap. 2, the self-field of the electron sheet can cause it to widen [2, 51]. There is some finite width to the width of the sheet due to the distribution of emission energies, and that width can be seen in the single particle simulation results. By multiplying the phase spread by a uniform bulk velocity and the rf angular frequency, ω, an approximate sheet width can be calculated. Neglecting space charge, the approximate width due to the emission energy variation is on the order of a few mm for 70 MHz and 250 V, as shown in Fig. 5-5.

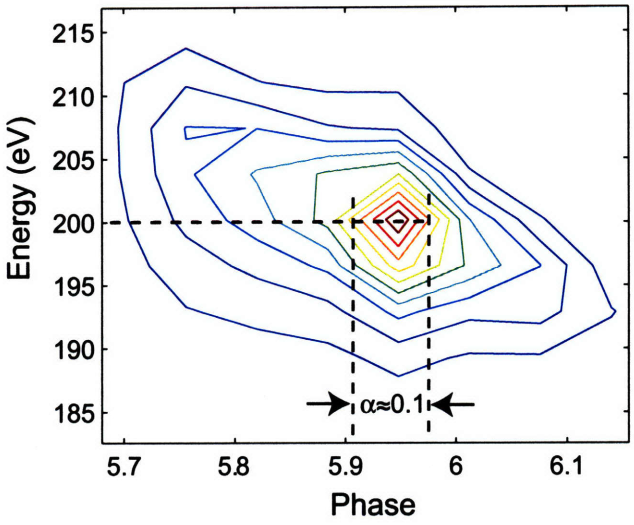

Figure 5-5: Contour plot of relative density of electrons with phase and energy. By assuming the majority of electrons have a phase range near 0.1 and E = 200 eV, the approximate electron sheet width is 1-2 mm.

The space charge of the current sheet can cause electrons to be accelerated ahead and behind the main group. In turn, this effect can cause further spreading of the phase distribution that affects the energy distribution function. In order to determine the plausibility and extent of this effect on the distribution functions, an infinitely thin sheet of charge will be initially assumed for simplicity. The electric field due to an infinitely thin current sheet is $E = \frac{\sigma}{2\epsilon_o}$, where σ is the surface charge density. A surface charge of order 2x10^{-8} C/m^2 will also be used for this case. This σ corresponds to a typical CMX current density of 1 A/m^2 collected in one half cycle at 70 MHz. For this case, the current sheet has an electric field of 1 kV/m, as compared to E_{rf} near 10kV/m. For V = 250 V in the coaxial geometry described above, the electric field due to space charge, E_{sc}, ranges from 7 to 17% of E_{rf}; therefore this space charge effect is not negligible.

In order to approximate this space charge effect on the distribution function, a similar approach to Vaughan will be taken [2]. In this approach, a test electron in the frame of the moving current sheet will be accelerated due to the space charge electric field. The acceleration felt by the electron will be

$$a = \frac{e\sigma}{2m_e\epsilon_o}. \tag{5.1}$$

Assuming a half cycle transit time, this acceleration gives rise to a relative change in velocity of

$$\Delta v = \pm\frac{e\sigma}{2m_e\epsilon_o}\frac{\pi}{\omega}. \tag{5.2}$$

The distance the electron advances forward or backward can also be determined by another integration and is given by

$$x = \pm\frac{e\sigma}{2m_e\epsilon_o}\frac{\pi^2}{2\omega^2}. \tag{5.3}$$

For the test case considered, Δv = 1.5x10^6 m/s or ΔE = 6.4 eV is possible. Also, a corresponding displacement of x = 5.6 mm is possible. The displacement can be converted to a phase delay or advance by multiplying by the sheet velocity. Using 80% of the V_{rf} or 200 eV (See Fig. 5-1) for the test case, the change in phase is equal to $\Delta\alpha = \pm 0.3$, which, for a half cycle, yields a phase spreading near 20%.

This phase spreading can be included in the simulation by adding random statistical variation with a standard deviation of 20% to each impact phase. If the electron impacts with E>E_1, then the secondary emitted electron is launched at the new phase which includes the randomly added error. The 20% phase spreading can be seen in Fig. 5-6, which shows the spread distribution of phases for 70 MHz in the same geometry as above.

This simple correction is used to determine whether space charge could spread the high energy populations to the degree seen in the experimental results. Fig. 5-7 depicts two sets of distributions. In the first panel, simulation energy distribution functions for no phase variation and 20% phase variation are compared. As mentioned, there are very few electrons between 1 eV and 100 eV for the single particle

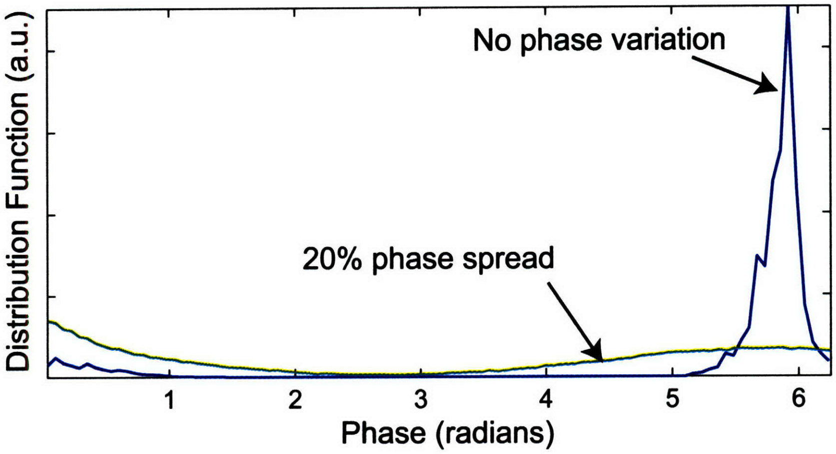

Figure 5-6: Phase distributions for coaxial multipactor at 70 MHz and the previously discussed geometry. Both the single particle, and 20% phase spread distributions are shown.

case. Yet, after implementing 20% phase spread, an electron population can be seen from 1 to 50 eV. Comparing this distribution to the experimental case in the second panel, these low energy populations agree rather well, suggesting these low energy electrons are in fact due to space charge spreading of the electron sheet. The simulated space charge effect also reduces the relative peak height of the high energy population near 200 eV, but it is still more peaked than the experimental case. In the same fashion as Fig. 5-5, the size of the electron sheet with 20% phase spreading can be determined to be approximately 7-8 mm, filling almost a third of gap, which is in agreement with Vaughan's theoretical treatment [2].

In considering space charge effects, the simulation results also show the low energy electrons are all O/O trajectories, which are either are defocused (<5 eV) or have multiple harmonic trajectories with low angular momentum. While electrons with high angular momentum can accelerate around the center conductor to energies over the rf voltage, these electrons are emitted with nearly all radial velocity and have insufficient energy to hit the opposite conductor. They then end up returning to the outer conductor upon the rf field reversal with energies 1-50 eV. Fig. 5-8 shows selected trajectories for electrons born with velocity -10^6 m/s and zero angular momentum for starting phases between 0 and 2. Electrons starting near $\alpha = 0$ accel-

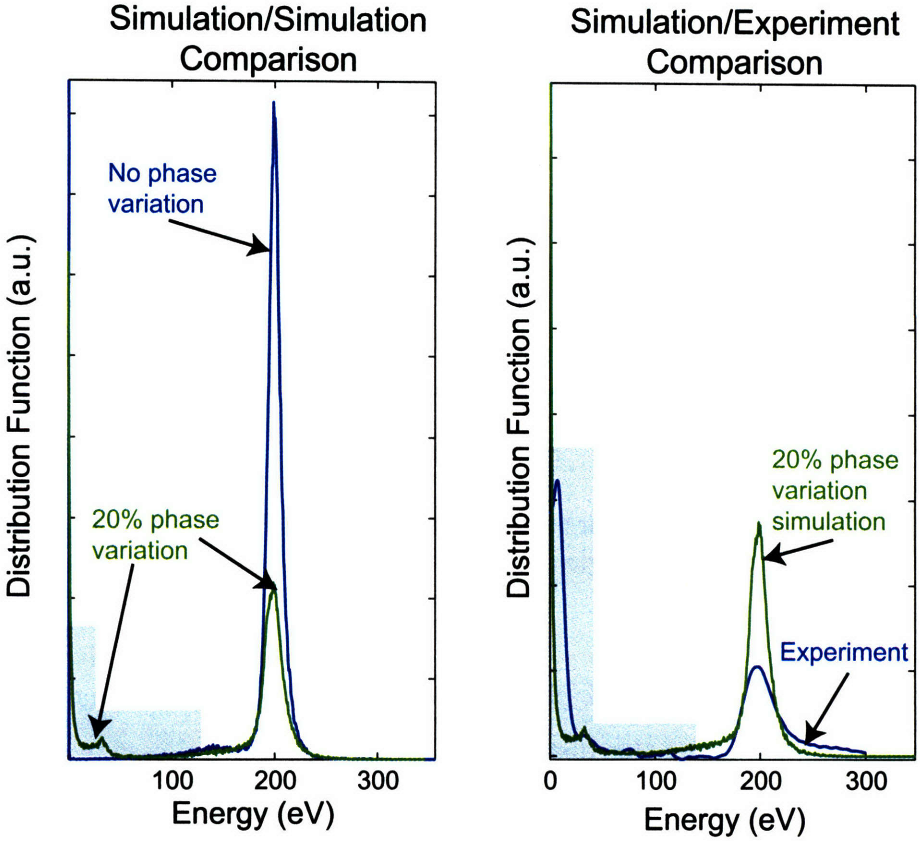

Figure 5-7: Energy distribution functions for electrons impacting the outer conductor for 70 MHz. The first panel depicts simulation distributions for the cases of zero and 20% phase spreading. For 20% spreading, there is a low energy population of electrons, very near that seen in the experimental results, shown in the second panel.

erate to the inner conductor, while electrons starting with phases from 0.75 to 2 turn around to come back to the outer conductor. Specifically, electrons with $\alpha = 0.75$ have higher order harmonic motion back to the outer conductor. For this trajectory, the electron impacts with E=30.8 eV, yet electrons with $1.0 < \alpha < 1.25$ return near 1 full rf cycle and impact with energies from 20-30 eV. The impact energy of both n=1 and 2 harmonic trajectories can extend up to near 50 eV with increasing emission velocity.

It can be concluded that many of the low energy electrons are a result of phase spreading due to space charge effects. The space charge effects cause a higher percentage of particles to have the appropriate phase for the aforementioned trajectories,

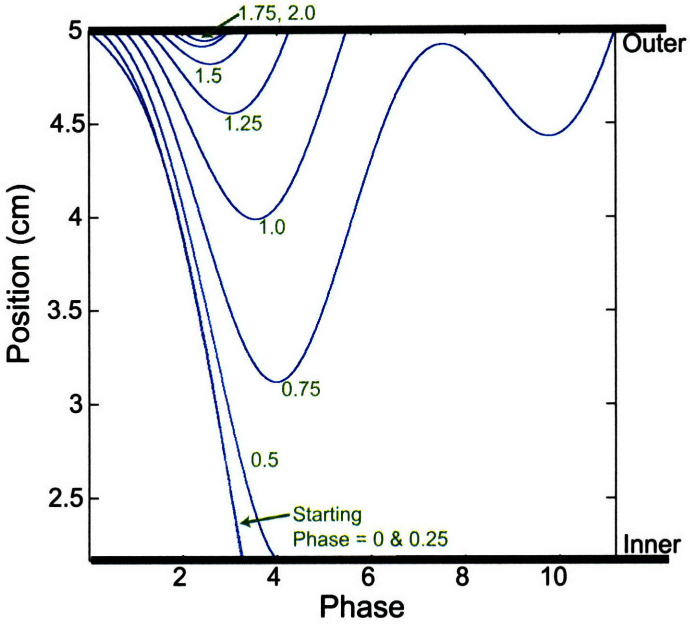

Figure 5-8: Nine different 1-D electron trajectories with zero angular momentum, 10^6 m/s emission velocity (3 eV), and starting phases from 0 to 2. The impact energies for the trajectories, starting with $\alpha = 0$, are 133, 98, 4.4, 30.8, 31.3, 24.7, 10.7, 5.1, 3.4 eV.

and it is these trajectories which give rise to impact energies in this low energy range. For 80 MHz, a similar argument can be made to explain the population peaking near 50 eV. Because of the higher frequency, this peak exists without accounting for space charge effects with similar trajectories as described by Fig. 5-8. Yet, space charge effects yield more electrons in the phase range to contribute to this low energy population.

Returning to the discussion of the high energy section of the distribution function, the high energy population is almost entirely made up of I/O trajectories, but as mentioned, O/O trajectories are responsible for the high energy tail. These results suggest a very important result. They suggest that while the bulk of multipactoring electrons involve inner conductor impacts, O/O trajectories have sufficient energy to support multipactor on the outer conductor alone. In this case, multipactor avoidance techniques would need to be applied to both coaxial electrodes to completely prevent multipactor.

Experimental evidence of space charge effects

If the number of low energy electrons is a result of space charge, then experimentally, the size of the low energy population (E<50 eV) should increase with increasing current density or surface charge as the space charge increases. The low energy current fraction, f_{lowE}, can be determined by integrating the distribution function from 0 to 50 eV and dividing by the total current, or $f_{lowE} = \int_0^{50} f(E)dE/I$. The electron sheet surface charge, σ, can be estimated from the current density as before. Fig. 5-9 shows the fraction of the low energy population to the total collected current with the estimated surface charge for 15 different frequencies from 55 to 90 MHz. For surface charge below 10^{-8} C/m^2, the number of low energy electrons decreases with increasing current, yet at and above 10^{-8} C/m^2, the low energy fraction increases with current as expected for space charge effects.

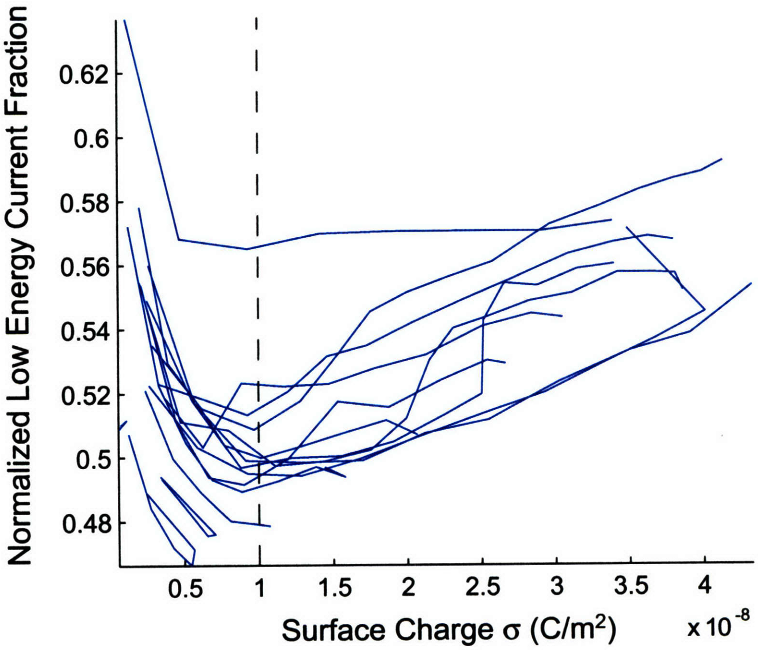

Figure 5-9: Low energy current fraction normalized by the total current versus the surface charge of the electron sheet. 15 coaxial multipactor cases are shown here for frequencies 55 - 90 MHz. There is a clear increase in the number of low energy electrons above σ=10^{-8} C/m^2.

At low surface charge below 10^{-8} C/m^2, the low energy fraction decreases with current for two possible reasons. The first is at low current, secondary emitted electrons from the RPA entrance grid could dominate the electron distribution until the enough high energy electrons are developed in the multipactor (see Sec. 5.1.3). The second possible cause is the error in the measurement at low current is relatively high. Yet, above 10^{-8} C/m^2, there is a definite rise in the low energy electrons which is near the same surface charge estimated in the preceding calculations justifying space charge effects.

Fig. 5-10 illustrates simulation distribution functions for increasing space charge effects in the form of increasing values of the phase spread standard deviation. It can be seen in the figure that the low energy electron population from 5-50 eV only appears for phase spread of 20% and greater. Also, while the high energy population peak holds at the same energy for all phase spread values, there is only a small decrease in the relative height of the high energy population past 20% phase spread. In addition, there is only a small increase in the number of low energy electrons with increasing phase spread beyond 20%. Because the increasing phase spread correlates to a higher space charge and, consequently, a higher multipactor current, these results are supported by the experimental observations shown in Fig. 5-9. Experimentally, the trend in the number of low energy electrons changes sharply near $\sigma = 10^{-8}$ C/m^2 (corresponding to a 20% phase spread), and then increases slowly with increasing current.

This finding demonstrates that the simple charge sheet model for implementing space charge effects is sufficient for explaining this collective phenomena. It also illustrates the importance of the space charge effects in developing the low energy population of the electron distribution function.

Interaction of the multipactor with the rf electric field

As just shown, the self field of the electron sheet can cause it to expand, which in turn causes an increase in the number of low energy electrons. In addition to this phase spreading effect, the electric field of the electron sheet interacts with the rf electric field, causing a depression in the potential across the gap. This depression

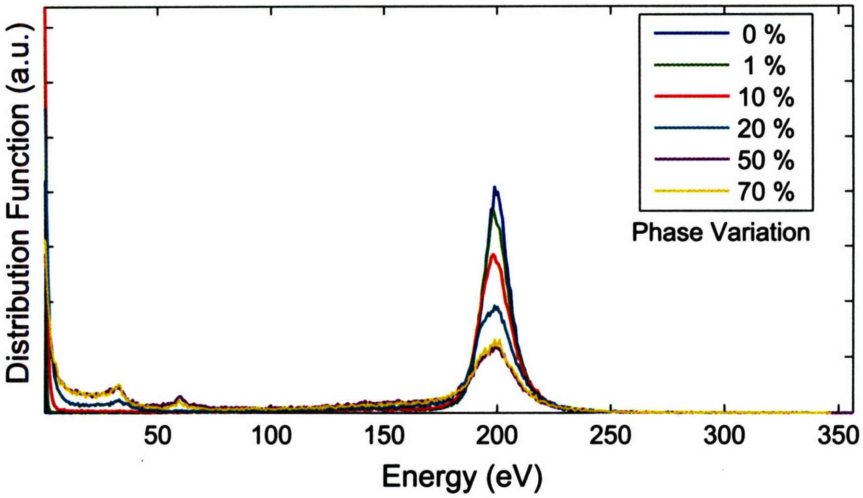

Figure 5-10: Effect of space charge phase spreading in the simulation. At least 20% phase spreading is necessary to see the low energy populations, yet increasing the phase spread over 20% has only a small effect.

can be estimated, as in the case in Sec. 5.1.2, for an electron sheet with $\sigma = 10^{-8}$ C/m^2, located in the center of the electrode gap. The simple potential depression determined from the electron sheet electric field is simply $V_{sc} = \frac{d\sigma}{2\epsilon_o}$. where d is the electrode spacing. Fig. 5-11 illustrates the effect of the electron sheet potential depression in the $\frac{1}{r}$ field of the coaxial geometry for 70 MHz, V_{rf}=250 V, and $\sigma = 10^{-8}$ C/m^2. The potential can vary up to 8 V from the rf voltage.

Due to this change in the rf potential and electron inertia, it is possible for the electron energy to spread on the order of this potential depression. Electrons moving from the inner conductor to the outer conductor (see Chap. 4, Sec. 4.3.2) have the narrowest sheet width, and therefore would be the most affected by the space charge potential depression. A simple modification can be made to the simulation to incorporate the electron energy spreading by adding a normal distribution of energy variation with standard deviation equal to the potential depression. A normal distribution was chosen for convenience to approximate the effect of this energy spreading. This spreading is applied to the high energy electrons in the narrow sheet, which are also the electrons responsible for sustaining the multipactor with E>125 eV.

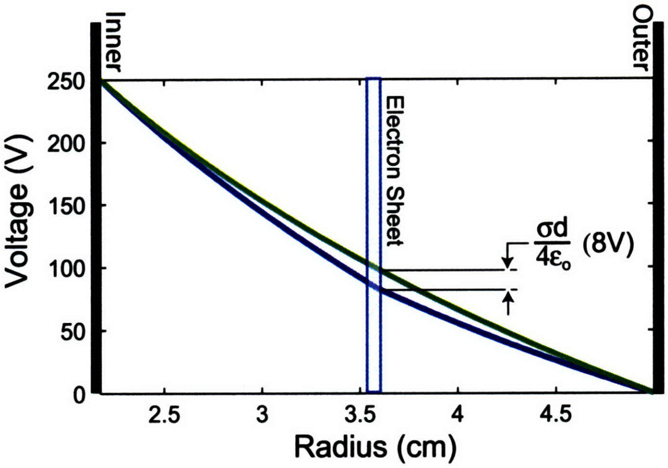

Figure 5-11: The potential depression due to the presence of an infinitely thin electron sheet located in the center of the gap in a coaxial geometry. For 70 MHz, V_{rf}=250 V, a $\sigma = 10^{-8}$ C/m^2 electron sheet causes a 8 V depression.

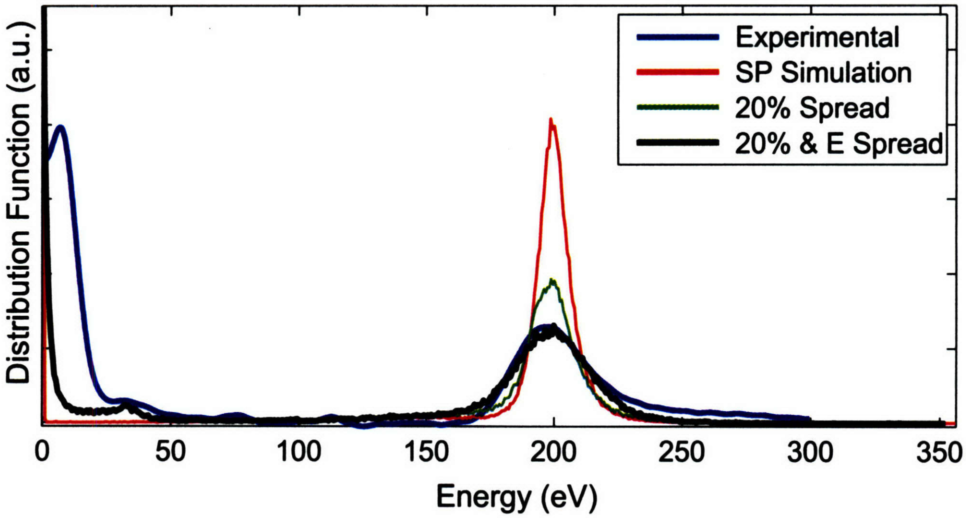

Figure 5-12: Distribution functions for experiment, single particle (SP) simulation, 20% phase spread simulation, and 10 eV energy spread with 20% phase spread simulation. All simulation data is normalized by the number of particles. The case considered is 70 MHz, 250 V, with the same coaxial geometry.

Fig. 5-12 shows the resulting distribution function after applying a 10 V voltage spread to the 20% phase spread simulation at 70 MHz and 250 V (black), as compared to the experimental (blue), single particle (SP) simulation (red), and 20% phase spread simulation (green) distribution functions. The 10 eV energy variation causes a slight spreading of the high energy population, and gives very good agreement with the experimental results. There are three slight differences in these two distribution functions. The first is the larger number of electrons near 5 eV in the experiment, and this is likely due to secondary emission from the bias grid within the RPA. The second two differences are a slightly higher number of simulation electrons at energies just below the high energy population and a slightly larger high energy tail in the experiment. These differences are most likely not explained due to the simple approach used to account for the space charge effects.

5.1.3 Secondary emission from RPA grids

As discussed in Chap. 3, primary electrons are collected as a function of bias voltage by RPAs. These RPAs have two, 44% transmission grids: an entrance grid and a bias grid. It is possible for primary electrons to impact either grid and produce secondary electrons which are collected by the collector. Fig. 5-13 illustrates these types of interactions on each grid. The collector is held at a minimum of +20 V from the bias grid voltage, fully suppressing secondary emission loss from the collector. The effect of secondary emission from each grid is examined in the following sections.

Secondary emission from the entrance grid

As primary electrons strike either the entrance aperture edge or the entrance grid with sufficient energy for secondary emission, the resulting electrons are emitted with a distribution of energy like that given in Fig. 2-6. Depending on the primary impact location, the emitted electron will either be emitted in the reverse direction and will not enter the RPA, or the electron will move into the RPA as shown by (a) in Fig. 5-13. Because of the 44% grid transmission, 56% of primary electrons impact the grid, yet only a fraction of these will emit electrons into the RPA (Fig. 5-13,(a)). Because these electrons are born at the entrance grid and move into the bias potential of the RPA, they are energy-resolved and collected as a function of bias voltage. As a result, the total collected energy distribution contains the primary electron energy distribution

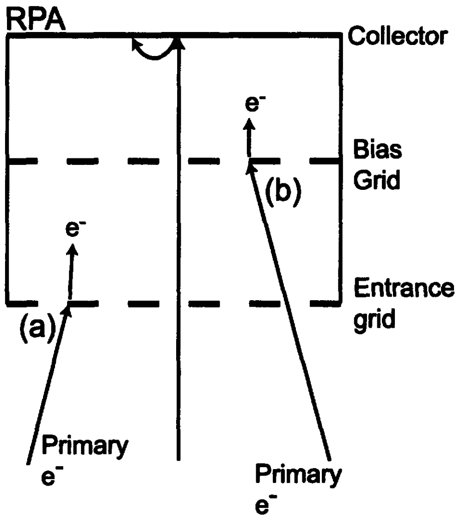

Figure 5-13: Secondary electron emission inside the RPA. In (a), a primary electron impacts an aperture edge of the entrance grid with sufficient energy for secondary emission. In (b), the same occurs on the bias grid. Secondary electrons born on the collector are suppressed by the minimum +20 V.

and a smaller secondary emission distribution from entrance grid secondary emission.

In order to add the effect of these secondaries to the simulated energy distribution, the approximate size of the secondary distribution must first be determined. The collected current density, j_c, is related to the primary electron current density, j_p, by the transmission of the two grids, or $j_p = \frac{j_c}{0.44^2}$. 56% of the primary electrons impact the entrance grid, yet the fraction of these electrons which emit electrons into the RPA is unknown. For the purpose of this discussion, 10% of primary electrons will be assumed to emit secondaries into the RPA from the entrance grid and aperture edge. Then, a secondary emitted distribution function with total number of electrons equal to 10% of j_p is added to the simulated primary electron energy distribution, as shown in Fig. 5-14. This figure shows the energy distribution with both phase and energy spreading (see Fig. 5-12) compared to the same distribution with collected entrance grid secondary electrons. These electrons add to the low energy portion (0-25 eV) of the energy distribution function, as seen in the figure.

Including secondary electrons from the entrance grid gives closer agreement to the experimental results in the 5-50 eV energy range, yet the simulation distribution is

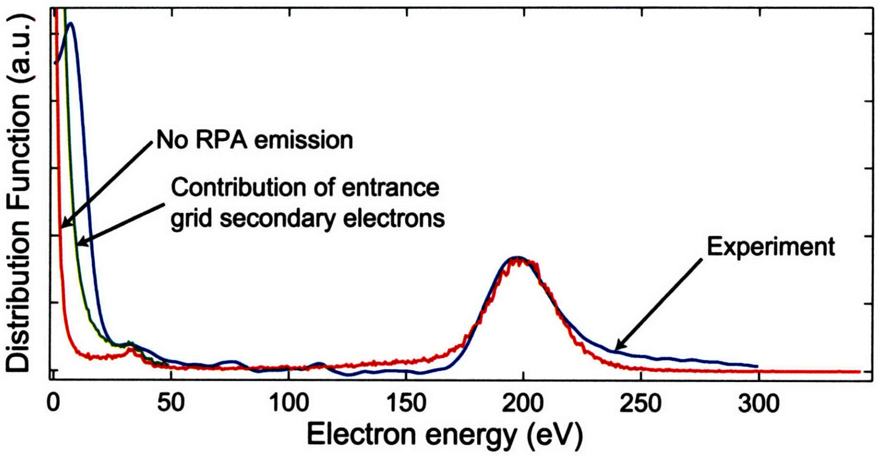

Figure 5-14: Distribution functions for 20% phase spread and 10 eV energy spread for 70 MHz and 250 V, as in Fig. 5-12, with and without the addition of secondary electrons from the RPA entrance grid, as compared to experimental results.

larger than the experimental case at very low energy (0-2 eV). This can possibly be explained by space charge inside the RPA. At very low bias voltage (0-2 V), there is very little potential between the entrance and bias grids, and therefore, these low energy electrons likely do not have sufficient energy to overcome the space charge repulsion.

Secondary emission from the bias grid

Primary electrons can also produce secondary electrons from impacts on the bias grid, shown in (b) of Fig. 5-13. As in the previous case, only secondary electrons that are emitted toward the collector are collected. Yet, in this case, they are not energy-resolved and are simply counted as current at a particular bias voltage. The question arises when the dependence of the secondary yield on the primary energy is considered. As these primary electrons enter the RPA, they are slowed by the retarding voltage between the entrance and bias grid. For example, at zero bias voltage, the primaries impact with full energy and secondary emission would be maximum. Yet if 150 eV electrons enter the RPA at a bias voltage of 100 V, they would impact the bias grid with only 50 eV, which would give rise to less secondary emission depending on the yield.

In order to see the effect of the secondary yield on the resulting energy distribution, Vaughan's formula for the secondary electron coefficient can be applied to a simulation primary energy distribution to determine the secondary electron current as a function of bias voltage [46]. The secondary current, j_{SE}, as a function of bias voltage, V_{bias}, is given by

$$j_{SE}(V_{bias}) = \int_0^\infty \delta(E) \cdot f(E + |V_{bias|})dE. \tag{5.4}$$

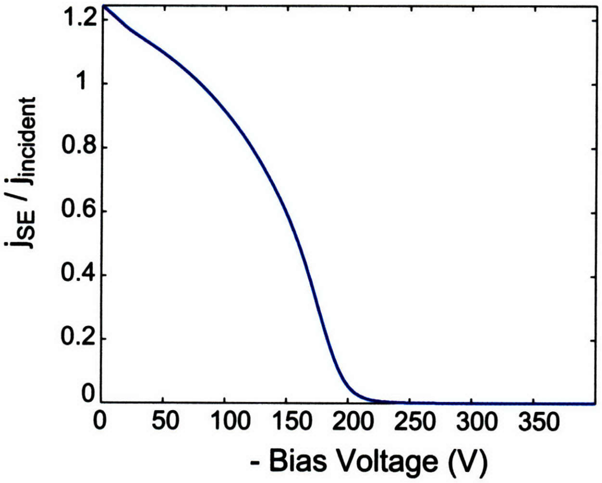

Figure 5-15: Bias grid secondary emission as a function of bias voltage. If all primary electrons caused secondary emission toward the collector at zero bias, the collected current would increase by 1.22. As the bias increases, the primaries slow and do not have sufficient energy for secondary emission.

Using stainless steel parameters for the secondary electron coefficient, the secondary yield is determined for each energy of the simulation distribution function. For secondary emission from the SS bias grid, E_1 = 90 eV, E_{max} = 330 eV, and δ_{max} = 1.4. The bias voltage is varied from 0 to -300 volts. Fig. 5-15 gives j_{SE} normalized by the number of incident electrons as a function of bias voltage. As in the case for the entrance grid, 10% of incident electrons will be assumed to give rise to forward secondary electrons at zero bias voltage. Then, this increase in current as a function of bias voltage is added to the collected I-V characteristic and differentiated to see the effect on the energy distribution. Fig. 5-16 shows both the resulting I-V characteristic and energy distribution assuming 10% of electrons incident on the bias grid emit secondaries toward to collector for zero bias. As seen, this effect is very small and can be assumed to not significantly affect the resulting energy distribution function.

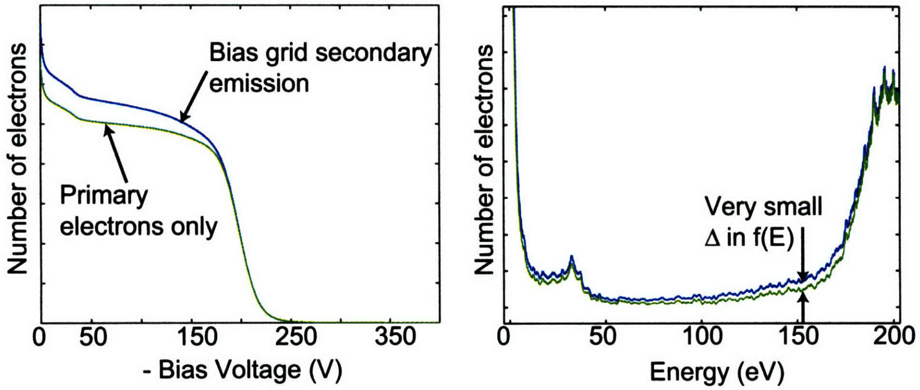

Figure 5-16: By assuming 10% of bias grid incident electrons give rise to secondary emission toward the collector, the I-V characteristic is altered, but not sufficiently to change the resulting distribution function.

5.1.4 Coaxial multipactor distributions explained: A summary of physics

By incorporating a few simple collective effects into the simple particle simulation, good agreement is found between simulation and experiment. This section summarizes the causes for all the features of the coaxial distribution function. Fig. 5-17 illustrates the experimental and simulation distribution function for electrons impacting the outer conductor. The majority of the distribution function features are a simple result of the geometry, emission energy, and phase requirements for coaxial multipactor at the particular voltage. In other words, the multipactor resonance condition explains the location of the high energy peak without accounting for any collective effects. The physics determining each of the four sections are given below.

Region I Defocused electrons due initial emission conditions and space charge of the electron sheet. Also included are secondary electrons emitted from the entrance

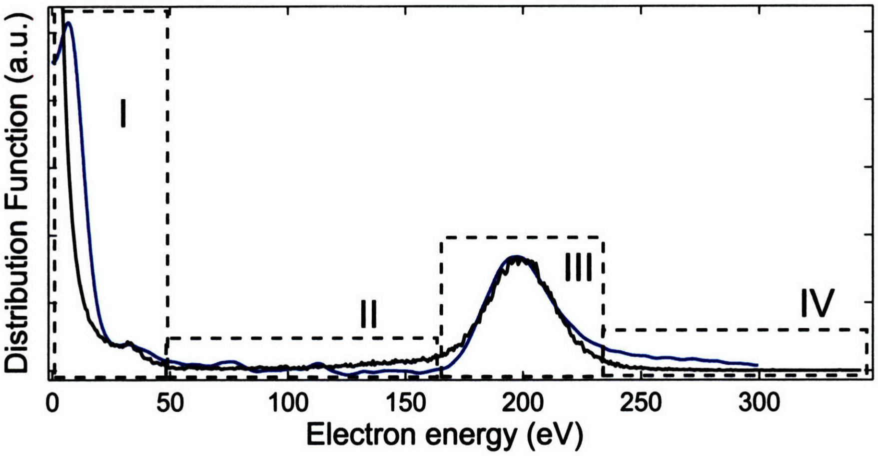

Figure 5-17: Simulation and experimental distribution functions for electrons impacting the outer conductor. The distributions are divided into 4 regions for explanation. 70 MHz, 250 V, and same coaxial geometry.

grid and aperture.

Region II Very few electrons due to the multipactor resonance condition. Small number of electrons right below Region III are O/O electrons.

Region III Mostly consists of I/O electrons, but also has some O/O electrons. Peak is located near 80% of the rf voltage due to multipactor resonance condition. Width and relative height of the peak is influenced by space charge phase spreading and energy spreading.

Region IV High energy tail consists purely of O/O electrons which pass closely by the inner conductor.

5.1.5 Effect of impurities

As described in Chap. 3, oxides and impurities on the electrode surfaces lower the minimum voltage for multipactor and increase the voltage range over which the multipactor can occur [37]. While the impurities are not measured directly on CMX, their presence can be inferred by short outgassing times and high pressure rise at the onset of the multipactor discharge. The pressure rise is due to the release of the surface impurities upon electron impact. Also, in the presence of air, Cu_2O will be formed as a result of the oxygen in the air, and this oxide will yield multipactor at a much lower rf voltage [36, 37].

Fig. 5-18 depicts experimental distribution functions for 60 MHz for clean copper electrodes and the same electrodes with Cu_2O and surface impurities. The surface impurities are due to a 10 mtorr pressure rise in the presence of a multipactor discharge that transitioned to a glow discharge. As described in Chap. 3, Sec. 3.4.1, this pressure rise led to a coating of ambient air and impurities from the Teflon windows on electrode surfaces. Fig. 5-18 displays two distributions which have the same total collected multipactor current, yet in the impurity case, this occurs for a much lower voltage. Because of the electrode oxidation and the subsequent change in the secondary emission properties, there are no experimental data for two cases at the same voltage.

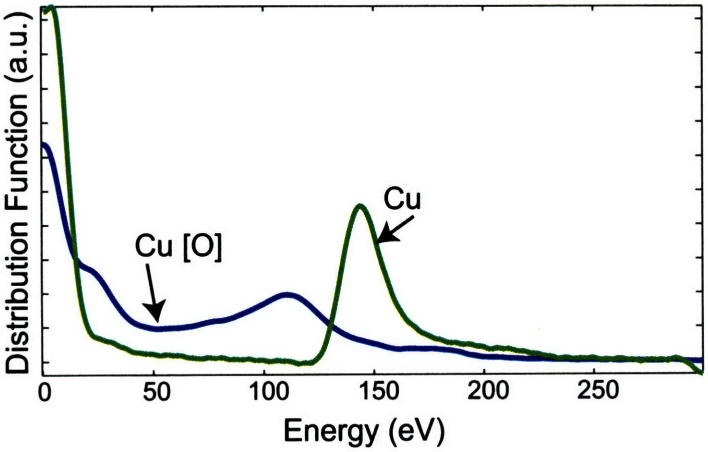

Figure 5-18: Experimental distribution functions for electrodes with and without the presence of surface impurities and oxide. Both cases are for 70 MHz, 50Ω, d_{OC}=5 cm, coaxial multipactor. The case of Cu[O] with oxide and impurities is at V_{rf}=145 V, while the clean copper case is at V_{rf}=180 V.

Both distributions have high energy populations near 80% of V_{rf} (75% impurities, 80% clean). More importantly though, the case with impurities has a much broader and smoothed distribution. As mentioned, a large pressure rise is seen in the MVC outside the coaxial vacuum region for the case with impurities, suggesting the possibility of electron-neutral collisions. As the multipactor liberates gases from the surface, the local pressure rises. Since the conductance of the coaxial region of the MVC is very low, a large rise in pressure in the multipactor region can be assumed. The electron mean free path approaches the system size near a neutral pressure of 1 mtorr. The possibility of electron-neutral collisions would have multiple effects. One effect of the electron-neutral collisions would be a smoothing of the energy distribution function as observed in Fig. 5-18. These same broader distributions are also seen by Höhn experimentally by simulating electrode gas desorption by the addition of Argon [5]. Collisions would also disturb the multipactor resonance condition and cause more electrons to be defocused in phase. This might occur for the very large group of electrons below 50 eV. Lastly, ionizing collisions could provide additional electrons to sustain the multipactor discharge at a lower voltage. The multipactor can also transition to a glow discharge below the minimum pressure for Pashen breakdown if the local pressure becomes high enough [5]. This will be discussed further in Chap. 6.

In conclusion, experiments in CMX clearly show that oxide layers and surface impurities significantly lower the necessary rf voltage for multipactor and widen the range over which the multipactor can exist. When attempting to prevent multipactor, efforts should be made to liberate all surface gases in-situ to minimize this effect.

5.2 Parallel Plate Multipactor Analysis

The main goal in measuring the electron energy distributions for parallel plates was to make connection to the work done by Höhn et. al. [5]. While Höhn's study mainly focuses on the transition of multipactor to a low pressure discharge, distribution functions were reported for vacuum pressure (7.5x10^{-7} torr), 10 cm diameter, stainless steel electrodes, 5.5 cm spacing, and 50 MHz. Also, the electrons were measured through an aperture in the center of the grounded electrode, similarly to CMX.

As in the coaxial case, similar agreement is seen in CMX experimental and simulation data. Fig. 5-19 compares experimental and simulation data for 60 MHz, 3 cm spacing, SS electrodes (E_1 = 90 eV [5]), and V_{rf} = 248 V. While the electrodes are separated by 3 cm, the 3.2 mm aperture depth is included in the distance the electron travels in the simulation.

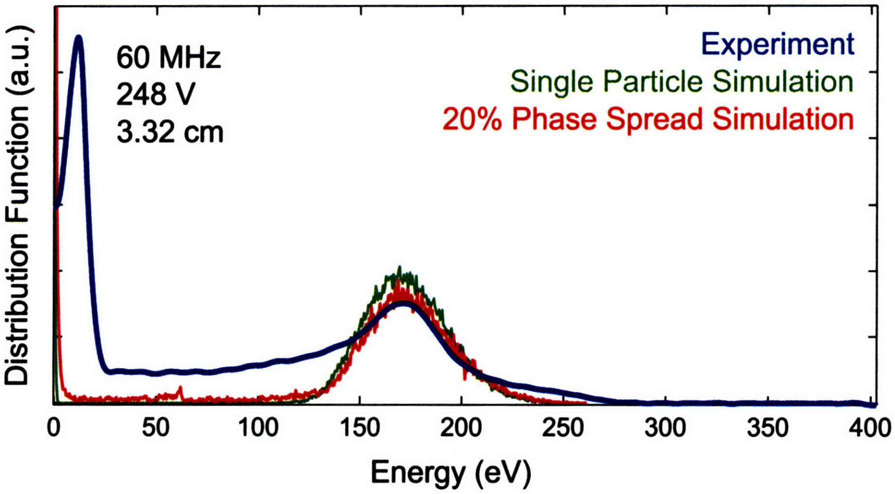

Figure 5-19: Comparison of distribution functions for experimental and simulation cases at 70 MHz and 248V. In both cases, SS electrodes were used (Simulation E_1=90 eV).

As shown, there is a good agreement of the experimental and simulation high energy populations. The location of these populations is near 70% of the rf voltage, and this location is determined by the multipactor resonance condition as in the coaxial case. The difference in the parallel plate geometry is the near linear electric field, rather than the $\frac{1}{r}$ field in the coaxial case. By adding 20% phase spread in the simulation, there is almost no change in the high energy population distribution, while there are many more electrons impacting with energy between 0 and 120 eV. Yet, the experimental distribution has a much larger number of electrons at these low energies. This more smooth distribution is most likely due to electron-neutral collisions as described in the previous section. While the parallel plate electrodes are cleaned both with multipactor and glow discharge processes, there is still the possibility of recycling off the MVC surfaces, which are not cleaned in the same manner. In the coaxial case, the multipactor region is shielded from MVC recycling by the outer conductor.

The same agreement in the high energy population location is seen for the simulation and experimental distributions at 60, 70, 80, and 90 MHz. Also, simulation cases were run with the parameters and rf voltages of Höhn's experiment; i.e. 50 MHz, SS electrodes, 5.5 cm gap. The simulation results yield good agreement with his experimental results as well. Fig. 5-20 shows the excellent agreement of the peak energy of the high energy populations, E_{peak}, between experimental and simulation data. Shown in the second panel of Fig. 5-20, in almost all cases, E_{peak} is near 70% of the MVC voltage.

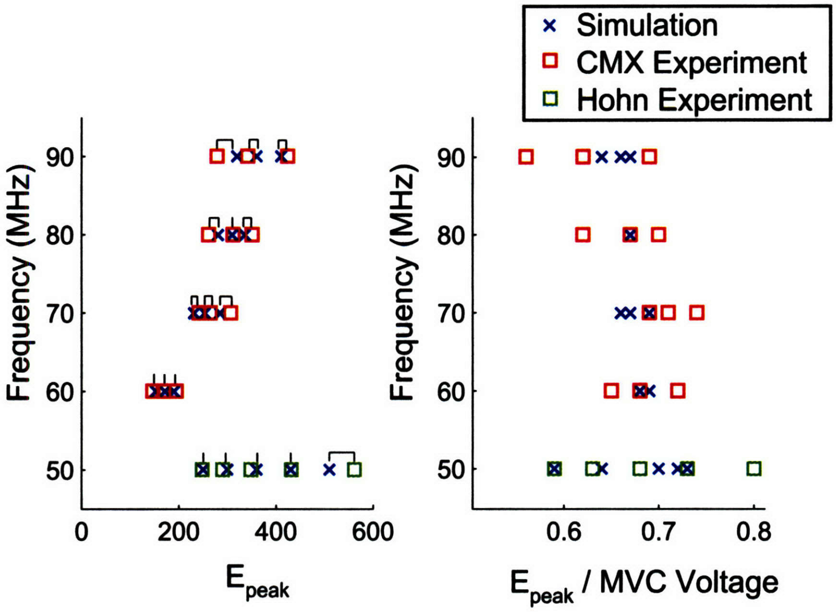

Figure 5-20: Peak location of the high energy population illustrating the agreement between simulation and experiment. The lines on the left panel connect experiment and simulation cases of the same rf voltage. Also shown and in good agreement are data from [5] and the corresponding simulation data.

5.3 Comparison of Coaxial and Parallel Plate Distributions

Coaxial and parallel plate multipactor discharges differ as a result of the particular electric fields in each transmission line geometry. The non-linear, $\frac{1}{r}$ field of the coaxial line yields a higher energy distribution function than the distribution function of the parallel plate multipactor. Fig. 5-21 compares simulation distribution functions for the two geometries with the same electrode spacing of 2.82 cm, corresponding to the 50 Ω, 10 cm outer conductor, coaxial line. Both cases are run for 70 MHz, $V_{rf} = 250$ V, E_1=125 eV, and a 20% phase spread.

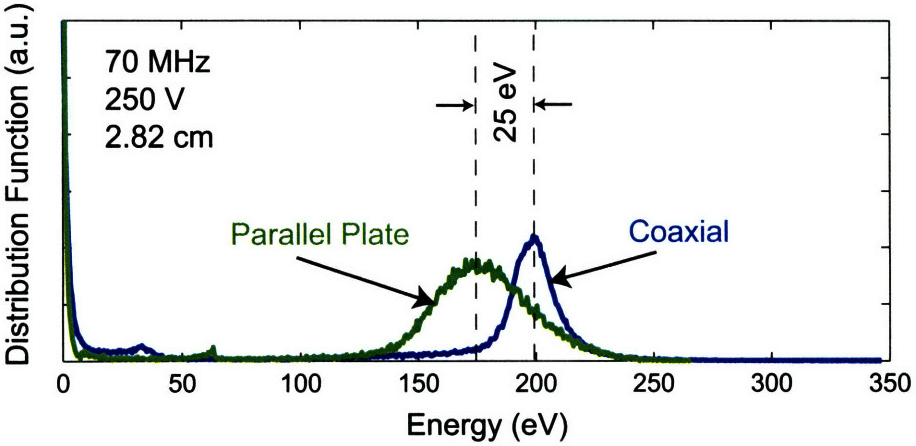

Figure 5-21: Comparison of the coaxial and parallel plate distribution functions at 70 MHz, 250 V, electrode spacing of 2.82 cm, and E_1=125 eV. The coaxial multipactor yields a higher energy distribution function than the parallel plate case.

The coaxial distribution has a high energy population at 80% of the rf voltage and 25 eV higher than the high energy population in the parallel plate case, at 70% of the rf voltage. The same ratio of the high energy population to rf voltage is seen experimentally, illustrated for several frequencies in Fig. 5-22. In this figure, the parallel plate electrodes have a 3 cm spacing, while the coaxial spacing is only 1.8 mm smaller, so it can be approximated as equal spacing. The coaxial multipactor consistently has a high energy population near 80%, while the parallel plate multipactor is always less, near 65-70%.

The result of this difference in the high energy population peak suggests that coaxial transmission line is more susceptible to multipactor than a stripline of similar electrode spacing. Often, transmission lines systems consist of both parallel plate or stripline sections and coaxial sections. Because the coaxial multipactor has a higher energy electron distribution, the electrons would reach the multipactor resonance con-

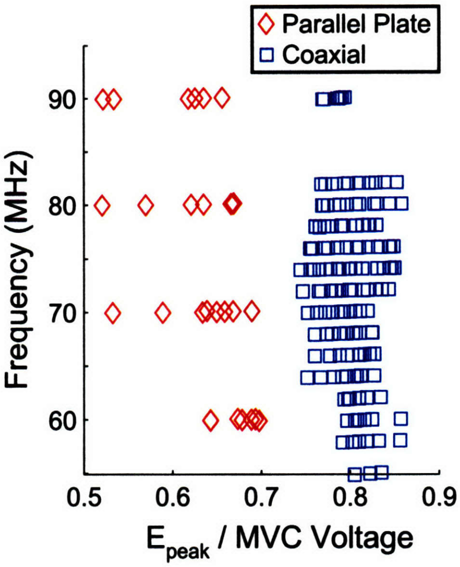

Figure 5-22: High energy population maximum as a percentage of the rf voltage. For all frequencies tested, the coaxial high energy population is at least 10% higher than the parallel plate case.

dition first in the coaxial section. This is observed experimentally on CMX in two ways. The first observation is in the susceptibility diagram, comparing the onset voltage of parallel plate and coaxial electrodes, as illustrated in Fig. 5-23. For frequencies from 50 to 90 MHz, the parallel plate multipactor voltage is a few tens of volts higher than the coaxial voltage. The second observation indicating the higher susceptibility of coaxial electrodes was a fortunate design mistake in CMX. As illustrated in Fig. 5-24, initially there was a very short (1 cm) section of exposed coaxial electrodes in the parallel plate configuration. When attempting to measure the parallel plate multipactor, a rise in reflection coefficient could be seen, while no current could be measured on the RPA. It was determined that coaxial multipactoring in the short region before the parallel plates was occurring, and therefore, preventing the multipactor from forming in the measurement region. In order to prevent this unwanted coaxial multipactor, a 2 cm teflon spacer was placed between the two coaxial electrodes. Subsequently, multipactor current was detected between the parallel plate electrodes, as hoped.

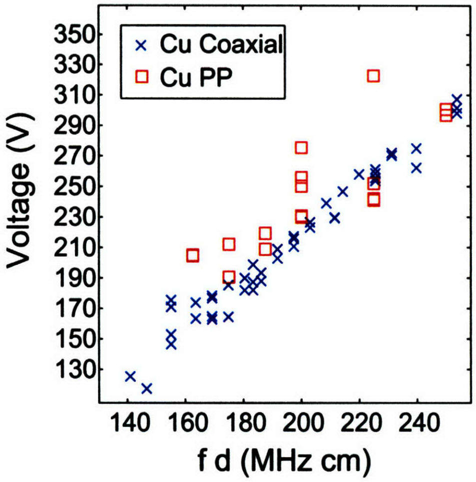

Figure 5-23: Susceptibility diagram for copper electrodes in both parallel plate and coaxial geometries.

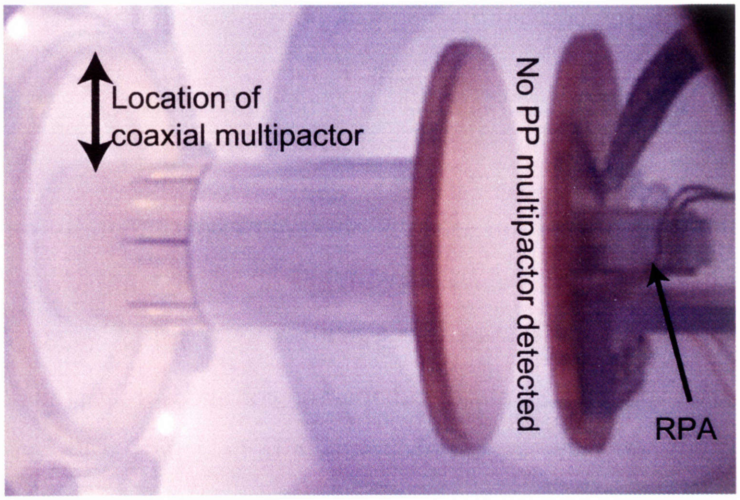

Figure 5-24: Initially, coaxial multipactoring prevented a parallel plate multipactor from forming. By placing a teflon spacer in the short coaxial region, parallel plate multipactor current was measured between the desired electrodes. This image was taken in the presence of an argon glow discharge.

5.4 Scaling Laws and Rule of Thumb Equations

As mentioned in Chap. 2, the voltage for a multipactor in a simple parallel plate geometry scales with $(f \cdot d)^2$, but no simple theoretical scaling relationship can be determined for the coaxial case due to the non-linear equations. Numerical analysis has shown the same scaling relationship holds for coaxial electrodes [48]. CMX data verifies these scaling relationships of V$\propto$ $(fd)^2$ in both parallel plate and coaxial geometries. All data can be fit rather well with an equation of the form $y = ax^2 + b$, and the constants can be determined for the cases of parallel plate and coaxial electrodes. Also the effect of surface oxides and impurities can be included in deriving these "Rule of Thumb" equations by fitting the data for those cases. Table 5.1 gives the fit coefficients and respective error for coaxial, parallel plate, and coaxial with surface oxide/impurities multipactor susceptibilities.

	a·10^3 $(\frac{Volts}{(MHz\cdot cm)^2})$	b $(Volts)$	R^2	RMSE
Coaxial	3.93	57.8	0.985	9.53
Parallel Plate	4.34	18.7	0.935	45.07
Coaxial (oxide/impurities)	1.56	65.23	0.971	7.95

Table 5.1: Fit properties for CMX experimental data using equation of the form $V = a \cdot (fd)^2 + b$, where V is in volts and fd is in MHz cm.

Fig. 5-25 shows the data with curve fits for the 3 cases, along with the theoretical zero electron emission multipactor bands derived by Kishek [1]. It is important to note that, experimentally, multipactor occurs at a lower voltage than that given by simple theory which does not include the initial energy distribution of the secondary electrons. Therefore, including the initial distribution of secondary electron emission energy is critical in the development of the multipactor.

The coaxial data curves fit the data quite nicely with low RMSE. Because of the different electrode materials tested in the parallel plate case, there is a larger RMSE for the corresponding fit. The following equations can be used for the frequency range of 50-100 MHz to determine the approximate voltage for multipactor in coaxial and parallel plate geometries. For all equations, V is in volts and fd is in units of MHz·cm.

$$V_{coaxial} = 4 \cdot 10^{-3}(fd)^2 + 10, \tag{5.5a}$$

$$V_{pp} \approx V_{coaxial} + 10 \text{ volts}, \tag{5.5b}$$

$$V_{coaxial}^{oxide} = 1.6 \cdot 10^{-3}(fd)^2 + 65. \tag{5.5c}$$

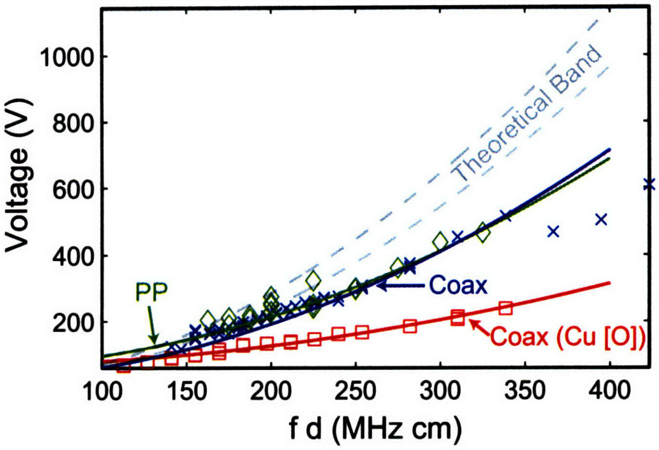

Figure 5-25: Susceptibility data curve fits for coaxial, parallel plate, and coaxial with oxide/surface impurities. Also shown are the bounds for multipactor as determined by Kishek's zero emission model [1].

As a general rule observed in CMX experiments, surface impurities typically lower the multipactor voltage 50 to 100 V due to the lower E_1 of the secondary electron coefficient. Lastly, as a rule of thumb for the frequencies and gaps used in this study, the multipactor voltage band between onset and push-through typically ranges from 200 to 400 volts. In certain cases, it may be possible to design a multipactor-free VHF system with electrodes spaced 1-5 cm such that multipactor susceptible voltages cannot exist in the transmission line sections of interest. In this case, the lower multipactor band (onset voltage) can be taken from the above equations, and the upper band (push-through) can be conservatively approximated as 0.5 to 1 kV above the onset voltage.

Chapter 6

ICRF Operational Neutral Pressure Limits on Alcator C-Mod

Fusion research experiments commonly use high power radio frequency heating to achieve high temperature plasmas. Ion cyclotron range of frequencies (ICRF) heating is one of the most prominent auxiliary heating techniques used in current experiments, such as Alcator C-Mod, which uses up to 8 MW of ICRF source power in three antenna systems [13, 61]. ICRF heating is also planned to be used for the International Thermonuclear Experimental Reactor (ITER) [12], and the design of these rf systems are currently underway.

With any high power rf system, the primary concern and operational limitation is voltage breakdown. When rf power is operated in the plasma environment of a fusion device, factors such as multipactor, neutral pressure, magnetic field, and ionizing radiation can further complicate conditions leading to voltage breakdown and cause more severe limitations on rf operation. While impurity generation and density production can also limit the high power rf systems on fusion experiments [13, 62], voltage breakdown continues to be the primary limiting factor for successful and consistent operation. Consequently, the design criteria of many rf systems is based on successful avoidance of all types of voltage breakdown. The work described in this chapter will focus on the connection between voltage breakdown and observed operational neutral pressure limits, which are both introduced in the subsequent sections. As will be shown, this investigation ties voltage breakdown as a multipactor discharge to the observed neutral pressure limit. With this information, rf systems such as those on ITER can be designed for more successful and consistent operation over a wider range of operating conditions.

6.1 Voltage Breakdown in rf Systems

Voltage breakdown can occur in fusion systems under many different conditions. One way in which it can occur is high voltage arcing [63, 64, 65, 66, 67, 68], which can occur at electric fields of order 10 kV/cm [31, 69]. This high voltage breakdown occurs on Alcator C-Mod for electric fields near 15 kV/cm along magnetic field lines, and for typical electrode spacings, a voltage of 40 kV [34]. This high voltage breakdown can transition to a gas discharge (also called a glow discharge), as the electron mean free path becomes small enough to cause electron avalanche by ionization [15]. This typically occurs at pressures above 10 mtorr, but depends on the gas and respective ionization cross sections [63, 64, 69, 70]. These discharges typically follow a Paschen law scaling with the breakdown voltage proportional to the product of pressure and distance [71, 72]. Rf glow discharges are possible on fusion experiments (50-90 MHz); therefore, in order to avoid this type of breakdown, fusion experiments are operated with neutral pressures well below that necessary for a pure rf glow discharge.

On the other hand, if conditions are favorable, voltage breakdown can occur as a multipactor discharge as previously discussed. The multipactor electrons are entirely supplied by secondary emission, as electron-neutral collisions are too infrequent for ionization. Yet, as the pressure increases and the electron mean free path approaches the system size, the multipactor discharge can transition to a glow discharge at a pressure lower than that expected for a pure rf discharge [5, 73, 74, 75]. Fig. 6-1 depicts the multipactor onset voltage as a function of background pressure on CMX. The upper red curve (square data points) gives the voltage just before the multipactor or glow discharge begins, and the lower blue curve (star data points) gives the voltage after the onset of the particular discharge.

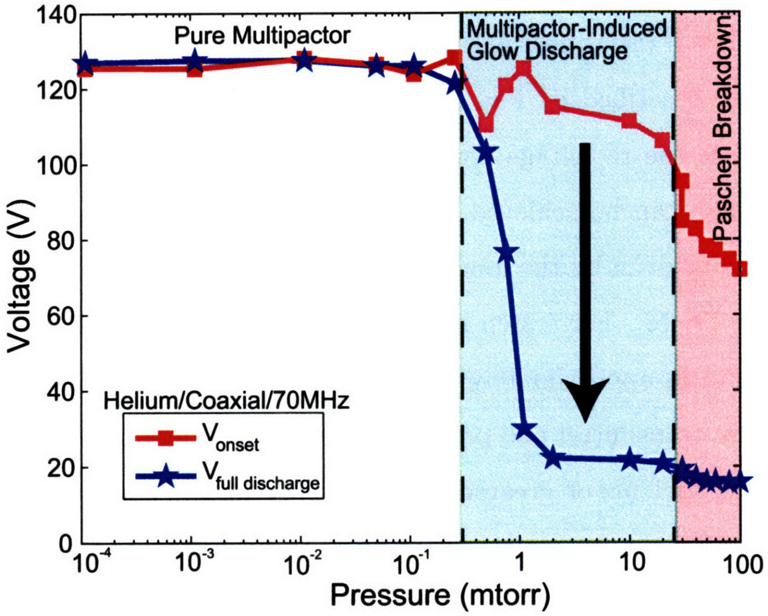

Figure 6-1: Multipactor onset voltage as a function of pressure. Data from Coaxial Multipactor Experiment [29].

As shown in Fig. 6-1, at low pressure and large mean free paths, the onset voltage of the pure multipactor holds constant near 125 V at pressures up to 0.1-0.2 mtorr. At 0.1-0.2 mtorr, the multipactor transitions into a multipactor-induced glow discharge or "multipactor plasma" [5]. Within this pressure range, the multipactor discharge supplements electrons for a glow discharge far below the expected Paschen breakdown pressure, given by the red region on the right side of Fig. 6-1. The glow discharge causes a very large change in cavity impedance, and there is a dramatic drop in circulating rf power. This drop in circulating power is illustrated in Fig. 6-1 by the large voltage decrease between the onset voltage (red curve) and the voltage after the discharge has developed (blue curve). Once this multipactor-induced glow discharge is initiated, push-through cannot be achieved because of the large drop in cavity voltage.

As previously mentioned, multipactor occurs because geometry, frequency, and δ all combine to provide the proper resonance conditions for electrons in the rf field. If multipactor can be prevented or avoided by changing any of these criteria, breakdown will not occur until the pressure given by the Paschen curve, as described by Höhn and seen on CMX. The rf rise time is also important in determining whether a multipactor can be initiated, described by Fig. 6-2. If the multipactor has insufficient time to develop such that the rf voltage rise time is faster than the multipactor rise time, then push-through can be achieved up to the Paschen breakdown pressure. The rf system rise time is given by the longer of the cavity time constant, $\tau_{rf} = \frac{Q}{\omega}$ and the rf rise time [76, 77, 78]. For a step increase in rf power, the rf voltage will rise from zero to maximum in approximately 0.2 μs for a Q=100 and 80 MHz. Yet for high power rf systems, transmitter and protection circuit considerations typically limit the voltage rise time to 1 ms or greater. The multipactor rise time is of order 100-200 rf cycles [50], so for the frequencies of interest and current arc protection circuitry, multipactor typically has sufficient time to fully develop.

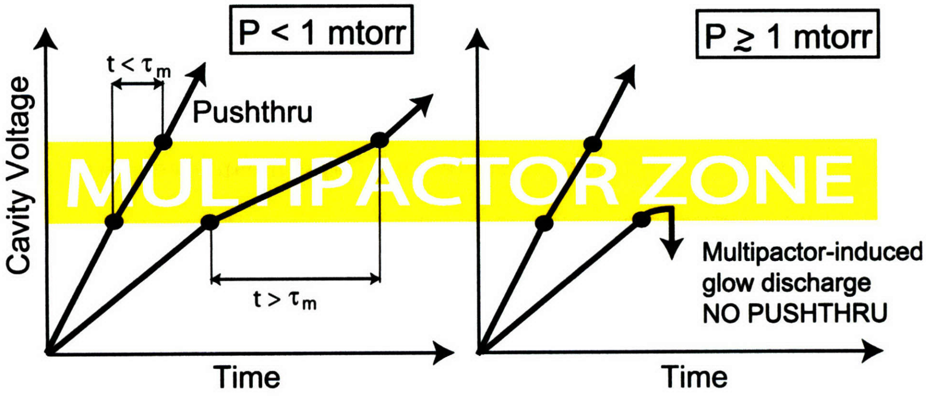

Figure 6-2: Independent of pressure, push-through can be achieved if the rf is increased with time less than the rise time of the multipactor (τ_m). However, at high pressures, push-through can not be attained when $t_{rf} > \tau_m$.

Typically for pressures below 0.1 mtorr, multipactor push-through can be achieved for any rf rise time as long as the system can tolerate the reflected power caused by the multipactor discharge. However, if multipactor can occur at pressures in the range for a multipactor-induced glow discharge, this discharge will form below the minimum Paschen pressure and cause a substantial loss of rf power to the load. Push-through cannot be achieved. Fig. 6-2 illustrates this effect of pressure on multipactor push-through.

6.2 Neutral Pressure Limits on Alcator C-Mod

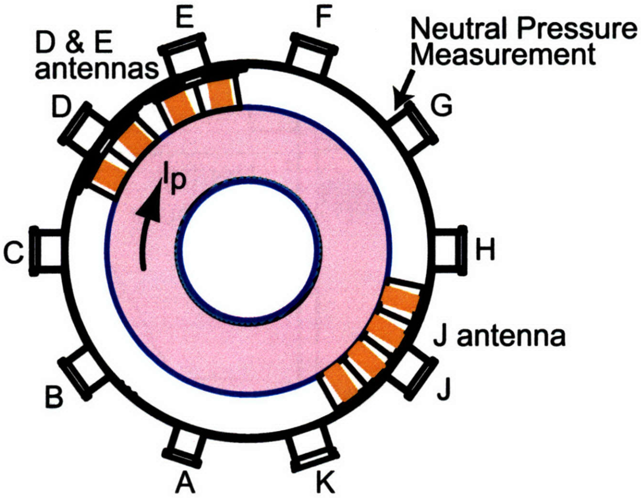

Figure 6-3: Plan view of Alcator C-Mod ICRF power systems.

Alcator C-Mod uses ICRF power from 40-80 MHz with three antenna systems for auxiliary plasma heating [13]. Fig. 6-3 depicts a plan view of the torus and associated ICRF antennas. Both E and J antennas, named for their respective ports, have experimentally observed neutral pressure limits above which they cannot be operated. This operational limit can be seen in Fig. 6-4, identified by the sharp drop in rf power at elevated neutral pressure. Limits of 1.0 mtorr and 0.5 mtorr on the E and J antennas respectively are consistently seen to prohibit C-Mod antenna operation, and once this pressure has been reached, the rf power cannot be restarted. This inability to restart can be seen in the shaded areas of Fig. 6-4. The short, low power rf pulses are repeated attempts of the rf restart, which immediately result in a fault. It should be noted that the Alcator C-Mod ICRF voltage rise time is 5 ms, determined by the feedback circuit of the arc protection system. Also, the neutral pressure is determined by plasma transport properties, such that if transport is high, the neutral pressure is typically also high [79]. The neutral pressure is measured near G port in the discussed experiments.

Because the rf power is applied to antennas which reside inside the vacuum chamber, vacuum transmission lines are inevitable [80]. In both E and J antennas, there

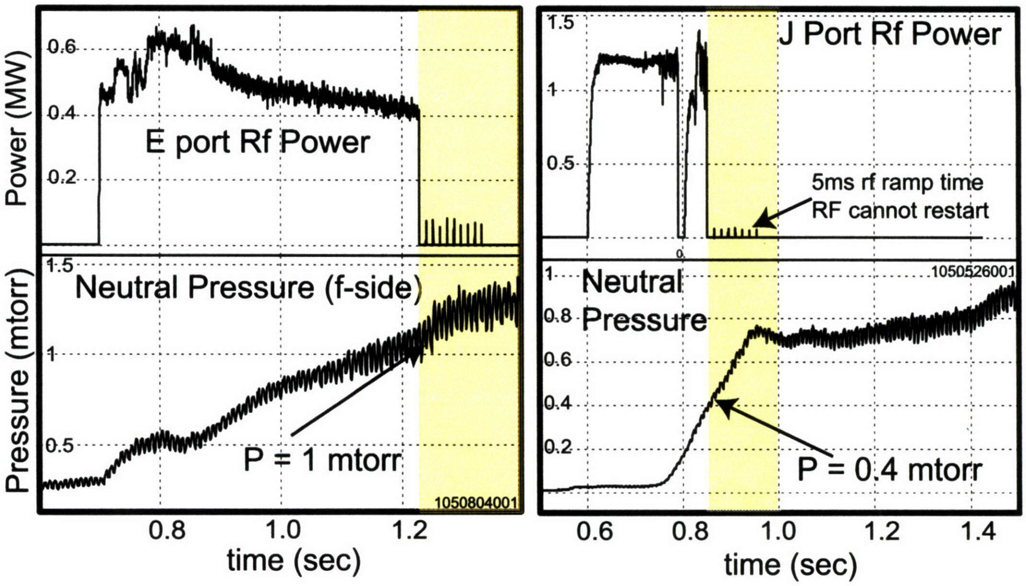

Figure 6-4: Experimentally-observed neutral pressure limits on E and J ICRF antennas on Alcator C-Mod. This neutral pressure limit is seen during typical C-Mod operation, which includes a 5.4 T magnetic field in the center of the tokamak plasma.

are coaxial vacuum windows connected to short sections of coaxial transmission line which bring the rf power into the vacuum. The coaxial transmission line connects to a stripline waveguide, for which $E_{rf} \perp B$, where B is the toroidal magnetic field. Fig. 6-5 illustrates a simplified schematic of the C-Mod ICRF system inside and outside the vacuum chamber. The E and J antenna systems will be shown to have different susceptibilities to multipactor, and this is likely due to the differences in vacuum transmission lines between the two systems. As shown in Fig. 6-6, the rf vacuum feedthroughs connect to short sections of vacuum coaxial transmission line with copper inner and outer electrodes, which are susceptible to multipactor. This region is given by the shaded region in Fig. 6-6. The J antenna system has a vacuum coaxial section twice as long as the E system, and the J port electrode spacing is also 3 mm larger than the E system. The impedances of these multipactor susceptible sections are 40Ω and 46.5Ω for the E and J coaxial electrodes. Due to the complex nature of these antenna systems, the standing wave pattern and the rf voltage in multipactor-susceptible regions are not currently known with and without plasma loading. This is an area of future work to be discussed in the next chapter.

As a result of the neutral pressure observations, an experiment was initiated to investigate multipactor discharges in the C-Mod rf antenna systems in the absence of plasma to determine if the observed pressure limits could be correlated to multipactor-induced glow discharge. The experiments on the C-Mod systems, described in Sec. 6.3, are further developed and supported by experiments on CMX, discussed in Sec. 6.4.

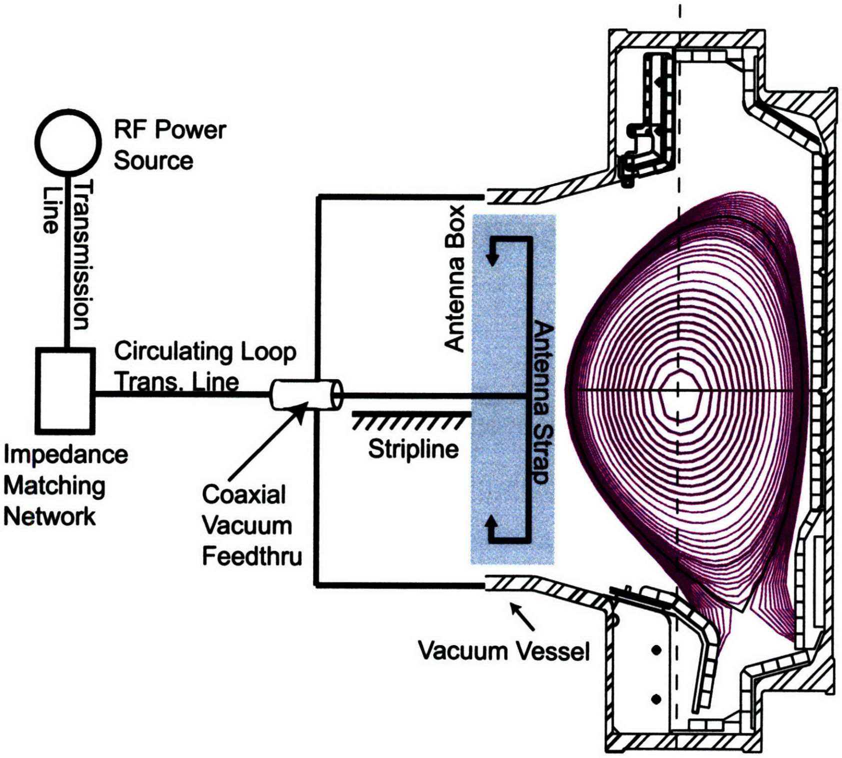

Figure 6-5: Simplified schematic view of the ICRF system of Alcator C-Mod. On all three antenna systems, there are sections of vacuum coaxial and stripline transmission lines which are susceptible to multipactor.

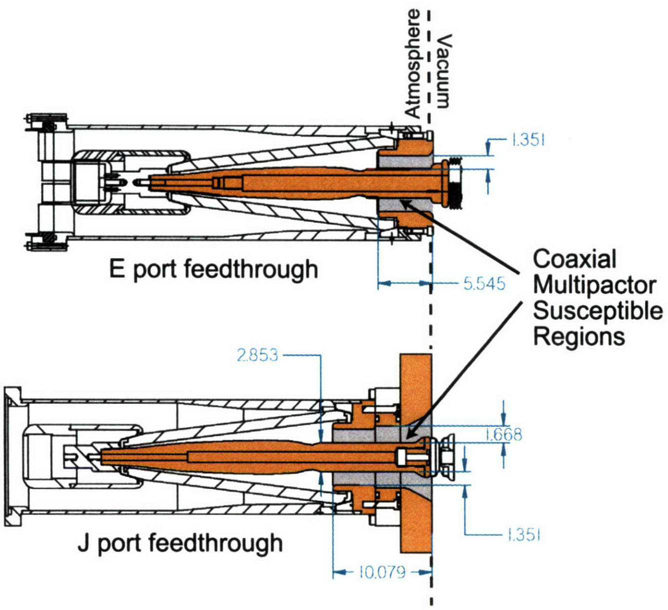

Figure 6-6: Rf vacuum feedthroughs for both E and J antenna systems. All dimensions are given in cm.

6.3 C-Mod Multipactor Experimental Procedure and Results

Multipactor experiments, similar to those on CMX, were performed on the E and J antennas in the absence of tokamak plasma. As mentioned, these antennas systems have short sections of vacuum transmission line which are susceptible to multipactor discharges. Both E and J antennas, operating in the two-strap configuration [61], were tuned in vacuum to 82 and 78 MHz respectively and tested for multipactor at these respective frequencies. In order to investigate C-Mod multipactoring, rf power was directed into the ICRF antenna system and increased in steps (0-250 W) at deuterium pressures typical of C-Mod operation (10^{-6} to 1 mtorr). Fig. 6-7 illustrates the series of forward power measurements for a range of pressures. The experiment was done with and without the presence of a 0.1 T toroidal magnetic field. Directional coupler pairs at the source and in the unmatched section measured forward and reflected power in order to determine the presence of a multipactor discharge.

Experimental results are shown in Fig. 6-8 and 6-9. Both antennas were found

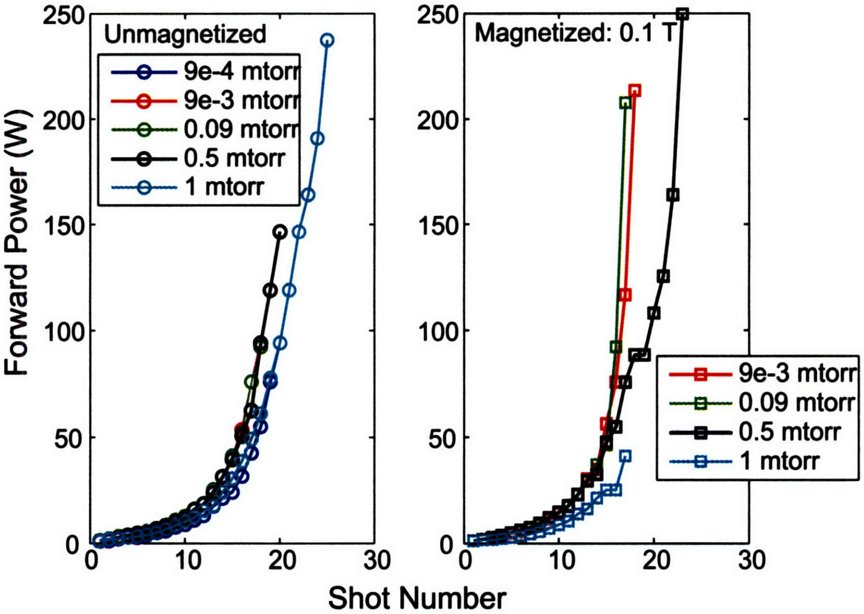

Figure 6-7: Input powers at increasing neutral pressures for the C-Mod multipactor experiments.

susceptible to multipactor discharge in both unmagnetized and magnetized cases. The multipactor discharge can be observed by a change in the reflected power amplitude, as shown by Fig. 6-8(a) and 6-8(b). As in CMX, the multipactor detunes the rf system such that a rise in the reflection coefficient can be seen accompanying the discharge. In all unmagnetized cases below 1 mtorr, multipactor push-through can be seen on both figures as the reflection coefficient drops back down the original level near 0.1. For J (unmagnetized, 1 mtorr; magnetized, 0.5 and 1 mtorr) and E (magnetized, 0.5 and 1 mtorr), push-through did not occur, as these cases results in a glow discharge. This will be discussed shortly.

Looking at the unmagnetized case of Fig. 6-8(a) and 6-8(b), the multipactor band (onset to push-through) and reflection coefficient is a bit larger for J port, yet push-through occurs at the same input power of 50 W in both cases for 0.01 mtorr and below. Interestingly, the J port reflection coefficient initially decreases with the onset of the multipactor. This larger multipactor band for the J system is likely due to the 5 cm longer vacuum transmission line section, as described by Fig. 6-6. The longer line length allows the multipactor more possible locations to occur along the standing wave

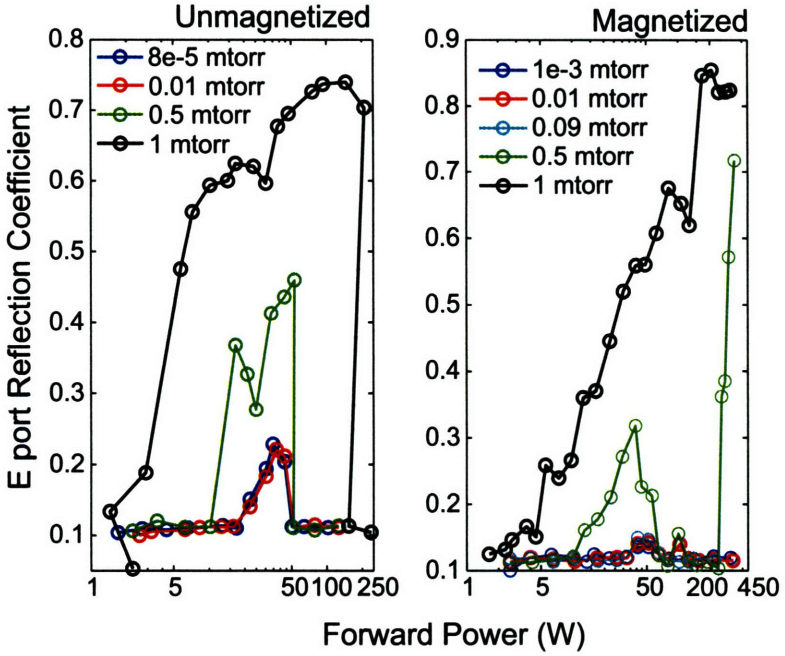

(a) E port reflection coefficient with forward power.

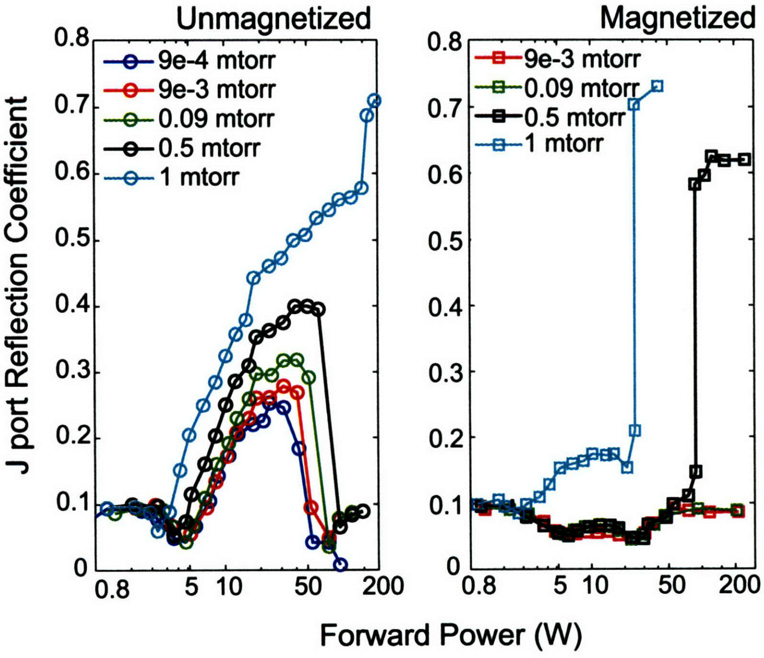

(b) J port reflection coefficient with forward power.

Figure 6-8: Reflection coefficient with forward power in the E and J port multipactor experiments. Both experiments were performed in the absence of a tokamak plasma, with and without the presence of a 0.1 T magnetic field.

pattern in that region. For the magnetized cases shown, the multipactor detunes the cavity much less, as shown by the much smaller increase in the reflection coefficient. The multipactor still exists approximately over the same band, yet it actually causes a slight reduction in the reflection coefficient for the entire multipactor band on J port.

Fig. 6-9 illustrates the circulating voltage ($V_{circ}=\sqrt{2\cdot 50P_{circ}}$) with increasing forward power. In each panel of both figures, a dashed curve illustrates the theoretical voltage rise for a resonator with Q=500 if no multipactor or other nonlinear reactive element is present. With the presence of multipactor, the circulating voltage increases more slowly due to a reduction in Q and increase in reflected power. The multipactor causes the flatter regions of the curves shown in Fig. 6-9(a) and 6-9(b). Also, multipactor push-through can be seen on both antennas in the unmagnetized case by the sudden increase in the circulating voltage measurement.

As before, unmagnetized push-through can be seen for all pressures on the E antenna, yet for the J antenna, push-through could not be achieved at 1 mtorr, indicated by the sharp drop in voltage in the first panel of Fig. 6-9(b). This drop in voltage is identical to the sharp drop in voltage in CMX and Fig. 6-1, indicating the onset of a glow discharge. The magnetized cases can be seen in the second panels of Fig. 6-9(a) and 6-9(b). As mentioned, the magnetized multipactor detuned the rf circuit less at low pressure than the unmagnetized case, which can be seen as closer agreement of the data to the dashed line representing the multipactor-free, theoretical voltage rise.

The most important results of these experiments are given by the large drops in rf voltage in the shaded regions of Fig. 6-9(a) and 6-9(b). These drops are an indication of multipactor-induced glow discharges occurring in both E and J antenna systems in the presence of magnetic field at minimum pressures of 1.0 mtorr and 0.5 mtorr (black curves of Fig. 6-9(a) and 6-9(b)). This circulating voltage drop is accompanied by a nearly total reflection of forward power, and once this discharge is established, no additional forward power can increase the circulating voltage. The magnetized onset of glow discharge at pressures of 1.0 mtorr and 0.5 mtorr for the E

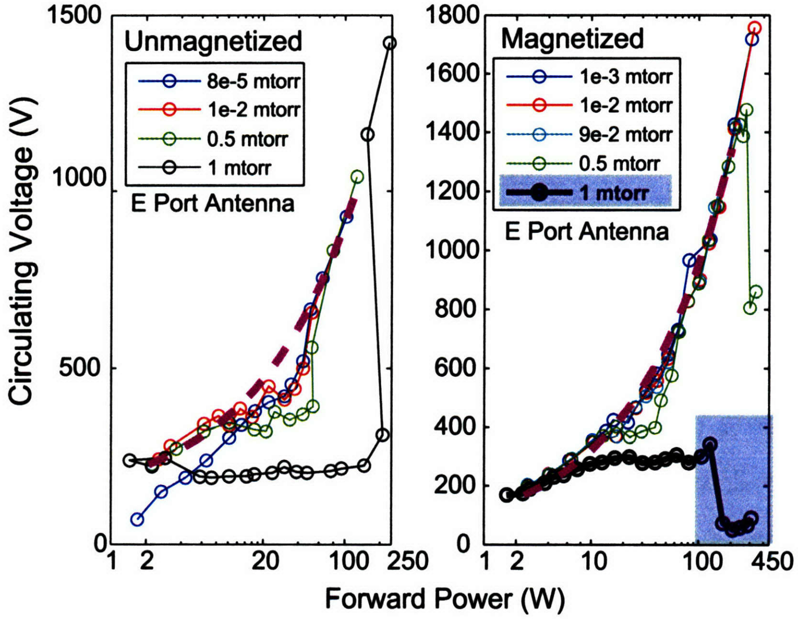

(a) Circulating voltage versus forward power for E port. Glow discharge onset occurs in the magnetized case at 1 mtorr, seen by the large drop in voltage.

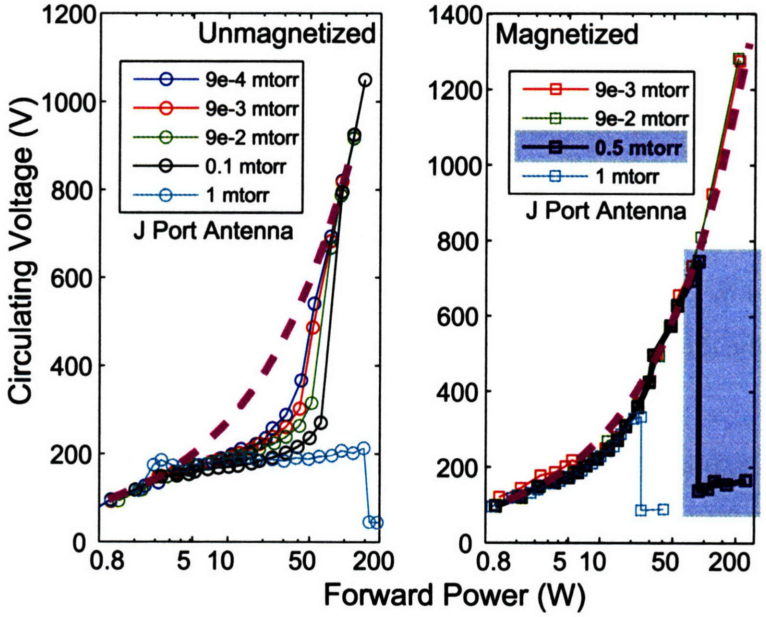

(b) Circulating voltage versus forward power for J port. In the magnetized case, glow discharge onset occurs at 0.5 mtorr.

Figure 6-9: Multipactor susceptibility of the E and J port antenna systems. The theoretical circulating voltage rise for a Q=500 resonator in the absence of multipactor is given by the dashed curve.

and J systems respectively correlates very well with the operational neutral pressure limits occurring at the same pressures for each system. The following section will describe CMX experiments which aim to demonstrate that the operational neutral pressure limit is set by this multipactor-induced glow discharge, below the Paschen breakdown limit, and in the presence of a magnetic field.

6.4 CMX Supporting Experiments

In order to verify that the observed correlation between the neutral pressure limits and glow discharge onset is indeed a result of a multipactor discharge, several unmagnetized experiments were performed on CMX. Because of the versatile nature of the CMX, various experiments and configurations can be investigated in which multipactor is either produced or prevented to determine the experimental criteria surrounding this multipactor-induced glow discharge. In these different experiments and configurations, the background pressure can be increased until the observation of a glow discharge in order to determine the factors contributing to glow discharge at the same pressures of the C-Mod experiments.

The CMX neutral pressure can be varied similarly to the low power C-Mod experiments, in the pressure range of 10^{-7} to 100 mtorr. Both argon and helium are used as the background gas in these experiments. If CMX conditions are set such that multipactor discharge is possible, a glow discharge will initiate in the pressure range given by the middle, blue band of Fig. 6-1, below the minimum Paschen pressure. For example, at 80 MHz and parallel plate electrodes spacing of 3 cm, a strong multipactor can be seen at low pressure, and correspondingly, the breakdown voltage varies with pressure identically to that shown in Fig. 6-1 and by Hohn [5]. Generally on CMX, in the presence of multipactor, a glow discharge is first observed between the 3 cm spaced parallel plates at 0.4 to 0.8 mtorr for Argon and 0.7 to 1 mtorr for Helium. When multipactor is successfully prevented, the glow discharge is first observed at 10 to 14 mtorr for Argon, which corresponds to the pressure for Paschen breakdown. The following text will describe the experiments in which these limits are determined.

The minimum pressure of 10 to 14 mtorr for a pure, Paschen glow discharge was determined by preventing multipactor in a variety of ways. In the first set of experiments, multipactor discharge was suppressed by changing the geometry, frequency, or δ so that no multipactor could be detected. For instance, with a parallel plate spacing of 1 cm and operating frequency of 50 MHz, no multipactor could be detected due to the insufficient criteria for electron resonance. The most successful experiment, which allowed the same rf and geometry multipactor resonance conditions, implemented electrode materials with δ below unity, preventing multipactor by suppressing secondary emission. The electrode materials tested were pure titanium, titanium nitride (TiN), and 50 μm sandblasted copper at frequencies between 50 and 90 MHz with a gap spacing of 3 cm. These electrode material experiments are also important for the discovery of a material for future implementation on Alcator C-Mod to prevent multipactor discharge and the associated glow discharge at lower pressure.

First, titanium electrodes, which were in-situ argon-etched to expose the $\delta < 1$ pure titanium surface, were only partially successful in reducing the multipactor. In this case, multipactor could not be seen initially but would return after a short time. The effectiveness of the rf discharge etching process was unknown, and it is likely that exposed titanium oxidized rapidly as oxygen was introduced slowly into the MVC. Second, TiN was unsuccessful in eliminating multipactor on CMX. Castañeda has shown that exposure to air and oxygen changes the secondary emission characteristics of TiN such that δ is not less than unity for the energies of interest [43].

Lastly, as discussed in Chap. 2, surface roughening has been shown to effectively reduce the secondary emission coefficient in order to prevent multipactor [16, 36, 45]. This effect would presumably be even more effective in the presence of a magnetic field, as the particles emitted will follow a Larmor orbit perpendicular to the surface, increasing the chance of reimpacting the surface. For a 5.4 T toroidal magnetic field at the major tokamak radius, the magnetic field near the coaxial vacuum transmission lines is approximately 3.5 T, and a secondary electron emitted with 5 eV has a Larmor radius near 2 μm.

With the availability of sandblasting with a grit size of 10 to 50 μm, it was proposed to apply this type of surface treatment to copper electrodes and potentially prevent multipactor, while retaining good copper rf conductivity and vacuum requirements necessary for Alcator C-Mod and other fusion experiments. This surface was shown to completely prevent multipactor at all frequencies tested after the surface was glow discharge cleaned for a few minutes. This sandblasted surface is now being proposed for implementation on the rf vacuum transmission line sections on Alcator C-Mod, as discussed in Sec. 6.6.

In all the previously discussed experiments, the voltage was increased very slowly in a stepwise manner, allowing more than sufficient time for the multipactor to develop. Another set of CMX experiments investigated the effect of the rf voltage rise time on the onset of glow discharge. Multipactor can be eliminated by increasing the rf voltage faster than the multipactor rise time, as described in Fig. 6-2. This was done on CMX by allowing the rf voltage to rise with the intrinsic time constant of the cavity (Q$\sim$200, f=70MHz, $\tau_{rf} = 0.9\mu s$). In this case, breakdown did not occur until the Paschen limit near 10 mtorr. If instead, the cavity voltage was modulated with a 1 to 5 ms ramp, the multipactor discharge had sufficient time to develop, and a multipactor-induced glow discharge could form below the Paschen limit pressure, as low as 0.4 mtorr. This later case of the 1-5 ms rf rise time is similar to the situation on C-Mod, where the rf is increased with a 5 ms time constant. This experiment further suggests the multipactor-induced glow discharge is responsible for the inability to restart the C-Mod rf systems at elevated neutral pressure with a time constant of 5 ms.

The third CMX experiment investigated the situation of a gradual pressure rise with rf operating above the multipactor susceptible voltage. Breakdown did not occur before the Paschen limit in this unmagnetized case. This result is also seen and discussed by Höhn [5]. The results of these CMX experiments are summarized in Tab. 6.1.

Material	f (MHz)	d (cm)	Voltage rise time	**Multipactor observed?**	Glow discharge pressure (mtorr)
Cu [O] & SS	60-90	3	Slow step	**Yes**	0.4-0.8
Cu [O]	50	1	Slow step	**No**	10-14
Ti [O]	60-90	3	Slow step	**Yes**	0.4-0.8
Ti GDC	60-90	3	Slow step	**No**†	10-14
TiN	60-90	3	Slow step	**Yes**	0.4-0.8
50 μm Cu	60-90	3	Slow step	**No**‡	10-14
Cu [O]	70-90	3	Q/ω	**No**	10-14
Cu [O]	80	3	1-5 ms	**Yes**	0.4-0.8

† Multipactor quickly returns with oxidation

‡ In-situ GDC required

Table 6.1: Summary of CMX results supporting C-Mod multipactor experiments. The 50 μm sandblasted copper surface [50 μm Cu] was most successful in preventing multipactor for a range of frequencies. A "slow step" rise time refers to slow (of order seconds), stepwise voltage rise, while Q/ω rise time refers to the intrinsic rise time of the cavity for a given Q and ω, giving an approximate rise time of 1 μs.

6.5 Discussion of Alcator C-Mod and CMX Results

The C-Mod multipactor experiment results show the multipactor is less reactive to the rf circuit in the presence of magnetic field. It is suspected that the multipactor is likely happening in the vacuum coaxial regions shown in Fig. 6-6. Each antenna also has vacuum stripline sections, but these sections have E$\perp$B magnetic insulation. If the multipactor discharge is occurring in the aforementioned coaxial region, the multipactor would be constrained to a much impact smaller surface area in the coaxial region, impacting both inner and outer electrodes, and likely resulting in a smaller, less reactive, multipactor current. It is possible that the presence of the magnetic field could enable multipactor to occur with minimal reflected power, but with enough electron current to induce a glow discharge. The onset of this glow discharge in a magnetic field could occur at voltages higher than expected in the unmagnetized case because of the magnetically-confined multipactor current.

Yet, in order to explain the initial trip of the rf shown in Fig. 6-4, the standing wave pattern must be known at all transmission line locations and times. Questions remain as to the exact voltages in the multipactor susceptible locations as well as the exact role of the magnetic field on the multipactor-induced glow discharge. These questions will be left to be answered in future multipactor experiments on Alcator C-Mod and CMX.

6.6 Surface Roughening Solution to Alcator C-Mod Neutral Pressure Limits

6.6.1 50 μm sandblast copper surface treatment

In order to prevent operational neutral pressure limits on the Alcator C-Mod ICRF systems, multipactor discharge must be eliminated. Currently, the most feasible solution seems to be implementing electrodes with secondary electron emission coefficients below unity for all impact energies. Initial tests indicate the best candidate is the 50 μm sandblast surface treatment, which would initially be implemented on the inner and outer conductors of the vacuum coaxial feedthroughs. Because O/O trajectories (see Sec. 4.3.2) of high impact energy are prevented in the presence of the toroidal magnetic field, it may only be necessary to apply this treatment to the inner conductor. It is also thought that this surface roughening would be even more effective in preventing multipactor on Alcator C-Mod because of the presence of the toroidal magnetic field and the corresponding Larmor motion of the emitted electron.

As mentioned in Sec. 6.4, sandblasting copper electrodes with 50 μm aluminum oxide bead successfully eliminated multipactor on CMX in the parallel plate geometry at frequencies of 50 to 90 MHz and a gap spacing of 3 cm. Specifically, the sandblast material used is S.S. White Airbrasive Powder, Accubrade©-50, Blend #3. Two 10 cm diameter, 0.635 cm thick copper plates, as used in the CMX parallel plate configuration, were sandblasted on all facing surface area using a 0.635 cm nozzle for applying the surface treatment. There are several advantages to this surface treatment, including good conductivity and vacuum compatibility. Because rf transmission lines are typically made of copper, this surface treatment can be applied to the currently used electrodes, and can be cleaned and handled no differently than other vacuum prepared electrodes. This treatment can presumably be implemented on any surface, including the inside surface of outer coaxial electrodes or center conductors.

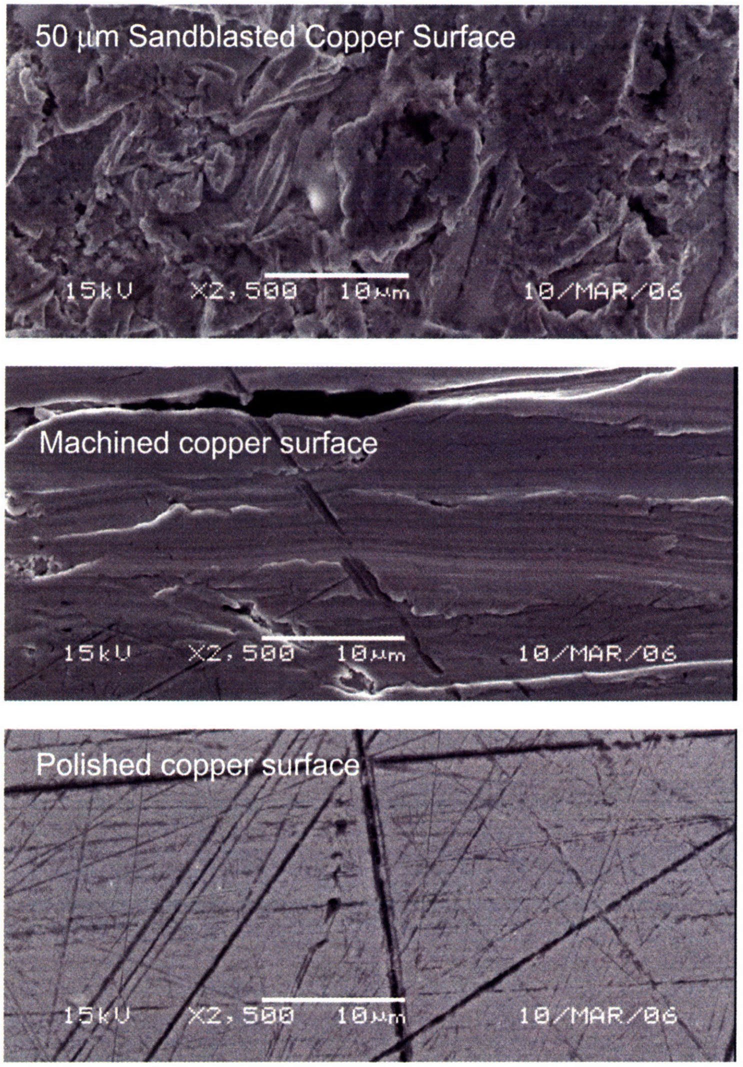

Figure 6-10: JEOL 5910 scanning electron microscope images of polished, machined, and sandblasted copper surfaces at 2500X.

Sandblasting the copper surface causes a much darker surface than the machined case due to the large degree of surface roughening, as seen in Fig. 6-12. Fig. 6-10 depicts JEOL 5910 scanning electron microscope images taken at 2500X magnification for the 50 μm sandblasted, machined, and polished surfaces. As seen in the figure, the sandblasting process drastically increases the surface roughness, yet creates a more

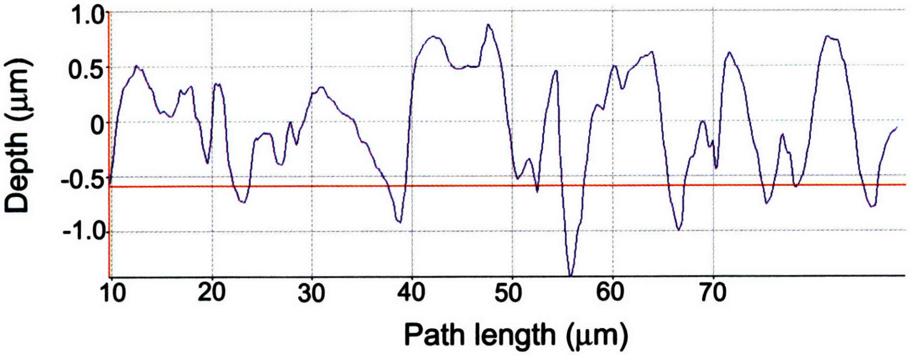

Figure 6-11: Cross-sectional view of the 50 μm sandblasted copper surface.

uniform surface with less enhanced field emission sites than the machined copper case [63]. Using the Alicona MeX 4.2 imaging software, a cross section profile of the surface is determined and shown in Fig. 6-11 [81]. This analysis determines that the sandblasting process creates peaks that are spaced several μm apart with the peak heights of order 1 μm. From these SEM images, there is no indication that the aluminum oxide grit material remains embedded in the copper surface after cleaning.

6.6.2 High voltage experiments of the sandblasted surface

Ideally, rf surfaces are prepared as smooth as possible to reduce field emission and high voltage arcing inside transmission lines [63, 67, 68]. Any anti-multipactor surface treatment applied to the high voltage transmission line systems on Alcator C-Mod must still allow high voltage handling and prevent vacuum breakdown at fields as high as 20 kV/cm. In order to determine if the sandblasted surface would satisfy this high voltage requirement, a DC high voltage test was performed on copper half spheres with different surface treatments. Pairs of polished, machined, and 50 μm sandblasted half spheres were placed 0.889 mm apart and tested for breakdown in air at high voltages of order 1 kV. Fig. 6-12 depicts the half spheres with surface treatments tested in the high voltage experiment. Table 6.6.2 gives the breakdown voltage determined from the high voltage experiment for each surface treatment.

As shown, the polished copper surface did not arc until an electric field of 51.7 kV/cm. As compared to the ideal case of the polished surface, a voltage handling

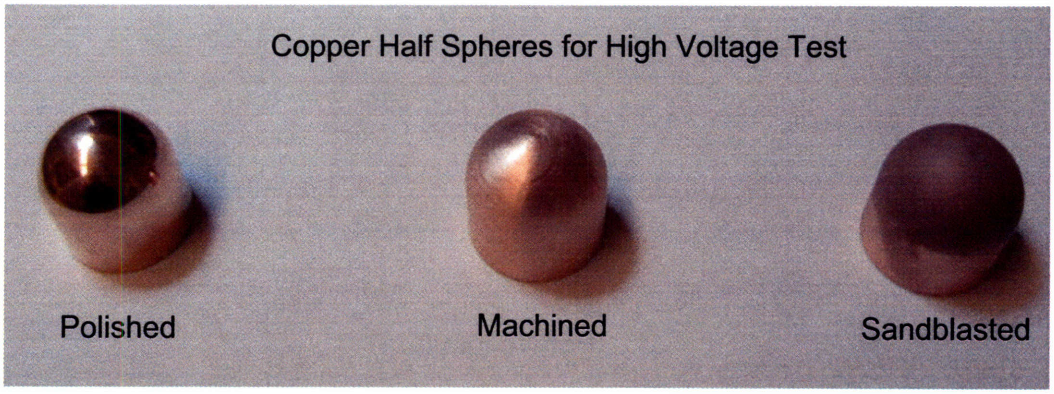

Figure 6-12: Copper half spheres with polished, machined, and sandblasted surface treatments for DC high voltage testing.

	Polished Cu	Machined Cu	Sandblasted Cu
Breakdown Voltage (kV)	4.6	4.3	4.4
Electric field (kV/cm)	51.7	48.4	49.5

Table 6.2: DC breakdown conditions for different surface preparations.

degradation of 6.4% and 4.3% was seen for the machined and sandblasted surface respectively. Interestingly, the sandblasted surface has better high voltage handling than the machined surface, most likely because the sandblasting process eliminates large field emitters which are present in the machined surface. In practice, the Alcator C-Mod transmission line electrodes are not polished surfaces but more similar to the machined surface. These high voltage results indicate that the sandblasted surface should cause no degradation of the high voltage handling on the Alcator C-Mod rf systems.

6.6.3 In-situ preparation of sandblasted surface in vacuum

One of the negative aspects of surface roughening as a anti-multipactor treatment is the enhanced gas entrainment due to the larger electrode surface area. Surface gases and impurities must all be removed to achieve the desired lowering effect on the secondary electron coefficient. Preliminary multipactor experiments were performed on the sandblasted electrodes in CMX after a short period of time in vacuum, with no baking, and no glow discharge cleaning. Upon initially applying rf voltage to the sandblasted electrodes, multipactor was detected due to the presence of surface gases on the electrodes. In order for this surface treatment to effectively lower δ for multipactor prevention, the adsorbed surface gases must be removed by glow discharge, baking, or long outgassing times.

The most effective process to remove these unwanted gases on CMX was to bake the vacuum chamber to 100°C, while allowing the initial multipactor to transition to a glow discharge near 1 mtorr. After only a few minutes of sustaining the glow discharge, and returning to low pressure ($<10^{-6}$ torr), multipactor could not be detected at any of the tested frequencies. While no direct measurement was made, the multipactor-induced glow discharge likely removes the surface gases by ion and electron impact. Keeping the chamber at high temperature prevents condensation and gas recycling from the walls, pumping the unwanted gases out of the vacuum system. This same in-situ treatment is necessary for successful implementation of this anti-multipactor surface as a solution to the Alcator C-Mod neutral pressure limit.

Chapter 7

Conclusions and Future Work

The work for this thesis provides new and improved data for multipactor discharges in both coaxial and parallel plate geometries. This investigation contributes to the current understanding of these discharges by providing the first experimentally-determined, electron distribution functions for coaxial and parallel plate geometries at a range of VHF frequencies. Because multipactor discharges can significantly limit or even damage rf systems, such as those on fusion experiments, understanding these discharges is critical to rf operation. The contribution of this work to a fast-growing and large body of multipactor studies will allow researchers to better design rf systems, operate them over a wider neutral pressure range, and possibly lead to the development of new multipactor technologies using the distribution function information of this work.

7.1 Contributions of CMX

The Coaxial Multipactor Experiment, described in Chap. 3, is the first experiment designed to specifically investigate the energy distribution functions of coaxial multipactor discharges. Because of the close similarities of the CMX coaxial configuration and the Alcator C-Mod rf systems, this work led to the discovery of multipactor discharge within the C-Mod rf systems. In addition, multipactor-induced glow discharge was determined to be the physical explanation behind the observed neutral pressure limit on the C-Mod antennas. Furthermore, CMX extends the study of parallel plate multipactor, agreeing very well with the only other experimental energy distribution study of Höhn, and further expanding the data to a wider range of frequencies and electrode materials. Because of CMX's versatile role as a multipactor testbed, various electrode materials are able to be easily tested in the parallel plate geometry, and as a result, a new, very promising, anti-multipactor surface treatment was discovered.

7.1.1 CMX as a multipactor testbed

CMX has the ability to create and investigate multipactor discharges in coaxial and parallel plate geometries for electrode spacings up to 10 cm and frequencies from 30 to 300 MHz with up to 1 kW of rf power. CMX features a full diagnostic set of directional coupler measurements for proper rf characterization, and CMX measures the multipactor current as a function of bias voltage with retarding potential analyzers. The energy distribution functions are determined from the I-V characteristic measured by the RPA. Using this new and unique facility, multipactor experiments can easily be carried out to investigate many different aspects of the multipactor discharge and the interaction with various electrode materials.

Specifically, this work investigated coaxial multipactor discharges in a 50 Ω line with a 10 cm outer conductor, at frequencies between 55 and 150 MHz. Multipactor discharges were measured for cleaned copper electrodes as well as the same electrodes with surface oxides and impurities, allowing determination of the effect of impurities on the coaxial discharge. In the parallel plate configuration, multipactor discharges were created and investigated for 1 to 3 cm electrode spacings and frequencies between 50 and 150 MHz. Copper, copper with Cu_2O, stainless steel, and titanium with Ti_2O_3 were used to create and measure parallel plate multipactor.

In both geometries, the multipactor discharge yielded maximum electron current densities of order 1 A/m^2, and this current was dependent on the electrode secondary emission coefficient. As shown for the various electrode materials in the parallel plate configuration, a higher secondary yield gave a higher multipactor current. In addition, the multipactor typically absorbed 10 to 15% of the rf power.

7.1.2 The coaxial multipactor energy distribution function

Coaxial multipactor energy distributions are measured for frequencies from 55 MHz to 150 MHz. In all cases, the distributions are comprised of two main populations: a high energy population consistently seen at 80% of the rf voltage, and a low energy population from 0 to 75 eV. The high energy population, which is responsible for sustaining the multipactor by secondary emission, moves with the rf voltage, but the energy always remains near 80% of the rf voltage. Using a Monte Carlo single particle simulation which moves electrons in the appropriate field and geometry, it is determined that the energy of this population is a result multipactor resonance conditions of the coaxial geometry and the $\frac{1}{r}$ electric field. In addition, both experimental and simulation energy distributions for the coaxial multipactor have a high energy tail which extends over 100 eV beyond the rf voltage. This tail is a result of electron angular momentum and electron trajectories which narrowly "miss" the inner conductor near the field reversal and then continue accelerating outward to the opposite side of the outer conductor. Outer conductor starting and impacting electrons (O/O), like that just mentioned, have sufficient energy to cause secondary emission, and the results suggest that a multipactor discharge could occur in the coaxial geometry on the outer conductor alone.

The low energy population of the energy distribution is a result of both space charge effects and secondary emission from the RPA entrance grid. The mutual repulsion of the phase focused electron sheet causes electrons to fall outside the resonant phase, and as a result, they are defocused and impact with low energy. This is determined using a simple correction applying a 20% phase spread due to a $2\text{x}10^{-8}$ C/m^2 current sheet. In addition to low energy electrons caused by space charge, primary electrons impacting the entrance grid can cause secondary emission which contributes to the low energy population in the overall distribution. Secondary emission from the bias grid has a negligible effect on the energy distribution.

Very good agreement was found between experiment and simulation results using a 20% phase spread, a 10 eV energy spread, and a entrance grid secondary emission correction to the simulation. Fig. 7-1 illustrates this agreement between the energy distributions of the simulation and experiment, reiterating these causes of the resulting distribution.

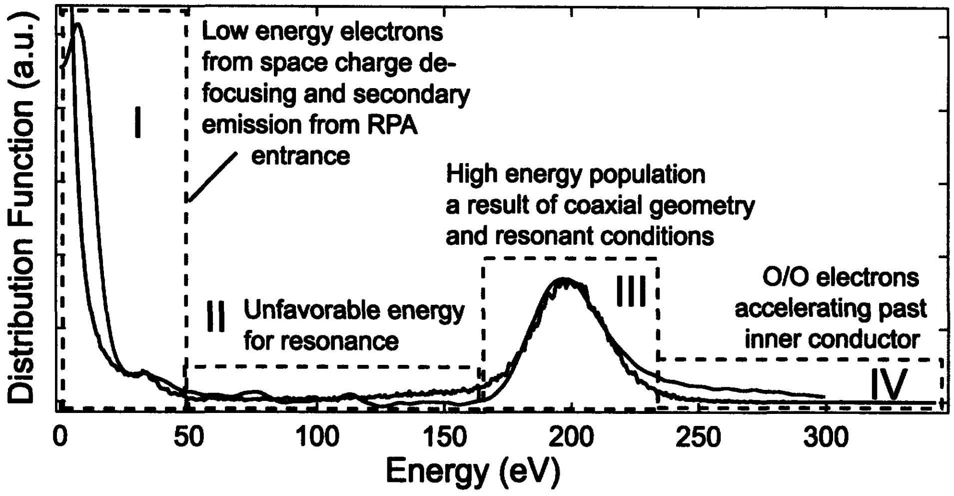

Figure 7-1: Coaxial multipactor energy distribution as described in Chap. 5

7.1.3 The parallel plate multipactor energy distribution function

Like coaxial multipactor distributions, the parallel plate multipactor energy distributions have low and high energy populations. The same arguments hold for the low energy population as the coaxial case, yet the high energy population in the parallel plate case is typically seen near 65-70% of the rf voltage. As in the coaxial case, the energy of this population is a result of the resonance conditions in the parallel plate geometry, but because of the differences in the rf electric field, the population energy relative to the rf voltage is less than the coaxial case. Good agreement was seen between simulation and experiment for the high energy populations of both CMX and those reported by Höhn [5].

7.1.4 Comparison between coaxial and parallel plate multipactor discharges

As illustrated in Chap. 5, for the same frequency, voltage, and electrode spacing, the coaxial multipactor has a higher energy distribution than the parallel plate case. As mentioned, the bulk of the multipactor-sustaining electrons are found at 80% and 70% of rf voltage for the coaxial and parallel plate geometries, respectively. The implication of this electron energy difference is that as the voltage is increased, the electrons in the coaxial region satisfy the multipactor conditions at a lower voltage than the parallel plate case, and the coaxial multipactor will occur first. This difference is also reflected in the susceptibility curves for copper electrodes in the two geometries. Many systems have both coaxial and stripline transmission lines of similar electrode spacing, and in this case, the coaxial region will preferentially support the multipactor discharge. This was seen experimentally on CMX, and this result will aid to determining the exact multipactor locations on rf systems.

7.1.5 CMX multipactor susceptibility

In both coaxial and parallel plate geometries, susceptibility curves giving the onset voltage with frequency and distance are shown in Chap. 3 and 5. Excellent agreement was seen between CMX results for coaxial electrodes with surface oxides and impurities and the experimental results of Woo [47]. In addition, this work provides the first experimentally-determined susceptibility data for clean copper coaxial electrodes, which have a onset voltage 50-100 volts higher than the case with oxides and impurities. CMX coaxial and parallel plate onset voltage data scale with $(f \cdot d)^2$, and data is fit to "rule of thumb" equations, given in Chap. 5. For similar electrode materials, the parallel plate multipactor is typically 10 volts higher than the coaxial case.

7.2 Multipactor within Alcator C-Mod ICRF systems

7.2.1 Multipactor-induced neutral pressure limits

At and above neutral pressures of 0.5 and 1 mtorr, rf operation of the respective Alcator C-Mod J and E ICRF systems is limited by antenna faulting and an inability to restart. These neutral pressures are below that expected for the initiation of a rf Paschen discharge, and the cause of this limit was previously unknown. Low power multipactor experiments, supported by results on CMX, show the formation of a multipactor-induced glow discharge at the same pressures of the observed limit. The C-Mod rf system has a 5 ms voltage ramp time, which allows sufficient time for the multipactor to develop and transition into a glow discharge. The glow discharge formation is accompanied by a very large jump in the reflected power, and no more power can be delivered to the rf antennas. It is currently believed that the discharge is occurring the coaxial vacuum feedthroughs of the transmission line systems, due to the system geometry and the CMX results favoring multipactor in coaxial geometries.

7.2.2 Solution to the observed neutral pressure limits

Using CMX's versatile nature, different surface treatments were investigated in order to find a solution to prevent multipactor and eliminate the observed neutral pressure limit on C-Mod. Due to the successful investigations of many others, it has been shown rough surfaces can eliminate multipactor by lowering the secondary coefficient below unity for the energies of interest. A new surface treatment of 50 μm aluminum oxide sandblast was implemented on copper electrodes. This surface dramatically increases the surface roughness as seen by SEM images, and the surface feature size is approximately 1 μm. After this surface was multipactor conditioned and glow discharge cleaned while baking the CMX vacuum chamber, multipactor could not be detected from 60 MHz to 90 MHz. Upon elimination of the multipactor discharge, the minimum pressure for glow discharge onset was raised from near 0.5 mtorr to over 10 mtorr. High voltage DC experiments show no significant high voltage degradation due to the sandblast-roughened surface. It is currently planned to implement this surface treatment on the J antenna vacuum transmission lines for higher neutral pressure operation.

7.3 Practical Engineering Considerations

From this investigation, there are several practical considerations which can benefit future engineers and scientists in the design and operation of rf systems. First, surface conditioning of rf vacuum components is very important when multipactor avoidance is crucial for rf operation. As shown, surface impurities lower the onset voltage for multipactor, can cause a local pressure rise, and possibly induce a glow discharge below the minimum pressure for Paschen breakdown. By successfully conditioning electrodes, the secondary electron coefficient can be lowered to that of the pure metal, which may be sufficient to eliminate multipactor in some cases. Yet, for most rf electrode materials, multipactor can still occur on the clean surface if the resonant conditions are satisfied. In this case, anti-multipactor treatments must be applied to all multipactor susceptible electrodes. While the multipactor may form first in the coaxial region, all possible multipactor sites must be eliminated. To eliminate multipactor in a coaxial geometry, results suggest that multipactor can be supported on the outer conductor alone; therefore, the anti-multipactor treatments must be applied to both inner and outer conductors. Also, due to the effect of impurities on the secondary emission coefficient, in-situ conditioning of surface roughening anti-multipactor treatments are necessary to prevent multipactor.

7.4 Directions for Future Work

Experimentally, there are many different aspects of multipactor discharges still necessary to investigate. Much of the future work may be possible with the sophisticated simulations available today, but as in this investigation, direct experimental investigation can bring new information to light. For example, the exact spatial distribution and time evolution of the multipactor has yet to be experimentally verified. Also, the exact role of the magnetic field in the coaxial geometry on the multipactor discharge, such as the situation on Alcator C-Mod, is still in question. This investigation could be possible using CMX and applying a magnetic field across the coaxial electrodes. In addition, there are countless unknown possibilities for new technologies which may arise in continuation of this work.

Specifically, there is further work necessary related to eliminating neutral pressure limits of fusion rf systems. As mentioned, it is currently planned to implement the 50 μm sandblast surface treatment to the copper electrodes in the vacuum transmission lines of Alcator C-Mod. Experimentally, successful implementation and in-situ surface preparation will be necessary, and questions still remain whether this treatment will allow higher neutral pressure operation. There is also a large theoretical need for the construction of a complete model of the Alcator C-Mod rf system, allowing determination of the standing wave pattern on all transmission lines for a variety of plasma conditions. This would provide the exact voltages in the multipactor-susceptible vacuum transmission lines, and therefore allow better determination of the areas which could support multipactor and the subsequent glow discharge.

In reference to the 50 μm sandblast surface treatment, a direct measurement of the secondary emission coefficient for a range of electron energies and surface conditions is still necessary. Also, future work will investigate different bead size sandblast treatments to determine the optimal surface roughening for preventing multipactor while retaining good high voltage handling. This future work will hopefully yield the optimal anti-multipactor surface treatment for rf systems to be applied to future devices such as ITER, future satellite payloads, or other rf systems of tomorrow.

Bibliography

[1] R. A. Kishek et al. Multipactor discharge on metals and dielectrics: Historical review and recent theories. *Phys. Plasmas*, 5(5):2120–2126, May 1998.

[2] J. M. Vaughan. Multipactor. *IEEE Trans. Electron Devices*, 35(7):1172–1180, July 1988.

[3] H. Bruining. *Physics and Applications of Secondary Electron Emission.* McGraw-Hill, NY, 1954.

[4] H. Seiler. Secondary electron emission in the scanning electron microscope. *J. Appl. Phys.*, 54(11):R1–R18, November 1983.

[5] F. Hohn et al. The transition of a multipactor to a low-pressure gas discharge. *Phys. Plasmas*, 4(4):940–944, April 1997.

[6] D. Woode and J. Petit. Investigations into multipactor breakdown in satellite microwave payloads. *ESA Journal*, 14:467–478, 1990.

[7] D. Woode and J. Petit. Design data for the control of multipactor discharge in spacecraft microwave and RF systems. *Microwave Journal*, 35(142):142–155, January 1992.

[8] P. F. Clancy. Multipactor control in microwave space systems. *Microwave Journal*, 21:77–83, March 1978.

[9] C. M. Lyneis, H. A. Schwettman, and J. P. Turneaure. Elimination of electron multipacting in superconducting structures for electron accelerators. *App. Phys. Let.*, 31(8):541–543, October 1977.

[10] R. Ballantini et al. Multipacting in 1400 MHz Beta=0.5 cavities for proton acceleration. In *10th Workshop on RF Superconductivity*, Tsukuba City, Japan, 2001.

[11] A. Kaye et al. Radio-frequency heating system. *Fusion Tech.*, 11(1):203–233, January 1987.

[12] ITER Physics Expert Group on Energetic Particles et al. Plasma auxiliary heating and current drive. *Nuc. Fusion*, 39(12):2495–2539, December 1999.

[13] S. J. Wukitch et al. Investigation of performance limiting phenomena in a variable phase ICRF antenna in Alctor C-Mod. *Plasma Phys. Control. Fusion*, 46(9):1479–1491, September 2004.

[14] T. P. Graves et al. Effect of multipactor discharge on alcator c-mod ion cyclotron range of frequency heating. *J. Vac. Sci. Tech. A*, 24(3):512–516, 2006.

[15] James Dillon Cobine. *Gaseous Conductors.* Dover Publications, Inc., New York, 1958.

[16] V. Baglin et al. The Secondary Electron Yield of Technical Materials and its Variation with Surface Treatments. In *7th European Particle Accelerator Conference*, Vienna, Austria, 2000.

[17] Spilios Riyopoulos. Multipactor with electric field retarding secondary emission. *Phys. Plasmas*, 5(1):305–311, January 1998.

[18] A. R. Nyaiesh et al. Properties of thin antimultipactor TiN and Cr_2O_3 coatings for klystron windows. *J. Vac. Sci. Tech.*, 4(5):2356–2363, September 1986.

[19] D. Wolk et al. Surface Treatment and Coating for the Reduction of Multipactor and Passive Intermodulation (PIM) Effects in RF Components. In *4th International Workshop in Multipactor, Corona and Passive Intermodulation in Space RF Hardware*, number AO-4025 ITT ESA, Noordwijk, The Netherlands, 2003.

[20] C. Gutton. *Compt. Rend.*, 186(303), 1928.

[21] P. T. Farnsworth. Television by electron image scanning. *J. Franklin Inst.*, 218:411–444, 1934.

[22] P. T. Farnsworth. Multipactor phase control. Technical Report 2071517, United States Patent Office, 1938.

[23] P. T. Farnsworth. Multipactor oscillator and amplifier. Technical Report 2091439, United States Patent Office, 1937.

[24] P. T. Farnsworth. Multipactor. Technical Report 2135615, United States Patent Office, 1938.

[25] P. T. Farnsworth. Multipactor oscillator. Technical Report 2137528, United States Patent Office, 1938.

[26] E. W. B. Gill and A. von Engel. Starting potentials of high-frequency gas discharges at low pressure. *Proc. R. Soc. London, Ser. A*, 192(1048):446–463, May 1949.

[27] A. J. Hatch and H. B. Williams. The secondary electron resonance mechanism of low-pressure high-frequency gas breakdown. *J. Appl. Phys.*, 25(4):417, April 1954.

[28] A. J. Hatch and H. B. Williams. Multipacting modes of high-frequency gaseous breakdown. *Phys. Rev.*, 112(3):681, November 1958.

[29] T. P. Graves et al. The Coaxial Multipactor Experiment (CMX): A facility for investigating multipactor discharges. *Rev. Sci. Inst.*, 77(1):014701–014704, January 2006.

[30] Jin Au Kong. *Electromagnetic Wave Theory.* EMW Publishing, Cambridge, MA, 2000.

[31] Theodore Moreno. *Microwave Transmission Design Data.* Dover Publications Inc., New York, 1948.

[32] J. R. Meagher and H. J. Markley. Practical analysis of ultra high frequency. RCA Service Company, Inc, Camden, New Jersey, 1943.

[33] Chuck Hutchinson, editor. *The ARRL Handbook for Radio Amateurs.* The American Radio Relay League, Inc, Newington, CT, 2001.

[34] S. J. Wukitch. Personal communication. 2005.

[35] D. R. Lide. *Handbook of Chemistry and Physics, 72nd ed.* CRC Press, 1991.

[36] D. J. Gibbons. Secondary electron emission. In A. H. Beck, editor, *Handbook of Vacuum Physics*, volume 2. Pergamon Press, 1966.

[37] I. Bojko, N. Hilleret, and C. Scheuerlein. Influence of air exposures and thermal treatments on the secondary electron yield of copper. *J. Vac. Sci. Tech. A*, 18(3):972–979, May 2000.

[38] N. Hilleret, C. Scheuerlein, and M. Taborelli. The secondary-electron yield of air-exposed metal surfaces. *Appl. Phys. A*, 76(7):1085–1091, May 2003.

[39] M. S. Chung and T. E. Everhart. Simple calculation of energy distribution of low-energy secondary electrons emitted from metals under electron bombardment. *J. Appl. Phys.*, 45(2):707–709, February 1974.

[40] K. Kanaya and H. Kawakatsu. Secondary electron emission due to primary and backscattered electrons. *J. Phys. D*, 5(9):1727–1742, September 1972.

[41] D. Ruzic et al. Secondary electron yields of carbon-coated and polished stainless steel. *J. Vac. Sci. Tech.*, 20(4):1313–1316, April 1982.

[42] R. E. Kirby and F. K. King. Secondary electron emission yields from PEP-II accelerator materials. *Nucl. Instrum. Meth. A*, 469(1):1–12, August 2001.

[43] S. I. Castañeda et al. Effects of air exposure on ion beam assisted TiN:O coatings to prevent multipactor. *J. Vac. Sci. Tech. A*, 21(6):2007–2012, November 2003.

[44] K. G. McKay. Total Secondary Electron Emission from Thin Films of Sodium on Tungsten. *Phys. Rev.*, 61(11-12):708–713, June 1942.

[45] G. Stupakov and M. Pivi. Suppression of the effective secondary yield for a grooved metal surface. Technical Report LCC-0145, SLAC-TN-04-045, 2004.

[46] J. R. M. Vaughan. A new formula for secondary emission yield. *IEEE Trans. Elec. Dev.*, 36(9):1963–1967, September 1989.

[47] R. Woo. Final Report on RF Voltage Breakdown in Coaxial Transmission Lines. Technical Report 32-1500, NASA-JPL, 1970.

[48] E. Somersalo, P. Yla-Oijala, and D. Proch. Analysis of multipacting in coaxial lines. In *Proceedings of the 1995 Particle Accelerator Conference*, volume 3, Dallas, TX, May 1995.

[49] R. A. Kishek and Y. Y. Lau. Interaction of multipactor discharge and rf circuit. *Phys. Rev. Let.*, 75(6):1218–1221, August 1995.

[50] R. A. Kishek, Y. Y. Lau, and D. Chernin. Steady state multipactor and dependence on material properties. *Phys. Plasmas*, 4(3):863–872, March 1997.

[51] Spilios Riyopoulos. Multipactor saturation due to space-charge-induced debunching. *Phys. Plasmas*, 4(5):1448, May 1997.

[52] P. Ylä-Oijala. Suppressing electron multipacting in coaxial lines by dc voltage. TESLA 97-21, November 1997.

[53] Daniel Boussard. RF Hardware Status. In *5th LEP Performance Workshop*, Chamonix, January 1995. SL Division.

[54] R. Woo. Multipacting discharges between coaxial electrodes. *J. Appl. Phys.*, 39(3):1528–1533, February 1968.

[55] Computer Simulation Technology. `http://www.cst.de/Content/Products/MWS/Overview.aspx`, Wellesley Hills, MA.

[56] I. H. Hutchinson. *Principles of Plasma Diagnostics.* Cambridge University Press, Cambridge, UK, 2002.

[57] The Mathworks Inc. Curve fitting toolbox documentation. `http://www.mathworks.com/access/helpdesk/help/toolbox/curvefit/curvefit.shtml`.

[58] John F. O'Hanlon. *A User's Guide to Vacuum Technology.* John Wiley and Sons, 1980.

[59] Alfredo H-S. Ang and Wilson H. Tang. *Probability Concepts in Engineering Planning and Design.* John Wiley and Sons, 1975.

[60] Julius S. Bendat and Allan G. Piersol. *Random Data; Analysis and Measurement Procedures.* John Wiley and Sons, 1986.

[61] Y. Takase et al. Engineering Design and Analysis of the Alcator C-Mod Two-strap ICRF Antenna. In *14th Symp. on Fusion Engineering*, San Diego, CA, 1992. IEEE.

[62] J.-M. Noterdaeme and G. Van Oost. The interaction between waves in the ion cyclotron range of frequencies and the plasma boundary . *Plasma Physics and Controlled Fusion*, 35(11):1481–1511, November 1993.

[63] P. A. Chatterton. Vacuum breakdown. In J. Meek and J. Craggs, editors, *Electrical Breakdown of Gases.* John Wiley and Sons, 1978.

[64] A. D. McDonald. *Microwave Breakdown of Gases.* John Wiley and Sons, New York, 1966.

[65] H. Wolff. Arcing in magnetic fusion devices. In *Atomic and Plasma-material Interaction Data for Fusion*, volume 1. International Atomic Energy Agency, Vienna, Austria, 1991.

[66] V. Bobkov et al. Influence of the plasma on ICRF antenna voltage limits. *J. Nuc. Mat.*, 313-316(15):956–961, March 2003.

[67] Jens Knobloch. *Advanced Thermometry Studies of Superconducting RF Cavities.* PhD dissertation, Cornell University, 1997.

[68] J. M. Lafferty. *Vacuum Arcs, Theory and Application.* John Wiley and Sons, Schenectady, New York, 1980.

[69] F. W. Baity et al. The ORNL/ASDEX Upgrade RF Breakdown Tester: Results and Plans. In *14th Topical Conf. on Radio Frequency Power In Plasmas*, volume 595, pages 510–513, Oxnard, CA, 2001. AIP.

[70] Sanborn C. Brown. *Basic Data of Plasma Physics, 1966.* The M.I.T. Press, Cambridge, MA, 1967.

[71] T. Kihara. The mathematical theory of electrical discharges in gases. *Rev. Mod. Phys.*, 24(1):45, January 1952.

[72] V. A. Lisovsky and V. D. Yegorenkov. Low-pressure gas breakdown in combined fields. *J. Phys. D: Appl. Phys.*, 27(11):2340–2348, November 1994.

[73] S. Riyopoulos. Collisional multipactor inside ambient gas. *Phys. Plasmas*, 11(5):2036–2045, May 2004.

[74] R. Udiljak et al. Improved model for multipactor in low pressure gas. *Phys. Plasmas*, 11(11):5022–5031, November 2004.

[75] Richard Udiljak. *Multipactor in a Low Pressure Gas.* PhD thesis, Chalmers Institute of Technology, 2004.

[76] A. Kaye et al. Present and future JET ICRF antennae. *Fusion Eng. Design*, 24(1):1–21, February 1997.

[77] F. W. Baity et al. Antenna loading impedance changes during arcs and ELMs on DIII-D. In *12th Topical Conf. on Radio Frequency Power in Plasmas*, volume 403, pages 405–408, Savannah, Ga, 1997. AIP.

[78] R. I. Pinsker. Development of impedance matching technologies for ICRF antenna arrays. *Plasma Phys. Control. Fusion*, 40(8A):A215–A229, 1998.

[79] B. LaBombard et al. Cross-field plasma transport and main-chamber recycling in diverted plasmas on Alcator C-Mod. *Nuc. Fusion*, 40(12):2041–2060, 2000.

[80] T. Fujii and S. Moriyama. High-Voltage Test of Feedthroughs for a High-Power ICRF Antenna. In *IEEE Trans. Plasma Sci.*, volume 29, pages 318–325, April 2001.

[81] MeX 4.2. Alicona Imaging GmbH. `http://www.alicona.com`, A-8074 Grambach, Austria.